

# **Self-Interference Cancellation for Full-Duplex Underwater Acoustic Systems**

**Lu Shen**

Doctor of Philosophy

University of York  
Electronic Engineering

December 2020



## Abstract

This work develops and investigates self-interference (SI) cancellation (SIC) techniques for full-duplex (FD) underwater acoustic (UWA) systems. To enable the FD operation in UWA systems, a high level of SIC is required. The main approach used in this work is the digital cancellation based on adaptive filtering. A general structure of the digital canceller is proposed which addresses key factors affecting the SIC performance, including the power amplifier and pre-amplifier nonlinearities, up- and down-sampling effects. With the proposed structure, the SI can be effectively cancelled in time-invariant channels by classical recursive least-square (RLS) adaptive filters, e.g., the sliding-window RLS (SRLS), but the SIC performance degrades in time-varying channels. A new SRLS adaptive filter based on parabolic interpolation of the channel time variations is proposed, which improves the SIC performance at the expense of the high complexity. To reduce the complexity, while providing the high SIC, a new family of interpolating adaptive filters which combine the SRLS adaptive algorithm with Legendre polynomials (SRLS-L) is proposed. A sparse adaptive filter is further proposed to exploit the sparsity in the expansion coefficients of the Legendre polynomials. For interpolating adaptive filtering algorithms, the mean squared error is unsuitable for measuring the SIC performance due to the overfitting. Therefore, a new evaluation metric, SIC factor, is proposed. The SIC performance of the proposed adaptive filters is investigated and compared with that of the classical SRLS algorithm by simulation, water tank and lake experiments. Results indicate that the proposed adaptive filters significantly improve the SIC performance in time-varying scenarios, especially with high-order sparse SRLS-L adaptive filter. Furthermore, SIC schemes with multiple antennas are investigated to explore the possibility of achieving extra amount of SIC in acoustic domain and cancelling the fast-varying surface reflections by adaptive beamforming.



# Table of contents

|   |           |
|---|-----------|
| <b>Abstract</b>   | <b>2</b>  |
| <b>List of tables</b>                                   | <b>9</b>  |
| <b>List of figures</b>                                  | <b>11</b> |
| <b>Acknowledgements</b>                                 | <b>18</b> |
| <b>Declaration</b>                                      | <b>20</b> |
| <b>1 Introduction</b>                                   | <b>23</b> |
| 1.1 Overview . . . . .                                  | 23        |
| 1.2 Review on existing SIC techniques . . . . .         | 25        |
| 1.2.1 Passive SI suppression . . . . .                  | 26        |
| 1.2.2 Analogue cancellation . . . . .                   | 29        |
| 1.2.3 Digital cancellation . . . . .                    | 31        |
| 1.3 State of the art in FD UWA systems . . . . .        | 36        |
| 1.4 SI channel characterization and modelling . . . . . | 36        |
| 1.4.1 Characterization of the SI channel . . . . .      | 37        |
| 1.4.2 Underwater acoustic simulators . . . . .          | 39        |
| 1.5 Water tank and field experiments . . . . .          | 43        |
| 1.6 Contributions . . . . .                             | 46        |
| 1.7 Thesis structure . . . . .                          | 48        |

|          |  |           |
|----------|--|-----------|
| <b>2</b> | <b>General Structure of the Digital Self-Interference Canceller</b>            | <b>51</b> |
| 2.1      | Digital SIC structure addressing the PA nonlinearity . . . . .                 | 52        |
| 2.1.1    | Digital SI canceller with two cancellation modes . . . . .                     | 52        |
| 2.1.2    | Digital SIC performance under two cancellation modes . . . . .                 | 55        |
| 2.2      | Extended structure of the digital SI canceller . . . . .                       | 61        |
| 2.2.1    | Sampling instant of the passband to baseband conversion . . . . .              | 61        |
| 2.2.2    | Multi-branch combining scheme . . . . .  | 62        |
| 2.2.3    | Evaluation of the extended digital SI canceller . . . . .                      | 64        |
| 2.3      | Adaptive equalization of the nonlinearity in the hydrophone pre-amplifier .    | 68        |
| 2.3.1    | Adaptive nonlinear equalization . . . . .                                      | 68        |
| 2.3.2    | The cost functions . . . . .   | 70        |
| 2.3.3    | Evaluation of the adaptive nonlinear equalizer . . . . .                       | 74        |
| 2.4      | Conclusions . . . . .  | 81        |
| <b>3</b> | <b>Time-Varying Self-Interference Channel Estimation</b>                       | <b>83</b> |
| 3.1      | Introduction . . . . .   | 84        |
| 3.2      | Evaluation of SIC performance . . . . .  | 84        |
| 3.2.1    | MSE and MSD performance . . . . .  | 85        |
| 3.2.2    | SIC Factor . . . . .   | 87        |
| 3.3      | Proposed SRLS-P adaptive filter . . . . .                                      | 90        |
| 3.3.1    | Classical ERLS and SRLS adaptive filters . . . . .                             | 91        |
| 3.3.2    | Delayed ERLS and SRLS adaptive filters . . . . .                               | 91        |
| 3.3.3    | SRLS-P adaptive filter . . . . .   | 92        |
| 3.4      | Baseband simulation results . . . . .  | 96        |
| 3.4.1    | MSD performance of RLS algorithms with a delay . . . . .                       | 97        |
| 3.4.2    | MSE, MSD and SIC performance of SRLS, SRLSd and SRLS-P<br>algorithms . . . . . | 100       |
| 3.4.3    | MSD, SIC and BER performance of SRLSd and SRLS-P algorithms                    | 102       |
| 3.5      | Passband simulation results . . . . .  | 104       |
| 3.6      | Experimental results . . . . .   | 105       |

---

|          |  |            |
|----------|--|------------|
| 3.7      | Conclusions . . . . .  | 110        |
| <b>4</b> | <b>Basis Expansion Model Adaptive Filtering for Self-Interference Cancellation</b> | <b>111</b> |
| 4.1      | Introduction . . . . .   | 112        |
| 4.2      | Proposed SRLS-L adaptive filter . . . . .  | 113        |
| 4.2.1    | Signal model . . . . .   | 113        |
| 4.2.2    | SRLS-L algorithm . . . . .   | 114        |
| 4.2.3    | Complexity of the SRLS-L adaptive filter . . . . .                                 | 117        |
| 4.3      | Homotopy SRLS-L-DCD adaptive filter . . . . .                                      | 121        |
| 4.4      | Numerical results . . . . .  | 124        |
| 4.4.1    | Simulation scenario . . . . .  | 124        |
| 4.4.2    | MSD performance . . . . .  | 127        |
| 4.4.3    | Complexity comparison . . . . .  | 131        |
| 4.5      | Experimental results in lake experiments . . . . .                                 | 133        |
| 4.5.1    | Experimental setup and transmitted signals . . . . .                               | 133        |
| 4.5.2    | Experimental vs simulation results . . . . .                                       | 134        |
| 4.5.3    | Experiments with different carrier frequencies and bandwidths . . . . .            | 135        |
| 4.6      | Conclusions . . . . .  | 137        |
| <b>5</b> | <b>Self-Interference Cancellation with Multiple Transducers</b>                    | <b>139</b> |
| 5.1      | Acoustic-domain SIC with two projectors . . . . .                                  | 139        |
| 5.1.1    | FD system structure with two projectors . . . . .                                  | 140        |
| 5.1.2    | Acoustic SIC scheme . . . . .  | 141        |
| 5.1.3    | Simulation results . . . . .   | 143        |
| 5.2      | Digital SIC with two hydrophones . . . . .   | 147        |
| 5.2.1    | Two-stage SIC scheme . . . . .   | 148        |
| 5.2.2    | Simulation results . . . . .   | 150        |
| 5.2.3    | Experimental results . . . . .   | 153        |
| 5.3      | Conclusions and discussion . . . . .   | 159        |

|          |   |            |
|----------|---|------------|
| <b>6</b> | <b>Conclusions and Further Work</b>   | <b>161</b> |
| 6.1      | Conclusions . . . . .   | 161        |
| 6.2      | Further work . . . . .  | 164        |
|          | <b>Acronyms</b>   | <b>167</b> |
|          | <b>References</b>   | <b>169</b> |
|          | <b>Appendix A Lake surfaces during the experiments</b>                              | <b>179</b> |
|          | <b>Appendix B Derivation of the channel estimate obtained by the SRLS algorithm</b> | <b>181</b> |
|          | <b>Appendix C Complexity analysis of the LBF estimator</b>                          | <b>183</b> |
|          | <b>Appendix D Complexity analysis of the HSRLS-L-DCD algorithm</b>                  | <b>185</b> |

# List of tables

|      |   |     |
|------|---|-----|
| 4.1  | SRLS-L algorithm . . . . .  | 116 |
| 4.2  | Leading DCD algorithm . . . . .   | 121 |
| 4.3  | $H\ell_1$ -DCD algorithm . . . . .  | 123 |
| 4.4  | Leading $\ell_1$ -DCD algorithm . . . . .   | 124 |
| 4.5  | Optimal $M$ for the adaptive filters . . . . .  | 128 |
| 4.6  | Parameters used for the HSRLS-L-DCD algorithm . . . . .   | 130 |
| 4.7  | Parameters used for the adaptive filters with DCD iterations, $H = 1$ and<br>$M_b = 24$ . . . . .                               | 130 |
| 4.8  | Overall complexity of the adaptive filters per sample . . . . .   | 132 |
| 4.9  | SICF (in dB) in the lake experiment and in simulation (Sim), $f_c = 32\text{kHz}$ ,<br>$f_d = 1\text{kHz}$ ; $L = 80$ . . . . . | 134 |
| 4.10 | SICF in the lake experiment, $f_c = 12\text{kHz}$ , $f_d = 1\text{kHz}$ and $L = 100$ . . . . .                                 | 135 |
| 4.11 | SIC factor (in dB) in the lake experiment, $f_c = 80\text{kHz}$ . . . . .   | 136 |
| 5.1  | The modified RLS algorithm for acoustic SIC . . . . .   | 143 |
| 5.2  | The modified ERLS algorithm for the beamformer . . . . .  | 149 |
| 5.3  | List of equipment used in the experiments . . . . .   | 153 |



# List of figures

|     |  |    |
|-----|--|----|
| 1.1 | Illustration of a full-duplex underwater acoustic system. Both transceivers simultaneously transmit and receive acoustic signals in the same frequency bandwidth. A receiver receives both the far-end transmitted signal and a strong self-interference signal from the near-end transmitter. . . . .   | 24 |
| 1.2 | Shared-antenna transceiver structure (Adapted from [20]) . . . . .   | 26 |
| 1.3 | Antenna configurations (Adapted from [52]) . . . . .   | 27 |
| 1.4 | FD UWA communication modem configurations (Adapted from [53]). . . . .   | 28 |
| 1.5 | The structure of the FD UWA communication modem (Adapted from [54]).   | 28 |
| 1.6 | Block diagram of FD system with active balun cancellation circuit (Adapted from [56]), where $g_i$ and $g_q$ represents the gain of the in-phase and quadrature components, respectively. RSSI is the residual signal level at the analogue canceller output, the algorithm updates $g_i$ and $g_q$ iteratively to minimize the energy of the residual signal. . . . . | 30 |
| 1.7 | Block diagram of FD system with two-stage iterative digital cancellation (Adapted from [42]). The near-end and far-end transmitted data are denoted as $a_n$ and $b_n$ , respectively. $x_{PA}(t)$ is the PA output, $z(t)$ is the received signal, and $\hat{y}_n(k)$ is the estimate of the far-end transmitted signal. . . . .                                      | 33 |

|      |   |    |
|------|---|----|
| 1.8  | An SI channel estimate from the lake experiment. The maximum depth of the lake is about 8 m. The projector and hydrophone are placed at 3 m and 4 m depth, respectively. The distance between them is around 1.3 m. The direct path is the one associated with the highest amplitude. Apart from the direct path, there are a few relatively stable reflections from the structure used to fix the transducer and hydrophone. The first surface reflection is obtained at the 16th tap. . . . . | 38 |
| 1.9  | Block diagram of the waymark model (Adapted from [68]). The index for waymarks is denoted by $m$ , the index for the passband signal samples and the taps of the channel impulse response are denoted by $n$ and $i$ , respectively.  | 40 |
| 1.10 | Zoom F4 multi-track recorder. . . . .   | 44 |
| 1.11 | Class AB and Class D amplifiers and an attenuator. . . . .  | 45 |
| 1.12 | Indoor water tank. The water tank is filled with 120 litre of water. The water tank experiments are not set up as a scaled version of the field experiment. It is used to obtain preliminary results of the cancellation scheme before the lake experiments. . . . .  | 45 |
| 2.1  | Block diagram of the FD UWA system. Two cancellation modes with different reference signals are considered. The recorders are synchronized to avoid having different sampling rates in the transmit and receive chains. . .   | 53 |
| 2.2  | Front-end processing. . . . .   | 53 |
| 2.3  | (a) Experimental setup of the FD UWA system. The plastic water tank is filled with 120 litre of water. (b) Placement of the projector and hydrophone underwater. (c) Vertical view of the tank. . . . .   | 56 |
| 2.4  | Impulse response estimate of the SI channel in the water tank experiment. The magnitude of the impulse response is shown in log scale due to its high dynamic range. . . . .  | 58 |
| 2.5  | Averaged NMSE performance of the NLMS and RLS-DCD algorithms. . .   | 59 |

|      |  |    |
|------|--|----|
| 2.6  | Averaged NMSE performance in the two cancellation modes. The original digital signal and ADC-converted PA output signal are used as the regressors in mode 1 and 2, respectively. . . . .  | 59 |
| 2.7  | Power spectra of the received signal before and after the digital cancellation.  | 60 |
| 2.8  | Estimates of the magnitude of the SI channel impulse response in the tank experiment. The channel estimates are obtained by the ERLS adaptive filter with the same desired signal and two time-shifted baseband PA outputs. . .  | 62 |
| 2.9  | NMSE performance of the digital canceller with different sampling delay in the water tank experiment. . . . .  | 63 |
| 2.10 | Block diagram of the extended structure of the digital SI canceller. The sample index with sampling rate $f_s$ , symbol rate $f_d$ and $2f_d$ are denoted by $n$ , $i$ and $j$ , respectively. . . . .   | 64 |
| 2.11 | Averaged NMSE performance in the tank experiment. Residual signals in the first and second branches refer to $e_1(i)$ and $e_2(i)$ in Fig. 2.10, respectively.   | 65 |
| 2.12 | Transducer configuration and the experimental site for the lake experiments.   | 66 |
| 2.13 | Averaged NMSE performance in the lake experiment. Residual signal in the first and second branches refer to $e_1(i)$ and $e_2(i)$ in Fig. 2.10, respectively. .  | 67 |
| 2.14 | Block diagram of the FD UWA system with nonlinear equalizer. . . . .   | 69 |
| 2.15 | Legendre polynomials. . . . .  | 70 |
| 2.16 | Rapp Model of the nonlinear amplitude response. . . . .  | 75 |
| 2.17 | SI channel impulse response in the cubic water tank. A long channel delay spread up to 150 ms can be observed. . . . .   | 76 |
| 2.18 | Comparison of the NMSE performance with the simulation data. The simulation data is generated by artificially introducing a nonlinearity to the hydrophone output signal recorded in the tank experiment. The NMSE curves are smoothed by a 200 ms rectangular window. . . . . | 77 |

|      |   |     |
|------|---|-----|
| 2.19 | Power spectra of the signals: (a) original hydrophone output; (b) hydrophone output with the artificial nonlinear distortion; (c) nonlinear equalizer output. Zoomed plots of the spectra in (a), (b), (c) are shown in (d), (e), (f), respectively. . . . .  | 78  |
| 2.20 | Experimental setup in a $3\text{ m} \times 2\text{ m} \times 2\text{ m}$ anechoic water tank. The projector and hydrophone are placed at 0.6 m depth. . . . .   | 79  |
| 2.21 | Comparison of the NMSE performance in the anechoic water tank. The NMSE curves are smoothed by a rectangular window of length 50 ms. . . .  | 80  |
| 2.22 | (a) PA output; (b) Original hydrophone output; (c) Signal equalized using HSR as the cost function; (d) Signal equalized using HSR with both constraints. Zoomed plots of the spectra in (a), (b), (c) and (d) are shown in (e), (f), (g) and (h), respectively. . . . .  | 81  |
| 3.1  | Adaptive filter with a delay. . . . .   | 85  |
| 3.2  | Block diagram of FD system with SIC; $r(i)$ is the baseband received SI, $s(i)$ is the regressor (baseband PA output), $f(i)$ is the artificially added far-end signal, $e(i)$ is the error signal at the adaptive filter output and $\varepsilon(i)$ is the residual signal that might be correlated with $f(i)$ ; $u(i)$ and $v(i)$ are the modified (uncorrelated) signal of interest and residual interference, respectively. | 88  |
| 3.3  | Time-varying channel and time windows of the SRLSd algorithm. . . . .   | 92  |
| 3.4  | Time-varying channel and time windows of the SRLS-P algorithm. . . . .  | 93  |
| 3.5  | A snapshot of the channel impulse response. . . . .   | 98  |
| 3.6  | MSD performance of the SRLS (Delay $T = 0$ ) and SRLSd algorithms. The optimal delay minimising the MSD is $T = M/2$ . . . . .  | 98  |
| 3.7  | MSD performance of the ERLS (Delay $T = 0$ ) and ERLSd algorithms. . . .  | 99  |
| 3.8  | MSD, MSE and SIC performance of the SRLS, SRLSd, and SRLS-P adaptive filters in slow and fast varying SI channels. . . . .  | 101 |
| 3.9  | BER, MSD and SIC performance for the SRLSd and SRLS-P adaptive filters in the fast varying SI channel. . . . .  | 103 |
| 3.10 | SIC performance of adaptive filters in the passband simulation. . . . .   | 105 |

|      |  |     |
|------|--|-----|
| 3.11 | The configuration of the lake experiments (Tx: projector; Rx: hydrophone).   | 106 |
| 3.12 | The experimental setup. The distances are shown in meters. . . . .   | 107 |
| 3.13 | SI channel estimate in the lake experiment. The channel delay spread is around 80 ms. It is observed that the first surface reflection (at the 16th tap) is fast-varying. The rest of the multipath components are the surface and the bottom reflections. . . . .   | 108 |
| 3.14 | SIC performance of adaptive filters in the lake experiment. The sliding window length $M$ is chosen to provide the best performance of each adaptive filter. . . . .   | 108 |
| 4.1  | Impulse response variation in the FD lake experiment. The lake surface is relatively calm during this experiment (see Fig. A.1 (b)). The lake depth is around 8 m. The distance between the transmitter (Tx) and receiver (Rx) is 7 cm. They are positioned at a depth of 4 m. It can be observed in the enlarged plot that the first few surface and bottom reflections are fast-varying. | 126 |
| 4.2  | Power delay profile (black curve) and cut-off frequency (red stem) of the multipath components in the FD lake experiment. The power of the multipaths are normalized with respect to the path with the maximum power. We plot the power delay profile and cut-off frequencies in the same figure to show the variance and speed of variation of the multipath components. . . .            | 126 |
| 4.3  | MSD performance of the adaptive algorithms against the polynomial order ( $P$ ) in the simulation generated based on the lake experiment. . . . .  | 128 |
| 4.4  | Estimates of expansion coefficients when using the HSRLS-L-DCD algorithm.  | 129 |
| 4.5  | Projector (Tx) and hydrophone (Rx) in the lake experiment. . . . .   | 133 |
| 5.1  | Block diagram of acoustic SIC for FD UWA system. Index $n$ is used for samples at the high sampling rate $f_s$ and index $i$ is used for samples at the lower sampling rate $f_d$ . The first projector is used for data transmission, and the second projector is used to emit a cancellation signal. . . . .   | 141 |
| 5.2  | Pulse shaping and carrier modulation. . . . .  | 141 |

|      |  |     |
|------|--|-----|
| 5.3  | Estimation of the secondary path $\mathbf{h}_2$ . . . . .  | 142 |
| 5.4  | Configuration of the simulation scenario (Tx1: primary projector; Tx2: secondary projector; Rx: hydrophone). . . . .   | 143 |
| 5.5  | Amplitude of the impulse response of the primary path ( $\mathbf{h}_1$ ). . . . .  | 144 |
| 5.6  | Amplitude of the impulse response of the secondary path ( $\mathbf{h}_2$ ). . . . .  | 145 |
| 5.7  | NMSE and SIC performance of the FD UWA system against the far-end SNR. The interference level increases with the far-end SNR. This explains the degradation in SIC and the increase in MSE at high far-end SNR. . . . .  | 146 |
| 5.8  | BER performance of the FD UWA system with different levels of far-end SNR.   | 147 |
| 5.9  | Block diagram of the two-stage SIC scheme; $s(i)$ is the PA output, $x_1(i)$ and $x_2(i)$ are the baseband received signals at the first and second hydrophones, respectively; $e_1(i)$ and $e_2(i)$ are the residual signals at the first and second hydrophones and $e_c(i)$ is the combined signal after adaptive beamforming. . . . .  | 148 |
| 5.10 | Power spectra of the signals at a single hydrophone in the static environment produced by the Waymark simulator. The power spectral densities are normalized with respect to the maximum of the power spectral density of the received signal. Received signal of the first branch refers to $x_1(i)$ in Fig. 5.9.   | 151 |
| 5.11 | Configuration of the simulation scenario with time-varying surface waves. . . . .  | 152 |
| 5.12 | Power spectra of signals in an environment with time-varying sea surface produced by the Waymark simulator. The power spectral densities are normalized with respect to the maximum of the power spectral density of the received signal. Received signal of the first branch and the combined residual signal after beamforming refer to $x_1(i)$ and $e_c(i)$ in Fig. 5.9, respectively. Residual signal of the first branch after DSIC refers to $e_1(i)$ . . . . . | 152 |
| 5.13 | Configuration of the water tank experiments. The plastic water tank is filled with 120 litre of water. . . . .   | 154 |

---

|      |  |     |
|------|--|-----|
| 5.14 | Power spectra of the signals in the water tank experiment. The power spectral densities are normalized with respect to the maximum of the power spectral density of the received signal on the first branch. Received signals of the first and second branches and combined residual signal after beamforming refer to $x_1(i)$ , $x_2(i)$ and $e_c(i)$ in Fig. 5.9, respectively. Residual signals of the first and second branches after DSIC refer to $e_1(i)$ and $e_2(i)$ , respectively. . . . . | 155 |
| 5.15 | Experimental site on the lake. . . . .   | 157 |
| 5.16 | Projector/hydrophones configuration for the lake experiment. . . . .   | 157 |
| 5.17 | Power spectra of signals in the lake experiment. The power spectral densities are normalized with respect to the maximum of the power spectral density of the received signal on the first branch. Received signals of the first and second branches and combined residual signal after beamforming refer to $x_1(i)$ , $x_2(i)$ and $e_c(i)$ in Fig. 5.9, respectively. Residual signals of the first and second branches after DSIC refer to $e_1(i)$ and $e_2(i)$ , respectively. . . . .           | 158 |
| A.1  | Lake surfaces at the Kelk Lake under different weather condition. . . . .  | 180 |



## **Acknowledgements**

I would like to express my deepest gratitude to my supervisor, Dr. Yuriy Zakharov, for his guidance, support and encouragement during my Ph.D study.

I would also like to thank my thesis advisor, Dr. David Halliday, for the valuable discussions and feedback on my work throughout the Ph.D. Thanks to my external examiner, Prof. Sergio M. Jesus, for the in-depth discussions during the viva and detailed feedback on my work.

Thanks to the colleagues at the Department of Electronic Engineering for creating a friendly and supportive environment. Thanks to the members of the Underwater Acoustics Research Group for the insightful advices and discussions at the seminars.

Thanks to Dr. Benjamin Henson for all the help and encouragement during my Ph.D study. Thanks to Dr. Nils Morozs and Prof. Paul Mitchell for their help in the field experiments.

I would like to express my sincere thanks to my family, without whom none of this work could have possibly happened.

Finally, I would like to thank the colleagues from the Newcastle University, Dr. Charalampos Tsimenidis, Jeff Neasham and Dr. Cornelius Healy for providing the experimental site and technical support during the experiments.



## Declaration

I declare that this thesis is a presentation of original work and I am the sole author. This work has not previously been presented for an award at this, or any other, University. All sources are acknowledged as References.

## Publications

### Publications directly associated with thesis work

- L. Shen, B. Henson, Y. Zakharov, and P. Mitchell, “Digital self-interference cancellation for full-duplex underwater acoustic systems,” *IEEE Transactions on Circuits and Systems II: Express Briefs*, vol. 67, no. 1, pp. 192–196, 2019
- L. Shen, B. Henson, Y. V. Zakharov, and P. Mitchell, “Two-stage self-interference cancellation in full-duplex underwater acoustic systems,” in *MTS/IEEE Oceans - Marseille*, 2019, pp. 1–6
- L. Shen, B. Henson, Y. Zakharov, and P. Mitchell, “Robust digital self-interference cancellation for full-duplex UWA systems: Lake experiments,” in *Underwater Acoustics Conference and Exhibition*, 2019, pp. 243–250
- L. Shen, B. Henson, Y. Zakharov, and P. D. Mitchell, “Adaptive nonlinear equalizer for full-duplex underwater acoustic systems,” *IEEE Access*, vol. 8, pp. 108 169 – 108 178, 2020

- L. Shen, Y. Zakharov, B. Henson, N. Morozs, and P. Mitchell, “Adaptive filtering for full-duplex UWA systems with time-varying self-interference channel,” *IEEE Access*, vol. 8, pp. 187 590–187 604, 2020
- L. Shen, Y. Zakharov, L. Shi, and B. Henson, “BEM adaptive filtering for SI cancellation in FD underwater acoustic systems,” *submitted to Signal Processing*, Under review
- Y. Wang, Y. Li, L. Shen, and Y. Zakharov, “Acoustic-domain self-interference cancellation for full-duplex underwater acoustic communication systems,” in *IEEE Asia-Pacific Signal and Information Processing Association Annual Summit and Conference*, 2019, pp. 1112–1116

#### **Other publications**

- Y. Zakharov, Y. Fei, P. Mitchell, N. Morozs, B. Henson, L. Shen, and T. Tozer, “Low-complexity UAC modem and data packet structure,” in *IEEE Underwater Communications and Networking Conference*, 2018, pp. 1–5
- Y. Zakharov, B. Henson, R. Diamant, Y. Fei, P. D. Mitchell, N. Morozs, L. Shen, and T. C. Tozer, “Data packet structure and modem design for dynamic underwater acoustic channels,” *IEEE Journal of Oceanic Engineering*, vol. 44, no. 4, pp. 837–849, 2019
- N. Morozs, W. Gorma, B. T. Henson, L. Shen, P. D. Mitchell, and Y. Zakharov, “Channel modeling for underwater acoustic network simulation,” *IEEE Access*, 2020

Lu Shen

December 2020

# Chapter 1

## Introduction

### 1.1 Overview

Underwater communication has attracted significant interest due to its wide applications in marine and oceanographic research, environmental monitoring, offshore exploration and other commercial applications [11–16]. Acoustic waves are the best candidate for long-range underwater communications since the electromagnetic waves suffer from the severe attenuation and limited transmission range [11]. Although acoustic waves can achieve a transmission range of hundreds or even thousands of miles, the attenuation of the acoustic waves is severe at high frequencies, which makes the available bandwidth for underwater acoustic (UWA) communication extremely limited [17–19]. Thus, any technologies that promise an increase in spectral efficiency should be considered.

In most communication scenarios, the transceiver works in half-duplex mode, which means the transceiver transmits and receives either at different time or over different frequencies. A long-held assumption in wireless communication has been that a transceiver cannot simultaneously transmit and receive on the same frequency band due to the severe self-interference (SI) from the near-end transmitter [20–23]. Recent advances in full-duplex (FD) radio systems demonstrate that it is practical to achieve FD communications with the innovative SI cancellation (SIC) techniques [23–28]. If FD operation is applicable in UWA systems, the capacity of the acoustic links would be significantly increased. From the network

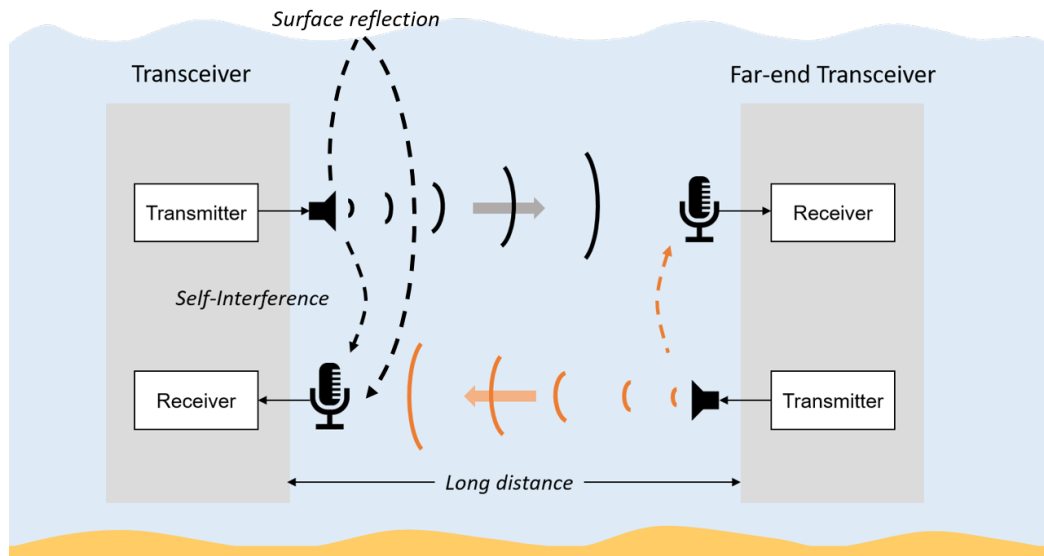


Fig. 1.1 Illustration of a full-duplex underwater acoustic system. Both transceivers simultaneously transmit and receive acoustic signals in the same frequency bandwidth. A receiver receives both the far-end transmitted signal and a strong self-interference signal from the near-end transmitter.

layer point of view, FD combined with network multiple access control protocols would increase the practical data throughput [20, 29, 30]. The application of FD operation can also be found in sonar systems [31]. Most of active sonars use pulse waveforms instead of continuous waveforms to avoid the strong SI (transmission leakage) from the transmitter. If it is possible to achieve FD operation, the system performance will be extremely improved [32].

Despite all the aforementioned benefits of FD communication, it is not seen to be widely used due to the challenge of cancelling the strong SI caused by the near-end transmitted signal (as shown in Fig. 1.1). In some scenarios, the SI can be more than 100 dB higher than the receiver's noise level [21, 23]. If the SI is not completely cancelled, the residual SI will reduce the signal to noise ratio (SNR) of the far-end desired signal thus degrading the system throughput. In terrestrial radio communications, a combination of analogue and digital cancellation schemes is normally used [21, 26, 33–41]. A certain amount of SI is cancelled in analogue domain before digital cancellation to avoid the saturation in analogue-to-digital converter (ADC) [42, 21, 36, 38, 43–45]. Apart from the limitation of the ADC, the hardware impairments in the transmit and receive chains such as the nonlinear distortions introduced by

the power amplifier (PA) [33], the carrier frequency offset [46] and the in-phase/quadrature (I/Q) imbalance [47] need to be addressed to ensure high level of SIC.

For UWA systems, in general significantly lower frequencies are used than that in terrestrial radio communications. In such systems, ADCs up to 24 bits and higher can be used, which would allow a digital cancellation up to 100 dB feasible. The front-end processing of the receiver can be done in the digital domain, thus avoiding hardware impairments such as the carrier frequency offset and I/Q imbalance [48]. Hydrophones with a long cable are normally equipped with an integrated pre-amplifier to avoid the SNR loss. Pre-amplifiers have an almost linear response within a voltage limit. Beyond the limit, they become non-linear and saturate [49]. Apart from the pre-amplifier, the transducer itself is a nonlinear device, it remains linear only for small amplitudes. For FD UWA systems, the near-end propagation channel and the nonlinear response of the equipments, including the PA in the transmit chain [34], hydrophone pre-amplifier and transducers [50], should be accurately estimated when performing digital cancellation. Another limiting factor is the fast channel variation of the SI channel. Existing digital cancellation algorithms are not capable of providing the required level of SIC in fast time-varying channels. Therefore, advanced digital cancellation algorithms should be developed for FD UWA systems, which can deal with all the aforementioned signal distortions.

The aim of this work is to develop novel digital cancellation techniques to achieve a high level of SIC in FD UWA systems. The acoustic-domain SIC technique will also be explored to reduce the SI level before digital cancellation.

## 1.2 Review on existing SIC techniques

In this section, we review main existing SIC techniques used in the state of the art designs and discuss their advantages and limitations.

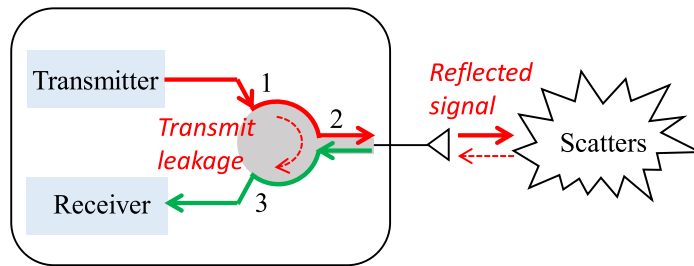


Fig. 1.2 Shared-antenna transceiver structure (Adapted from [20])

### 1.2.1 Passive SI suppression

Passive SI suppression techniques are used before analogue and digital cancellation to provide a degree of physical isolation between the transmitter and receiver. Depending on antenna structures of the transceiver, different SIC techniques are used.

With the shared-antenna transceiver structure, a circulator is normally used to provide isolation between the transmitter and receiver [21, 38]. The circulator is a passive non-reciprocal three-port device, which connects the antenna to the transceiver. As shown in Figure 1.2, the antenna is connected to port 2, the transmitted signal is fed through port 1 and routed to port 2 for transmission. The received signal from the antenna is passed from port 2 to port 3 and then fed to the receiver circuit. The circulator cannot completely isolate port 1 and port 3, there will be some transmit leakage and the near-end reflected signal received at port 3 inevitably. Observed from the experimental results in [21, 38], up to 20 dB reduction of the SI signal is achieved.

With the separate-antenna transceiver structure, multiple (more than two) antennas can be used for transmitting and receiving signals. Different kinds of passive SI suppression techniques can be used.

Antenna separation is considered as the simplest passive SI suppression technique. By separating the transmit and receive antennas for a fixed distance, the SI signal will be attenuated due to the path loss [26, 51]. The larger distance between the transmit and receive antennas, the more attenuation the SI signal experiences. The antenna separation approach is adopted in [26], where one antenna is used for transmission and the other one is used for

reception. A separation distance of 20 cm and 40 cm are considered, which are reasonable for mobile devices like a tablet or laptop. The measurement results [26] indicate that for a signal with the carrier frequency 2.4 GHz and 625 kHz bandwidth, 39 dB and 45 dB suppression of the SI is achieved for a distance of 20 cm and 40 cm, respectively.

Apart from the antenna separation, for a device with limited space, different physical placements and orientations of the transmit and receive antennas also have an influence on the SI reduction performance. In [52], the SI attenuation is measured for three different antenna configurations as shown in Fig. 1.3. Both the transmit and receive antenna are omnidirectional. The best SI reduction performance is achieved with configuration (b), which has the maximum horizontal distance between two antennas. In [53], the effect of the acoustic-shell coupling on the formation of the SI signal is investigated. The considered modem structure is shown in Fig. 1.4. It is found that the sound pressure level at the center location is significantly higher than that at locations shifted from the center. Therefore, the SI level can be reduced by adjusting the position of the receiving end.

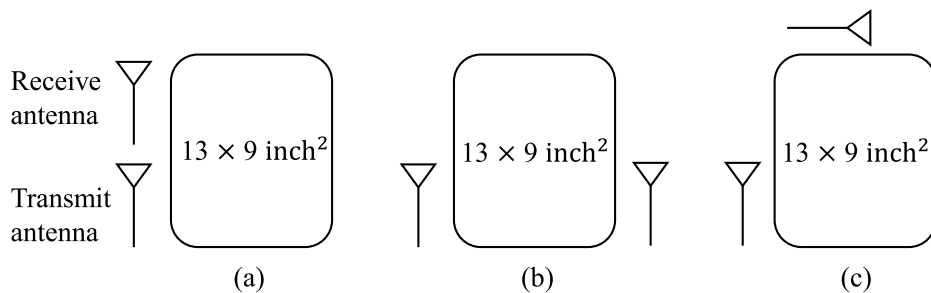


Fig. 1.3 Antenna configurations (Adapted from [52])

In [54], an acoustic baffle is inserted between the projector and hydrophone to suppress the SI signal. The projector and hydrophone are vertically spaced and further separated by a rod. The use of the acoustic baffle reduces the received SI power in the direction of the hydrophone position.

The use of nulling transmit antenna is suggested in [25], such as the printed annular slot antenna [55]. The nulling transmit antenna forms an omnidirectional radiation pattern except for one particular direction. The nulling direction can be controlled to match the position of

Different receiving locations

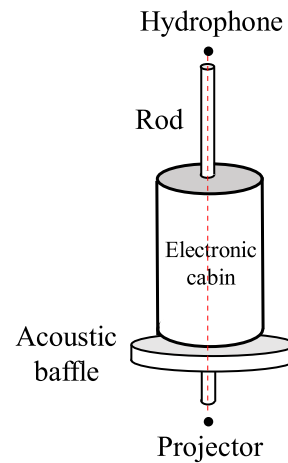
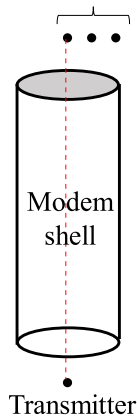


Fig. 1.4 FD UWA communication modem configurations (Adapted from [53]).

Fig. 1.5 The structure of the FD UWA communication modem (Adapted from [54]).

the receiver. The nulling antenna is expected to achieve about 25 to 30 dB cancellation. The major drawback of this design is that the nulling antenna will reduce the SNR at the far-end receiver in the nulling direction.

In [23], two transmit antennas and one receive antenna are used for antenna cancellation. By placing two transmit antennas at distance  $d$  and  $d + \lambda/2$ , respectively, two transmitted signals are added destructively and cancel one another at the receiver. The experimental result [23] indicates that a SI reduction of 33 dB is achieved when a radio signal is transmitted at 2.4 GHz carrier frequency with 5 MHz bandwidth. Apart from the fact that by using three antennas the overall size of FD transceiver is increased, there are two major limitations of this approach:

- Amplitude mismatch of the received signals from two transmit antennas. If there is 1 dB difference in the powers of two signals, the SI reduction is restricted to 20 dB.
- Not applicable for wideband signals. A fixed receive antenna position only corresponds to one particular frequency. If the receive antenna is placed with respect to the carrier frequency, there will be a receive antenna placement error for other frequencies.

To conclude, the design with circulator is simple and easy to produce, but there is no passive component of the same functionality which can be used in FD UWA systems. The use of nulling antenna achieves SI reduction at the expense of a reduction in the far-end SNR

in the nulling direction. The antenna cancellation scheme which reduces the SI signal by destructively adding the two transmitted signals is less applicable in FD UWA systems due to the use of wideband acoustic signals. The SI can be reduced by adjusting the position of the receiving end as suggested in [53].

### 1.2.2 Analogue cancellation

The general principle of analogue cancellation is to generate a cancellation signal which mimics the inverse of the actual received SI signal. Ideally, by combining the cancellation signal and the received signal, the SI will be cancelled completely. In this subsection, a range of analogue cancellation techniques are reviewed and their merit and limitation are discussed.

The Quellan noise canceller (QHx220) is used for analogue SIC in many designs [23, 25, 56]. The analogue canceller adjusts the amplitude and phase of the transmitted signal to match that of the SI signal in the received signal. The amplitude and phase of the transmitted signal is changed by adjusting gains of the in-phase and quadrature components. For a radio signal of 2.4 GHz carrier frequency and 5 MHz bandwidth, 20 dB of analogue cancellation is achieved [23]. However, the cancellation performance of the analogue canceller is limited for wideband signals. Apart from the bandwidth limitation, another drawback of this design is that the parameters of the analogue canceller require manual tuning. It is desired to have an adaptive algorithm which automatically tunes the parameters of the canceller according to the dynamic environment.

In [56], balun cancellation is proposed. The key idea of the balun cancellation is that we can use a balun to obtain the inverse of the transmitted signal and then use the inverted signal for SIC. Unlike the phase-offset based method used in [23], the balun cancellation is applicable for wideband signals as well. The inverted signal is delayed and attenuated to match the SI channel between the transmit antenna and the receive antenna. In this design, high-precision passive components are used to provide the delay and the attenuation of the cancellation circuit. Thus, this cancellation technique is called balun passive cancellation. The experimental results indicate that balun passive cancellation shows good cancellation performance for wideband signals [56].

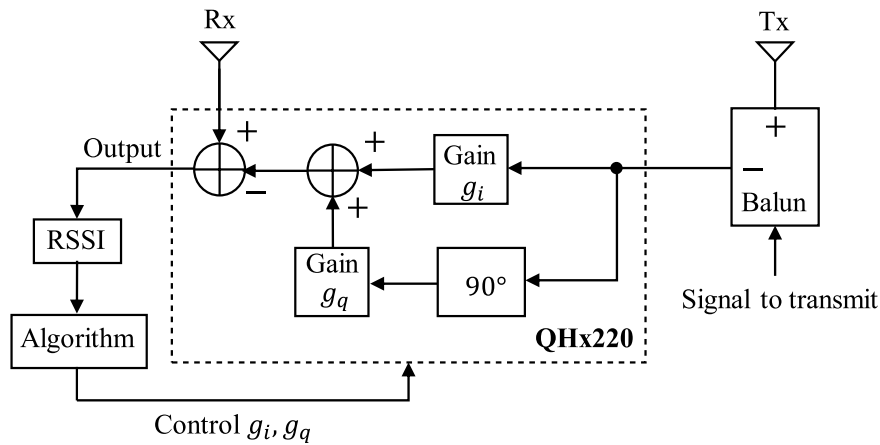


Fig. 1.6 Block diagram of FD system with active balun cancellation circuit (Adapted from [56]), where  $g_i$  and  $g_q$  represents the gain of the in-phase and quadrature components, respectively. RSSI is the residual signal level at the analogue canceller output, the algorithm updates  $g_i$  and  $g_q$  iteratively to minimize the energy of the residual signal.

An auto-tuning algorithm is proposed to achieve active balun cancellation [56]. As shown in Fig. 1.6, the Quellan analogue canceller combined with the auto-tuning algorithm is used to provide an approximation of the delay and attenuation. The auto-tuning algorithm is designed to minimize the residual SI by tuning the gains of the in-phase and quadrature signals. The main limitation here comes from the analogue canceller, which cannot work at high transmit power. If the transmit power is too high, nonlinearities will be introduced in the cancellation circuit, which will degrade the performance of both analogue and digital cancellation. To remove the limitation on transmit power and further improve the performance of active cancellation, it is suggested to use fine-grained programmable analogue attenuators and delay lines instead of the QHx220 analogue canceller [56].

In [21], an analogue cancellation circuit is designed to reconstruct the SI signal by a linear transversal filter. The PA output is used as the reference signal, which incorporates both the quantization errors and the linear/non-linear distortions introduced in the transmit chain. The cancellation circuit consists of a number of parallel fixed delay lines and each delay line is connected to a variable attenuator. The delay range of the delay lines is chosen to cover the actual delay spread of the SI channel. Once the delay range is chosen, the cancellation signal is generated by linearly combining outputs of the delay lines with different attenuations.

Each variable attenuator provides a certain amount of attenuation level. The attenuation of each delay line is tuned iteratively to minimize the residual SI energy. As indicated by the experimental results in [56], an analogue cancellation of 47 dB is achieved for a WiFi signal with 5 GHz carrier frequency and 80 MHz bandwidth.

For FD UWA systems, the high resolution ADC is unlikely to be saturated, but the hydrophone might be driven to have a nonlinear response when the received signal amplitude is too high. Analogue cancellation is considered to be useful to remove a certain amount of SI before signal reception at the hydrophone. However, it is not feasible to apply the aforementioned analogue cancellation techniques in FD UWA systems considering the large channel delay spread.

In [57], an auxiliary transmit chain is used for analogue cancellation in FD UWA systems. The aim of the analogue cancellation is to cancel the strong SI component from the direct path. The cancellation signal is generated by applying an attenuation to the delayed version of the transmitted signal in the digital domain, and then converted to an analogue signal. The cancellation performance depends on the accuracy of the estimated delay and attenuation applied to the transmitted signal. As indicated by the simulation results, up to 40 dB of analogue cancellation can be achieved. As the nonlinearity of the PA is not taken into account in this design, it is reasonable to believe that the analogue cancellation might degrade in practical scenarios.

Another approach to reduce the SI level before signal reception is the acoustic cancellation. The SI can be cancelled in the acoustic domain using a secondary projector which emits a cancellation signal [58].

### 1.2.3 Digital cancellation

Digital cancellation is normally operated after analogue cancellation to further reduce the residual SI power.

The simplest method for digital cancellation is to use a coherent detector [23]. The detector correlates the baseband transmitted signal with the digitalized baseband received signal. The peak of the correlation indicates the delay and attenuation of the SI signal, which

are then used to reconstruct the SI signal. In this design, a digital cancellation of 10 dB is achieved. This limited performance can be explained by two reasons. Firstly, the reference signal is not chosen properly. The actual transmitted signal is not the same as the clean digital signal. The hardware impairments introduced in the transmit chain are not taken into account. The second reason is that the SI signal received at the receiver contains multipath components, thus it cannot be perfectly reconstructed by using a single delay and attenuation.

The digital cancellation performance can be improved by reconstructing the SI signal based on the SI channel estimates. In [56], the SI channel is estimated in the frequency domain by the least square (LS) algorithm. The baseband transmitted signal is used as the reference signal. Then, the channel impulse response is computed by the inverse fast Fourier transform (IFFT) and is used for the reconstruction of the SI signal. The limitation of this design is that the channel should be re-estimated on a periodic basis depending on how fast the channel varies. Another limitation is that the SI channel is modelled as a linear system, thus the nonlinearity introduced in the transmission chain cannot be cancelled by the digital canceller. The experimental result in [23] with a 10 MHz WiFi signal show a digital cancellation of 30 dB.

In [21], the digital cancellation is operated in two steps to cancel both the linear and nonlinear components of the SI signal. For linear cancellation, the aim is to cancel the SI leakage from the direct path and the multipath due to the reflections. The SI channel is modelled as a linear noncausal system. Previous and future samples of the baseband transmitted signal are used to reconstruct the SI signal at the current sampling instant. This is achievable since the whole transmitted signal is known at the receiver. The channel impulse response is estimated by the LS method in the time domain. For nonlinear cancellation, the Taylor series expansion is used to model the nonlinearities. Only odd-order terms are considered in the nonlinear channel model. The digitalized baseband equivalent model is represented as:

$$y(n) = \sum_{\substack{p=1, \\ p \text{ odd}}}^P \mathbf{h}_p^T \mathbf{x}(n) |\mathbf{x}(n)|^{p-1}, \quad (1.1)$$



cancellation. In this case, the nonlinear distortion of the PA is incorporated in both the reference signal and the received signal thus the rest of the distortions can be modelled by a linear channel model. The digital cancellation is operated in two stages. In the first stage, the near-end SI channel is estimated by the LS method. The accuracy of this channel estimate depends on the receiver's noise level and the far-end signal power. A more accurate estimate can be achieved if the far-end signal is removed from the received signal. Therefore, the far-end transmitted symbols are decoded and re-modulated to provide an estimate of the far-end transmitted signal. In the second stage, the estimated far-end transmitted signal and the received signal are used to generate an estimate of the far-end channel. Then, the received far-end signal is reconstructed and subtracted from the received signal. After that, the near-end SI channel is estimated again. With such iterations, more accurate channel estimates can be obtained. As demonstrated by the simulation results, 46 dB of SIC is achieved after the first stage cancellation. After the second iteration, up to 70 dB cancellation is achieved. This approach outperforms the SI canceller in [21], which has also taken the nonlinear cancellation into account. The extra amount of cancellation achieved in this design can be attributed to the high-accuracy channel estimates obtained in the second iteration with the removal of the far-end signal, which significantly improves the estimation accuracy.

An adaptive non-linear digital SIC algorithm is proposed in [39]. The pure baseband transmitted signal is used as the reference signal, thus the channel model includes the transmit and receive chain together with the propagation channel. To deal with the nonlinearities introduced by the active components, the same nonlinear function is used as in (1.1). To iteratively estimate the channel coefficients, a least mean squared (LMS)-based algorithm with basis function orthogonalization is proposed. The orthogonalization is performed on the basis function vector to avoid the large eigenvalue spread of the correlation matrix due to the highly correlated basis functions [59]. To evaluate the performance of the nonlinear adaptive algorithm, a highly nonlinear low-cost PA is used in the transmit circuit. The experimental results in [39] indicate that 46 dB of digital cancellation is achieved.

It is known that the recursive least square (RLS) algorithm provides higher convergence speed to the steady-state level compared to the LMS algorithm [59]. In [60], a digital

canceller based on the RLS algorithm is proposed to estimate the nonlinear SI channel in FD UWA systems. The Hammerstein model is used to model the nonlinear response introduced by the PA. The time interval between the beginning of the near-end transmission and the arrival of the far-end signal is called the non-overlapping period. It is proposed to operate channel estimation during the non-overlapping period instead of using the whole transmission period to avoid the influence of the far-end signal on the estimation performance. In addition, sparse constraint is applied to the cost function to exploit the sparsity of the SI channel. As indicated by the simulation results, the detection performance is improved by operating the channel estimation during the non-overlapping period compared to utilizing the whole SI signal. The detection performance is further improved when sparse constraint is applied to the algorithm.

In [48], it is indicated that channel estimation performance of the maximum-likelihood (ML) estimator is better than that of the LS-based estimator in the presence of non-Gaussian noise due to the far-end signal. To improve the estimation performance, a noise-predictive ML algorithm (NPML) with sparse constraint is proposed to estimate the sparse SI channel. The channel estimate is initialized with the LS estimation, and then updated iteratively using a stochastic gradient descent based algorithm. As indicated by the experimental results in a swimming pool, the NPML algorithm with sparse constraint outperforms the LS-based estimator and the conventional NPML algorithm. The limitation of this design is that the nonlinear distortion introduced by the PA is not taken into account; secondly, it is uncertain how the proposed algorithm performs in practical scenarios with fast-varying SI channels.

For FD UWA systems, it is possible to achieve high level of SIC performance in digital domain. Existing digital SIC techniques are not capable of providing the required level of SIC, thus advanced digital SIC algorithms should be developed. The key factors that need to be considered when developing digital SIC schemes for UWA applications are the nonlinear distortions introduced by the equipment and the dynamic underwater environment. The sparsity of the UWA channel can also be exploited to improve the channel estimation performance.

### 1.3 State of the art in FD UWA systems

In this section, we present the state of the art designs and summarize existing SIC techniques applied in FD UWA systems.

The first full-duplex underwater acoustic modem is experimentally investigated in [54]. Orthogonal frequency-division multiplexing (OFDM) and spread-spectrum modulation techniques are used for the near-end and far-end data transmission, respectively. Sea experimental results show significant improvement in the system throughput. In this design, the near-end SI is suppressed by physical isolation between the transducer and hydrophone. As indicated in [53], the power of the near-end SI can be further reduced by adjusting the hydrophone position.

In [57], an analogue cancellation scheme is proposed to cancel the strong SI signal from the direct path in FD UWA systems. An RLS-based digital canceller is proposed in [60], which estimates the joint response of the PA nonlinearity and the propagation channel. The SI channel estimation is performed in the time interval before the far-end signal arrives. In [48], a noise-predictive ML algorithm with sparse constraint is proposed for the digital SIC. These SIC techniques are evaluated by simulation and experiments in water tanks. Their performance in practical scenarios has not been investigated.

Due to the dynamic underwater environment, the tracking ability of the cancellation algorithm is a key factor to achieve a high level of SIC. Known UWA channel estimators are not capable of providing such a high estimation accuracy in FD systems. In Section 4.1, we review a class of identification algorithms which can provide improved tracking performance when estimating SI channels.

### 1.4 SI channel characterization and modelling

In this section, we analyse key features of the SI channel in UWA systems and briefly describe techniques/simulators used for SI channel modelling.

### 1.4.1 Characterization of the SI channel

UWA channels are considered to be difficult for communications [61]. They are characterised by multipath propagation with long delay spreads due to multiple reflections from the sea surface and bottom, refraction and low speed of sound [61]. To understand the difficulties and limitations to be addressed in the SIC scheme for FD UWA systems, SI propagation channel should be accurately characterised.

In [62], measurements of the SI channel impulse response are presented based on sea experimental data. The experiments are carried out in August 2018 in the North Sea. The maximum depth of the experimental site is around 50 m. The hydrophone and the projector are vertically placed at 5 m and 15 m, respectively. Linear frequency modulated chirp signals are used as the transmitted signal. The SI channel is estimated by correlating the PA output with the bandpass filtered received signal. A key observation from [62] is the long reverberation of at least 200 ms of the SI channel. To cover the large delay spread, a long filter length is required for SI channel estimation, which would increase the complexity of the digital canceller. Thus, it is desirable to have a low-complexity design for digital SIC.

Another factor which must be taken into account when designing the SIC scheme is the fast channel variation speed due to the time-varying sea/lake surface. A three-dimensional SI channel impulse response obtained from a FD lake experiment is shown in Fig. 1.8 to provide some insights into the channel variation. The SI channel estimation is done in the baseband using an adaptive filter. The baseband sampling frequency is  $f_d = 1$  kHz, thus the adaptive filter taps are separated by a 1 ms interval. It is seen that the direct path and the reflections from the structure used to fix the equipments are strong and stable while other paths are fast-varying, especially for the first surface reflection at the 16th tap. Similar degree of variation also exhibits in other reflections from the surface and the bottom. It is found in [63] that the channel coherence time in dynamic oceans can be as short as 80 ms and it is highly variable in the experiments. Similar conclusions are drawn in the work [64], which studies statistical characteristics of the SI channel using lake experimental data. It is indicated in [64] that the first surface reflection is the dominant path among all the reflections,

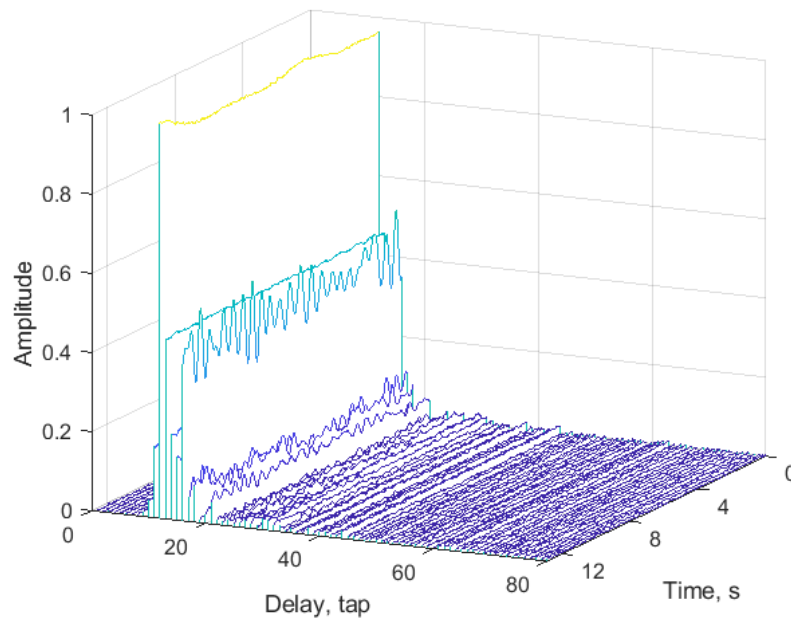


Fig. 1.8 An SI channel estimate from the lake experiment. The maximum depth of the lake is about 8 m. The projector and hydrophone are placed at 3 m and 4 m depth, respectively. The distance between them is around 1.3 m. The direct path is the one associated with the highest amplitude. Apart from the direct path, there are a few relatively stable reflections from the structure used to fix the transducer and hydrophone. The first surface reflection is obtained at the 16th tap.

the coherence time of which is around 70 ms in the lake experiments. This level of variation speed would raise a high requirement to the tracking ability of the digital canceller.

Apart from the moving sea surface, fast channel variation can also be introduced by the motion of the transmitter and/or receiver [61]. To achieve reliable communication, Doppler shifts must be taken into account in the communication system design. Various Doppler estimation methods have been proposed to compensate the multipath and Doppler effects in time-varying UWA channels [65–67].

In this thesis, we assume that the relative position of the transducer and hydrophone is fixed. Based on the studies conducted on SI channel characterization, it is reasonable to conclude that the two major factors to be taken into account in the digital SI canceller design is the long reverberation of the SI channel and the fast channel variations.

## 1.4.2 Underwater acoustic simulators

Sea experiments are expensive and difficult to conduct. Due to the dynamic underwater environment, it is hard to guarantee the same experiment conditions when comparing the performance of different communication systems [68]. Thus, it is desirable to have a simulator which provides a simulation of the UWA signal transmission that mimics a sea trial for analysing the system performance before conducting field experiments.

Modelling the acoustic wave propagation is difficult due to the large channel delay spread introduced by the multipath propagation and the severe Doppler distortion caused by the motion between the transmitter and the receiver. Apart from that, the specific propagation conditions of the particular sea area should also be taken into account. In this subsection, we review the commonly used UWA simulators and a specified-spectra based simulator which can be used to model time-varying channels in both terrestrial radio and UWA systems.

### The VirTEX simulator

A general approach for modelling the UWA signal transmission is to compute the channel impulse response for the source and receiver locations that correspond to every sampling instant of the signals. The VirTEX simulator [69] computes the ray information on a relatively sparse grid of points in range and depth. The range of the grid covers the trajectory of the receiver. For any receiver position, the ray information is obtained through interpolation. Assume there are two multipath arrivals, at each of them there are four surrounding grid points, then the interpolated point would comprise of eight multipath arrivals in total. The ray amplitudes of the interpolated point is computed using a combination of the weighted amplitudes of the four neighbouring grid points. The weights of the amplitudes from four grid points are computed based on the horizontal and vertical distance between the interpolated point and each grid point. The corresponding delay of each ray is adjusted by the travel time differences between the interpolated point and the grid point according to the local speed of sound, the geometric distance and incident angle from the interpolated point to the grid point.

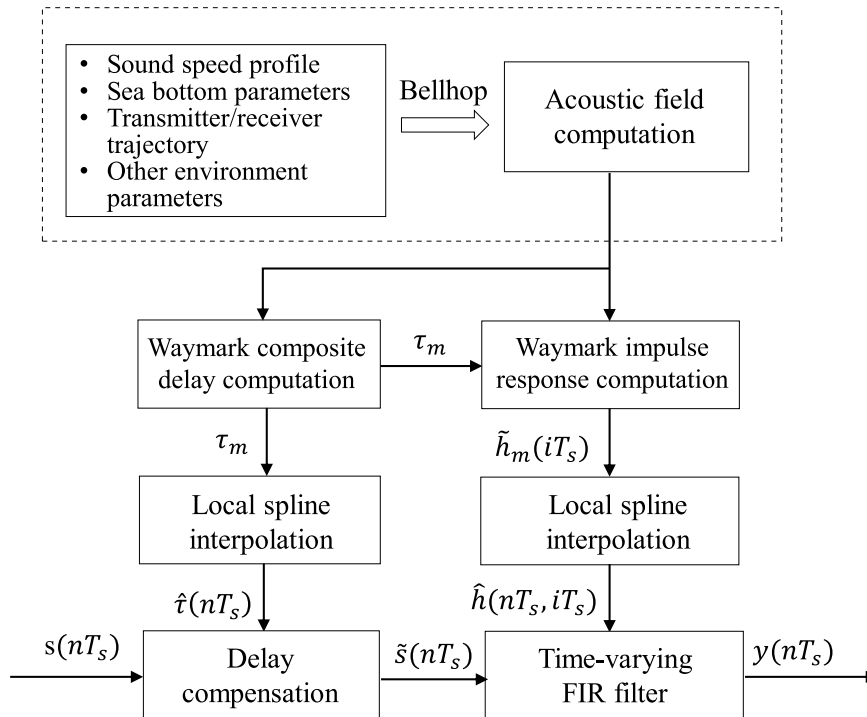


Fig. 1.9 Block diagram of the waymark model (Adapted from [68]). The index for waymarks is denoted by  $m$ , the index for the passband signal samples and the taps of the channel impulse response are denoted by  $n$  and  $i$ , respectively.

The limitation of the VirTEX model is that the interpolation is operated at the sampling frequency, thus the computational complexity is high.

### The Waymark simulator

The Waymark simulator and its extensions proposed in [68, 70, 71] are developed to simulate long signal transmission sessions and meanwhile reduce the computational complexity. A block diagram of the passband Waymark simulator proposed in [68] is given in Fig. 1.9. In the passband Waymark simulator, the trajectory of the receiver is sampled at a much lower rate than the sampling rate. The acoustic field at each waymark (trajectory-sampling) point is computed using the BELLHOP ray-tracing program [72]. Then, the channel frequency response can be computed over the frequency band of interest, which includes both the transmitted signal bandwidth and the maximum Doppler shift introduced by the motion between the transmitter and the receiver.

The channel variation is considered to be fairly slow between one signal sample to another, thus the waymark interval  $T_w$  can be set much longer than the signal sampling interval  $T_s$ . Then, the channel impulse responses between two waymark points are obtained by local-spline interpolation. Local-spline is chosen because it has less memory requirement. Particularly, local cubic B-spline is used as the basis function. For cubic B-spline interpolation, only four basis functions and the corresponding coefficients are required to reconstruct the channel impulse response at every sampling instant. Each coefficient can be found as a weighted combination of the previous, the current and the future waymark impulse responses. Therefore, at any sampling time instant, only six waymark impulse responses are required to reconstruct the channel impulse response.

Before we interpolate the channel impulse response between two waymark points, the time difference introduced by the change in the transmitter/receiver position should be taken into account. If the interpolation between two waymark points is operated directly without delay adjustment, significant errors will be introduced in the interpolation results (see an example in [68]). The delay is adjusted approximately by a delay shift  $\Delta\tau$  to align the two consecutive waymark impulse responses with respect to the maximum energy. Then, the waymark composite delay is updated by  $\tau_m = \tau_{m-1} + \Delta\tau$ .

After that, the delay-adjusted impulse response  $\tilde{h}_m(iT_s)$  is used for generating the interpolated channel impulse response  $\hat{h}(nT_s, iT_s)$ . The composite waymark delay at every sampling instant  $\hat{\tau}(nT_s)$  is also interpolated and applied to the transmitted signal to compensate for the delay introduced in the impulse response interpolation. Finally, the channel output  $y(nT_s)$  is obtained by convolving the interpolated channel impulse response  $\hat{h}(nT_s, iT_s)$  with the delay-adjusted transmitted signal  $\tilde{s}(nT_s)$ .

### **The baseband Waymark simulator**

The baseband Waymark simulator is proposed in [70] with the aim to further reduce the simulation time. Instead of generating the channel impulse responses at a high sampling rate  $f_s$  at the passband, the baseband equivalent channel impulse responses are generated at baseband with a lower sampling rate  $f_d$ . The transmitted signal is down-converted, low-pass

filtered and down-sampled to produce the baseband equivalent signal. Then, the channel output is computed in the same way as in the passband Waymark simulator but at a lower sampling frequency. Once the channel output has been obtained, the signal is up-sampled and up-converted back to the high sampling rate at the passband. When we convert the received signal back to the carrier frequency, a phase correction is applied to the output signal to compensate for the phase shift produced by the composite delay at the carrier frequency. Note that the baseband Waymark simulator recovers the time variation of the time-varying channel impulse response. It takes into account both the rescaling of the signal and the frequency dependency.

### **The Grid Waymark simulator**

The computational complexity of the baseband Waymark model [70] is significantly reduced by the baseband processing. The efficiency of the baseband Waymark model is mostly limited by the ray tracing program used for acoustic field computation.

To address this limitation, the grid baseband Waymark model is developed in [71]. Instead of computing the acoustic field at every waymark point, the acoustic field is pre-computed on a space grid which covers the whole receiver trajectory. The ray information of all the arrivals at every grid point is stored in the memory. During the simulation, the ray parameters at every waymark point are approximately interpolated by combining all the arrivals at four neighbouring grid points as in the VirTEX model.

### **Specified-spectra based simulator**

Unlike the aforementioned UWA simulators, the specified-spectra based simulator is not an acoustic simulator. It can be generally applied for simulating time-varying channels. Assume that the SI channel  $\mathbf{h}(i)$  consists of  $L$  multipath components. Every element  $[\mathbf{h}(i)]_\ell$  of  $\mathbf{h}(i)$  is a stationary random process with a power spectral density  $c_\ell G(f)$ , where  $G(f)$  is uniform within a frequency interval  $[-f_{\max}, f_{\max}]$ , and  $c_\ell$  is the variance of the  $\ell$ th channel tap. The parameter  $f_{\max}$  determines the maximum variation speed of the multipath components. The UWA channel normally has a decaying power delay profile due to the spreading and

absorption loss [61]. For instance, assuming the power delay profile  $c_\ell$  of the SI channel decays exponentially, it can be generated as:

$$c_\ell = e^{-\gamma\ell}, \quad \ell = 0, \dots, L - 1, \quad (1.2)$$

and  $\gamma$  is chosen to control the ratio between the variance of latest arrivals ( $\ell = L - 1$ ) and that of the first arrival ( $\ell = 0$ ). The random processes  $[\mathbf{h}(i)]_\ell$  are independent for different  $\ell$ , and they are generated using the fast Fourier Transform (FFT)-method [73].

In this thesis, the passband Waymark model is used for simulating the acoustic signal transmission underwater. This is due to the high accuracy required for the FD scenario. The up and down conversions in the baseband Waymark model and the interpolation of the field information in the Grid Waymark might introduce some approximation error into the signal generation. Since the computational time is not our main concern, it is better to use the passband version which ensures the high accuracy of the signal processing. The specified-spectra based simulator is used for modelling the time-varying scenarios instead of using UWA simulators. This is due to the fact that the application of the proposed algorithms is not limited in UWA systems, it could be applied in any time-varying communication systems. Besides, this approach guarantees that the true channel impulse response is available for comparison with its estimates, which would require extra processing with the passband Waymark simulator.

## 1.5 Water tank and field experiments

For FD systems, the experimental equipment has a strong impact on the SIC performance. To understand those effects, most of the cancellation schemes are evaluated by tank and lake experiments. This section introduces the equipment used in the indoor water tank and lake experiments and provides some interpretation of the experimental data.

The Zoom F4 multi-track recorder [74] shown in Fig. 1.10 has been used for both signal transmission and reception. It can transmit or record up to four channels simultaneously. The recorder contains high resolution 24-bit ADC and digital-to-analogue converter (DAC) which



Fig. 1.10 Zoom F4 multi-track recorder.

ensures low quantization noise. It supports a range of sampling frequencies up to 192 kHz. Each channel is equipped with a clip indicator and a level meter to monitor the input signal level. The timecode function of the recorder allows synchronization of two recorders, which is vital for digital cancellation when the input signals are sampled by two recorders. This function is used when the baseband transmitted data is used as the reference signal for digital cancellation.

Class A amplifier is considered as the best class of amplifier due to its excellent linearity. When Class A amplifier is not available, Class AB and Class D amplifiers are the alternative choices. In Fig. 1.11, we show the PAs and an attenuator used in the experiments. The PULSE PLA300 Class AB amplifier [75] contains two channels. Both channels are equipped with a clip indicator for signal level monitoring. The PA gain can be adjusted by the knob. The Behringer A800 Class D amplifier [76] has similar functionalities as that of the Class AB amplifier. The main difference is the level of nonlinearity introduced during the amplification, a relatively high level of nonlinear distortion can be observed in the signal spectrum when using the Class D amplifier. It is worth to point out that there is no noticeable difference in the digital cancellation performance with the proposed canceller structure when using the aforementioned amplifiers. The Behringer Ultra-DI DI100 direct injection box [77] is used



Fig. 1.11 Class AB and Class D amplifiers and an attenuator.



Fig. 1.12 Indoor water tank. The water tank is filled with 120 litre of water. The water tank experiments are not set up as a scaled version of the field experiment. It is used to obtain preliminary results of the cancellation scheme before the lake experiments.

as the attenuator. It could provide either 20 dB or 40 dB of attenuation of the input signal. The attenuator is used to ensure that the PA output signal is reduced to a level within the input voltage range of the recorder.

We use the Benthowave BII-7530 transducer [78] with 50 m cable for data transmission. Based on the calibration results obtained at Neptune Sonar [79], the usable frequency of the transducer is up to 100 kHz. Two Benthowave low noise broadband hydrophones (BII-7011 and BII-7032 [80]) are used at the early stage of the investigation. The Neptune D/140/H hydrophones with pre-amplifiers [81] are used in the field experiments. The pre-amplifier gain of each hydrophone is 20 dB. The usable frequency range is between 10 Hz to 200 kHz.

The indoor water tank used for conducting tank experiments is shown in Fig. 1.12. The volume of the water tank is  $380 \times 1190 \times 420 \text{ mm}^3$ . Indoor water tank experiments provide a relatively stable environment compared to that of the lake experiments. Without the fast channel variation introduced by the moving lake surface, the limitation of the cancellation performance either comes from the imperfections of the equipment or due to the long reverberation in the water tank. We have also conducted experiments in an anechoic water tank in Newcastle University. A major benefit of the anechoic water tank is that most of the reflections are absorbed by the anechoic material at the tank boundaries, which is useful for assessing the distortions introduced by the equipment.

## 1.6 Contributions

The original contributions of this work are summarized as follows:

### **General structure of the digital SI canceller**

To ensure high level of digital SIC, the nonlinear distortion introduced by the equipment in the transmit and receive chains and transducers need to be addressed. In this work, the general structure of the digital SI canceller is proposed. The proposed structure uses the PA output as the reference signal for digital cancellation to address the nonlinear distortion introduced by the PA. Furthermore, an adaptive nonlinear equalization technique is proposed to equalize the

nonlinear response of the hydrophone pre-amplifier. A multi-branch combining structure is also incorporated to address the potential distortion introduced by the passband-to-baseband conversion. The performance of the proposed digital SI canceller is evaluated in the tank/lake experiments.

### **Adaptive filter with a delay**

In time-invariant channels, the SI can be effectively cancelled by classical RLS adaptive filters, such as the sliding-window RLS (SRLS) or exponential-window RLS (ERLS), but their SIC performance degrades in time-varying channels. Their performance can be improved by delaying the filter inputs. Thus, delayed versions of the SRLS and ERLS adaptive filters are considered. The dependence between the delay of the input signals and the SIC performance for the ERLS and SRLS adaptive filters is investigated.

### **Interpolating adaptive filtering algorithms**

The fast time-varying nature of the SI channels raises high requirements to the tracking performance of the adaptive filters. The interpolating adaptive filtering provides better channel estimation performance compared to the classical predictive adaptive filters in fast-varying channels. Based on this, new SRLS adaptive filter which exploits parabolic approximation of the time-varying SI channel response is proposed. Interpolating adaptive filtering algorithms based on the SRLS algorithm and basis expansion model (BEM) approach are further proposed for channel estimation in fast-varying channels. A sparse adaptive filtering algorithm based on the homotopy iterations is proposed to exploit the sparsity in the expansion coefficients of the BEM. The performance of the proposed algorithms in time-varying channels is investigated and compared with that of classical adaptive filters in simulations and lake experiments.

### **New evaluation metric for measuring the SIC performance**

The use of interpolating estimators makes the generally used mean squared error (MSE) not suitable for evaluating the cancellation performance, as the same data is used for training and

evaluation. A new evaluation metric, SIC factor (SICF), is proposed for measuring the SIC performance. The computation of the SICF takes into account the distortion of the far-end signal due to the over-fitting. It is applicable for both predictive and interpolating adaptive filters. To validate the applicability of the SICF, it is compared with other commonly used metrics in different simulation scenarios.

### **SIC schemes with multiple antennas**

Investigations on SIC schemes with multiple antennas are presented. A two-stage SIC scheme with two hydrophones is proposed to deal with the fast channel variation introduced by the moving surfaces. In the first stage, classical adaptive filters are used to cancel the strong and stable direct path at each hydrophone. In the second stage, the fast-varying surface reflections are eliminated by adaptive beamforming. Technically, it is possible to cancel all the SI in digital domain without acoustic cancellation for FD UWA systems. However, it would be beneficial to remove a certain amount of SI in acoustic domain before digital cancellation. This could also avoid the nonlinear distortion caused by the hydrophone pre-amplifier due to the high acoustic level and increase the resolution of the far-end desired signal. To this end, an acoustic-domain SIC scheme with two projectors and one hydrophone is proposed. The primary projector emits the data for the far-end user and is treated as the source of the near-end SI. The signal transmitted by the secondary projector is adjusted in such a way to produce a cancellation signal to cancel the near-end SI at the hydrophone.

## **1.7 Thesis structure**

The remainder of the thesis is organized as follows.

In Chapter 2, a general structure of the digital SI canceller is proposed to address the imperfections introduced in the transmit and receive chain. A multi-branch combining scheme is also incorporated to address the distortion introduced by the passband-to-baseband conversion. The performance of the proposed digital SI canceller is evaluated using experimental data.

Chapter 3 investigates the SIC performance of the adaptive filters in time-varying channels. A new metric is proposed for evaluating the SIC performance in FD UWA systems. A new SRLS based algorithm with parabolic interpolation is proposed for SI channel estimation in fast-varying channels. The performance of the proposed adaptive filter is investigated and compared with classical adaptive filters via both simulation and lake experimental data.

Chapter 4 proposes new interpolating adaptive filtering algorithms which combine the SRLS adaptive filter with BEM for SI channel estimation in FD UWA systems. To exploit the sparsity in the expansion coefficients, a sparse adaptive filtering algorithm based on homotopy iterations is also proposed. The identification performance of the proposed algorithms is evaluated in both simulation and lake experiments.

In Chapter 5, SIC schemes with multiple antennas in FD UWA systems are presented. An acoustic-domain SIC scheme with two projectors is presented. The acoustic cancellation performance is evaluated by the residual SI level and the detection performance via simulations with virtual far-end transmission. A two-stage SIC scheme with two hydrophones is proposed to provide another insight for eliminating the fast-varying surface reflections.

In Chapter 6, we conclude the thesis and discuss directions of further work.

In Appendix A, pictures of the lake surface are presented to demonstrate the surface conditions during lake experiments. In Appendix B, detailed derivation of the channel estimate obtained by the SRLS algorithm is given. Complexity of the local basis function (LBF) and HSRLS-L-DCD algorithms is analysed in Appendices C and D, respectively.



## Chapter 2

# General Structure of the Digital Self-Interference Canceller

In this chapter, a general structure of the digital SI canceller is proposed regarding the major factors affecting the digital cancellation performance. In Section 2.1, digital SI cancellers with different reference signals are investigated. The SIC structure using the PA output as the reference signal is adopted to take into account the nonlinear distortion introduced by the PA. This structure is extended in Section 2.2 to reduce the signal distortion caused by the passband-to-baseband conversion. In Section 2.3, an adaptive nonlinear equalizer is proposed to reduce the nonlinear distortion introduced by the hydrophone pre-amplifier thus improving the digital cancellation performance. Finally, conclusions are drawn in Section 2.4.

The work in this chapter is presented in the papers: L. Shen, B. Henson, Y. Zakharov, and P. Mitchell, “Digital self-interference cancellation for full-duplex underwater acoustic systems,” *IEEE Transactions on Circuits and Systems II: Express Briefs*, vol. 67, no. 1, pp. 192–196, 2019; L. Shen, B. Henson, Y. Zakharov, and P. Mitchell, “Robust digital self-interference cancellation for full-duplex UWA systems: Lake experiments,” in *Underwater Acoustics Conference and Exhibition*, 2019, pp. 243–250; L. Shen, B. Henson, Y. Zakharov, and P. D. Mitchell, “Adaptive nonlinear equalizer for full-duplex underwater acoustic systems,” *IEEE Access*, vol. 8, pp. 108 169 – 108 178, 2020.

## 2.1 Digital SIC structure addressing the PA nonlinearity

A linear filter is normally used to model the SI channel for digital cancellation. However, the digital cancellation performance can be limited due to the nonlinear distortions introduced in the transmit and the receive chains. It is known that the majority of the nonlinear distortions comes from the PA, and the rest of the nonlinear distortion is introduced by the hydrophone pre-amplifier and the transducer.

One approach to address the PA nonlinearity is to estimate the nonlinear SI channel. This could be done by either using two-step digital cancellation scheme (cancel the linear and nonlinear SI components separately) [21] or by developing a nonlinear adaptive filter [39] or by predistorting the reference signal for digital cancellation based on the estimate of PA characteristics [40, 82]. These designs obtain up to 48 dB of digital SIC at the expense of high complexity [21, 39, 41]. Another approach to dealing with the PA nonlinearity without developing a high complexity digital SI canceller is to use the PA output as a reference signal [42]. In such a case, a linear canceller can be sufficient. In [42], this idea is investigated by simulation for multi-carrier communication signals.

In this section, a low-complexity practical digital SI canceller is proposed for FD UWA systems, which uses the PA output to reduce the effect of the PA nonlinearity on the SIC performance. The performance of the proposed digital SI canceller is evaluated by the experimental data from an indoor water tank experiment. As demonstrated by the experimental result, a significantly higher level of SIC is achieved compared to reported experimental results for FD terrestrial radio and UWA systems.

### 2.1.1 Digital SI canceller with two cancellation modes

The FD system structure with the proposed digital SI canceller is shown in Fig. 2.1. The system operates at two sampling rates. The high sampling rate  $f_s$  is used for sampling the received signal. The lower sampling rate  $f_d$  is used for SI channel estimation and digital cancellation. The sample index with the high sampling rate  $f_s$  and the low sampling rate  $f_d$

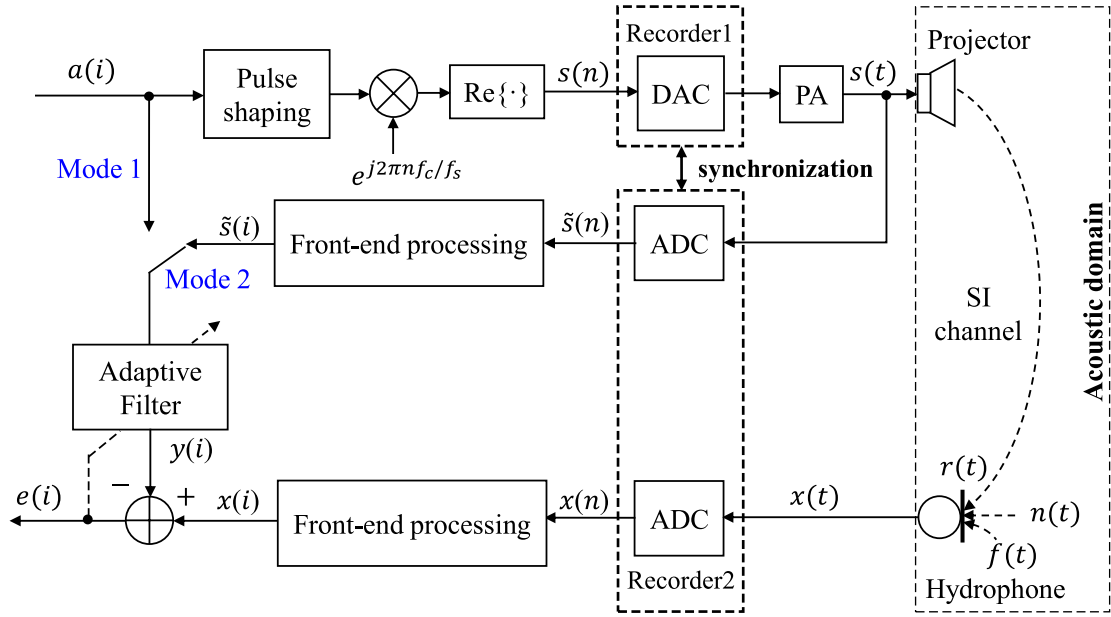


Fig. 2.1 Block diagram of the FD UWA system. Two cancellation modes with different reference signals are considered. The recorders are synchronized to avoid having different sampling rates in the transmit and receive chains.

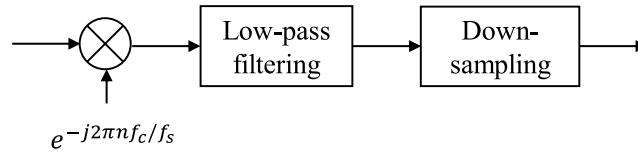


Fig. 2.2 Front-end processing.

are denoted by  $n$  and  $i$ , respectively; e.g, the transmitted signal  $s(t)$  sampled at  $f_s$  is denoted as  $s(n)$ .

We consider transmitting a pseudo-random sequence of complex data symbols  $a(i)$ . The transmitted data is up-sampled from  $f_d$  to  $f_s$ , pulse-shape filtered and up-converted to the carrier frequency  $f_c$ . The root-raised cosine (RRC) filter [83] is used for the pulse-shaping [84]. Then, the passband signal  $s(n)$  is digital-to-analogue converted (DAC), amplified in the PA and transmitted by a projector. The SI channel output  $r(t)$  along with the far-end desired signal  $f(t)$  and the noise  $n(t)$  are received by the near-end hydrophone. The far-end signal  $f(t)$  is transmitted over the same frequency band as the near-end transmission. Note that the far-end signal introduces additional interference at the hydrophone that degrades the SI channel estimation performance. In this section, the aim is to evaluate the baseline performance

of the digital SIC, therefore the far-end transmission is not considered in the experiments. It is known that the adaptive filtering could cause distortion to the far-end signal. The distortion of the far-end signal is taken into account in the evaluation metric presented in Section 3.2.2.

We use an adaptive filter for SI channel estimation and SI signal reconstruction. As shown in Fig. 2.1, the system can switch between two modes. In mode 1, the transmitted digital data  $a(i)$  is used as the regressor in the adaptive filter. In mode 2, the baseband samples  $\tilde{s}(i)$  of the analogue output  $s(t)$  of the PA are used as the regressor. After the ADC, the digitalized PA output is front-end processed as shown in Fig. 2.2, where  $\tilde{s}(n)$  is down-converted, low-pass filtered by an RRC filter and downsampled to  $f_d$  before being used as the adaptive filter input. The received signal  $x(t)$  undergoes the same front-end processing as the analogue PA output  $s(t)$  before being used as the desired signal  $x(i)$  in the adaptive filter [59]. The downsampling of the input signal before the adaptive filtering is used to reduce the computational complexity and to avoid the ill-condition problem caused by a high condition number of the autocorrelation matrix of the narrowband regressor [59].

It is reasonable to assume that the SI channel is not static in sea environments. In most scenarios, apart from the direct SI path between the projector and the hydrophone, there are reflections from the moving sea surface. The channel coherence time can be as short as 70 ms [64]. Thus, fast convergence speed is one of the main features we are interested in. Another objective is to implement the SIC algorithm on a real-time design platform, such as a DSP board [85]. Therefore, the computational complexity and numerical stability are also crucial factors for algorithm selection. The fastest convergence is achieved by the classical RLS algorithm, but it suffers from numerical instability and possesses high computational complexity. The numerical instability is a consequence of the recursive matrix inversion. This recursion allows a reduced complexity of an order of  $L^2$  arithmetic operations per sample, which however is still too high for practical implementation.

We use the ERLS algorithm with dichotomous descent (DCD) iterations (ERLS-DCD) that has a convergence speed comparable to that of the classical ERLS algorithm, it is numerically stable and has a significantly lower complexity [86]. Moreover, the ERLS-DCD algorithm is well suited to implementation in fixed-point arithmetic, in particular, in

hardware [86, 87]. Instead of the matrix inversion, it solves a system of normal equations, thus making the algorithm numerically stable. For the solution, it uses DCD iterations. Its impulse response is only updated for each successful DCD iteration, in which the cost function is reduced. The ERLS-DCD algorithm requires an order of  $LN_u$  operations per sample, where  $N_u$  is the number of DCD updates, and  $N_u \ll L$ . With  $N_u = 2$ , as is in our experiments, the complexity of the ERLS-DCD algorithm is comparable with that of the normalized least mean squares (NLMS) adaptive filter, considered to be one of the least complicated algorithms [87].

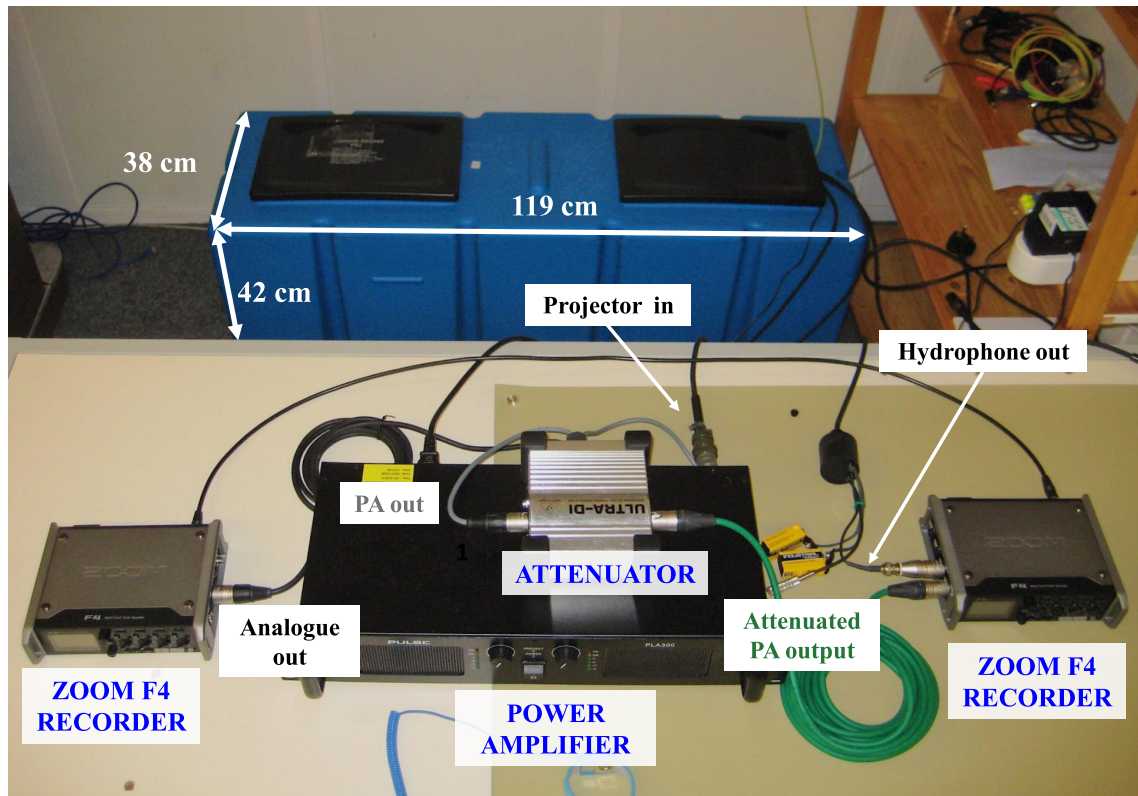
### 2.1.2 Digital SIC performance under two cancellation modes

#### Experimental setup

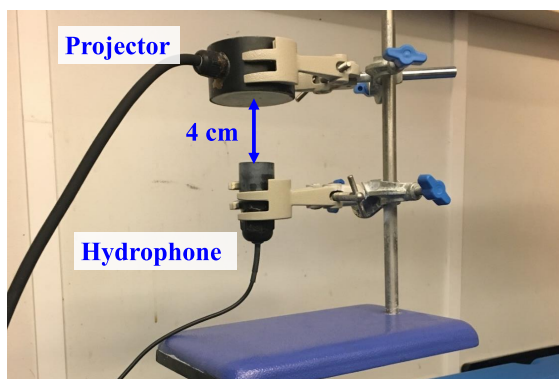
In our experiment, we transmit binary phase-shift keying (BPSK) symbols at the carrier frequency  $f_c = 12$  kHz. The symbol rate is  $f_d = 1$  kHz. The RRC roll-off factor is 0.2 and the filter length is of a duration of 14 symbols (14 ms). A Hanning window is applied to the filter coefficients to avoid the edge effects due to the truncation of the RRC impulse response. The length of the transmitted signal is 15 s, which includes 5 s of zero padding before the data transmission. The received signal during this silence period is used to measure the background noise in the water tank.

Fig. 2.3 (a) shows the experimental setup. We use a Benthowave BII-7530 projector [78] for the near-end data transmission and a Benthowave BII-7010 hydrophone [80] for the SI reception. As shown in Fig. 2.3 (b) and (c), the projector and hydrophone are clamped by a retort stand with a fixed distance between them of 4 cm and submerged in the water during the experiment.

The passband digital samples  $s(n)$  of the transmitted signal are generated in MATLAB and stored in an SD card of a Zoom F4 multitrack recorder [74]. This recorder converts these samples to an analogue signal with a 24-bit DAC and passes it to the PULSE PLA300 power amplifier [75]. Finally, the amplified analogue signal is fed to the projector and transmitted.



(a)



(b)



(c)

Fig. 2.3 (a) Experimental setup of the FD UWA system. The plastic water tank is filled with 120 litre of water. (b) Placement of the projector and hydrophone underwater. (c) Vertical view of the tank.

As mentioned in Section 2.1.1, the system has two modes of digital cancellation. The second mode requires access to the PA output to generate the regressor for the adaptive filter. The hydrophone output and PA output are recorded by the same recording device during the experiment. In our experiments, the PA output and the hydrophone output are recorded using a Zoom F4 multitrack recorder at a sampling rate of 96 kHz. The recorder contains a high resolution 24-bit ADC to avoid introducing high quantization noise. Although we use the same type and model of recorders for data transmission and reception, the sampling rates generated by the two oscillators in the recorders might not be identical. Thus, we have synchronized the audio clock of the two recorders to avoid a difference between the sampling rates in the transmit and receive chains.

Due to the high voltage level of the PA output (up to 48 V in our experiments), the PA output is attenuated by the Behringer DI100 attenuator [77] before being fed to the recorder.

### Experimental results

In this section, the tank experimental results of the digital SI cancellers are presented. The digital SIC performance is evaluated by the steady-state normalized mean-squared error (NMSE) level of the adaptive filter. The NMSE at the  $i$ th time instant is computed as:

$$\text{NMSE}(i) = \frac{|e(i)|^2}{P_x} = \frac{|e(i)|^2}{\mathbf{x}^H \mathbf{x} / N}, \quad (2.1)$$

where  $e(i)$  is the  $i$ th sample of the error vector,  $P_x$  is the average power of the desired signal vector  $\mathbf{x} = [x(1), \dots, x(i), \dots, x(N)]^T$ , and  $N$  is the total number of samples in the error signal. The steady-state NMSE level is computed as an average of the instantaneous NMSE from 5 s to about 10 s of the received signal after the silence period.

In Fig. 2.4, a snapshot of the SI channel estimate in the water tank is plotted. This channel estimate represents the adaptive filter taps after convergence of the ERLS-DCD algorithm in the second (more accurate) mode. It can be seen that we have a long impulse response with a delay spread of around 80 ms.

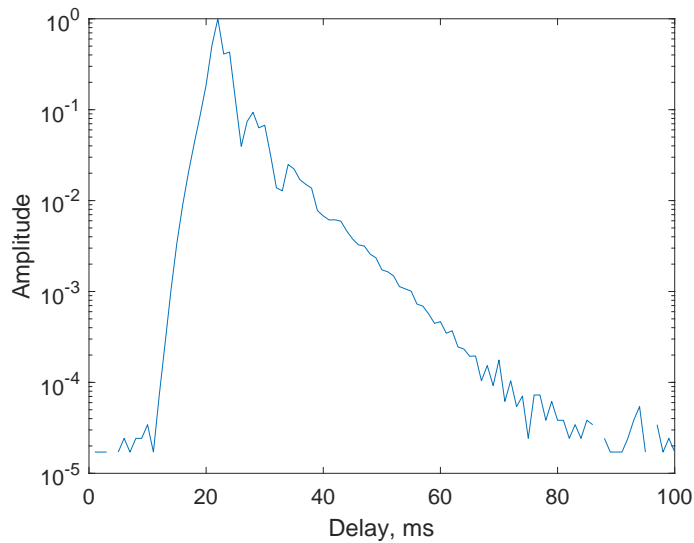


Fig. 2.4 Impulse response estimate of the SI channel in the water tank experiment. The magnitude of the impulse response is shown in log scale due to its high dynamic range.

In Fig. 2.5, we show the NMSE performance of the NLMS and ERLS-DCD algorithms in the second mode. The filter length is  $L = 100$ , which is sufficient for the channel delay spread in the water tank. The algorithm parameters are tuned to achieve the same steady-state NMSE level. The NLMS step-size is  $\mu = 0.3$ . For the ERLS-DCD algorithm, the forgetting factor is  $\lambda = 1 - 1/4L = 0.9975$ , the number of bits representing the impulse response is  $M_b = 16$ , and the number of updates is  $N_u = 2$  [86]. The NMSE curves are smoothed by averaging the instantaneous NMSE over a period of 15 ms to provide a better vision of the NMSE performance for comparison. The ERLS-DCD algorithm clearly shows a faster convergence speed than the NLMS algorithm.

In Fig. 2.6, we compare the digital SIC performance of the ERLS-DCD algorithm in the two modes. Parameters of the ERLS-DCD algorithm are the same as we used for NMSE performance comparison. With the aforementioned parameters, we achieve the same steady-state NMSE level as the classical ERLS algorithm (not shown here). The NMSE curves are again smoothed in the same way to provide a clearer vision. As shown in Fig. 2.6, when we use the digital data as the regressor, the steady-state NMSE level is close to  $-46$  dB.

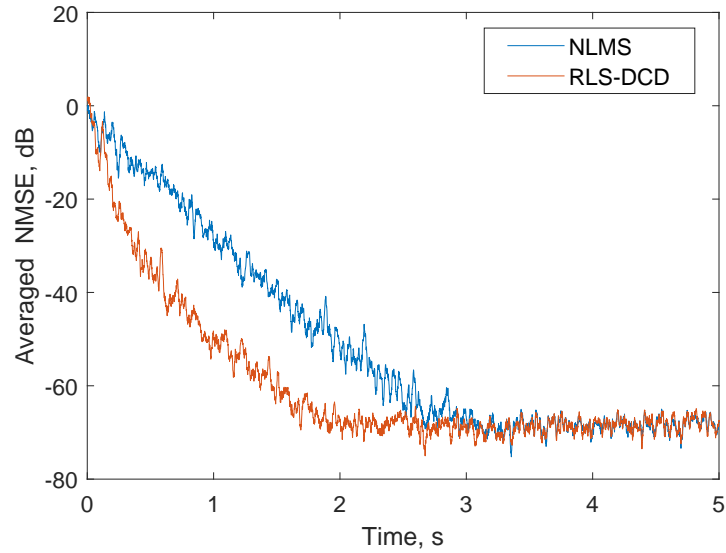


Fig. 2.5 Averaged NMSE performance of the NLMS and RLS-DCD algorithms.

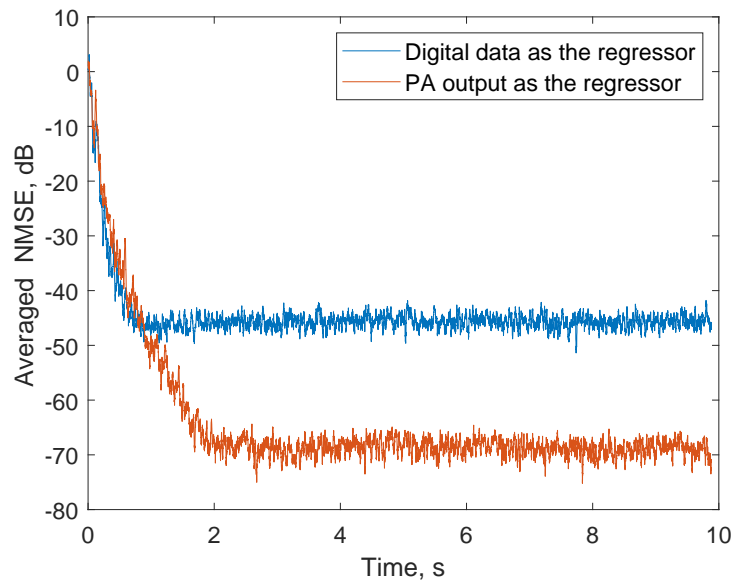


Fig. 2.6 Averaged NMSE performance in the two cancellation modes. The original digital signal and ADC-converted PA output signal are used as the regressors in mode 1 and 2, respectively.

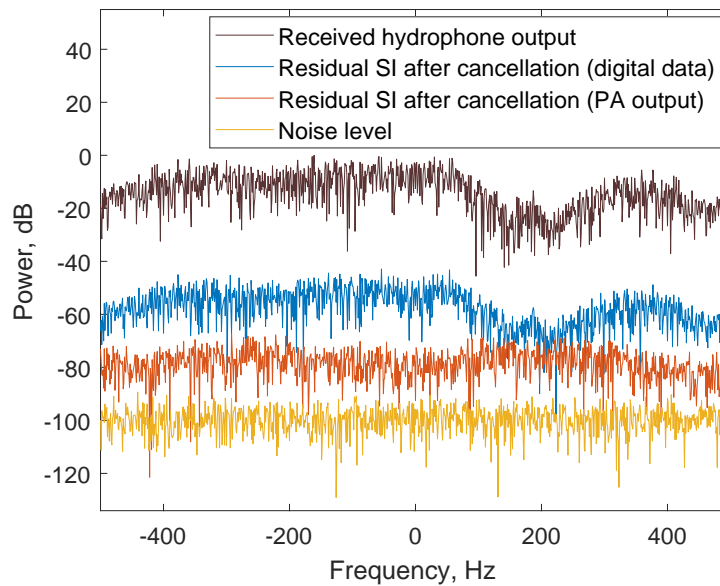


Fig. 2.7 Power spectra of the received signal before and after the digital cancellation.

However, the NMSE level can be further reduced to  $-66$  dB with the PA output being used as the regressor.

The spectra of the received signal before and after digital cancellation are shown in Fig. 2.7. Both the NMSE performance and the signal spectra demonstrate that the digital cancellation when using the PA output as the regressor significantly outperforms that with the digital data. We believe that the observed 20 dB improvement in SIC in the second mode is achieved by taking into account the nonlinear distortions introduced by the PA.

It can be seen in Fig. 2.7 that the residual signal after digital cancellation is still 20 dB higher than the noise floor. This can be attributed to the residual nonlinear distortions introduced by other equipment rather than the PA and the long reverberation time in the tank. For example, the hydrophone we use has an integrated pre-amplifier. The pre-amplifier will introduce extra nonlinear distortion to the received signal which is not taken into account with a linear adaptive filter. Further discussion on the nonlinearity of the hydrophone pre-amplifier will be given in Section 2.3.

## 2.2 Extended structure of the digital SI canceller

In Section 2.1, a low-complexity digital canceller design using the PA output as the reference signal is proposed. With this approach, a linear digital canceller can be sufficient for modelling the SI channel, since the nonlinear distortion introduced by the PA is incorporated into the reference signal. In our experiments, it has been observed that the performance of the digital canceller is significantly affected by the choice of the sampling time instant of the passband to baseband conversion. In this section, a multi-branch combining scheme is incorporated into the digital SI canceller structure to ensure that the robust cancellation performance can be achieved regardless the choice of the sampling time instant.

### 2.2.1 Sampling instant of the passband to baseband conversion

For digital cancellation, the SI channel estimation is done in the baseband using an adaptive filter. To obtain the baseband equivalent signals, the digitalized PA output and the received signal are demodulated to the baseband, low-pass filtered and decimated to the baseband sampling rate  $f_d$  in the front-end processing block (see Fig. 2.2). From our observation, the choice of the passband sampling time instant of the passband to baseband conversion is crucial for the SIC performance. Even a slight shift (within the baseband sampling interval  $T_d = 1/f_d$ ) in the sampling time might cause significant degradation in the SIC performance.

As an example, we start the passband to baseband conversion at two sampling time  $t_1$  and  $t_2$  to obtain the PA outputs  $\tilde{s}_{t_1}(i)$  and  $\tilde{s}_{t_2}(i)$ . The sampling delay between the two sampling time instants is  $0.3T_d$ , which is only a fraction of the time delay corresponding to one tap of the adaptive filter. The channel estimates obtained with the two PA outputs are shown in Fig. 2.8. With the channel estimate shown in Fig. 2.8 (a), a good digital SIC performance is achieved. On the other hand, the channel estimate shown in Fig. 2.8 (b) contains a wide spread of arrivals arrive earlier than the direct path. Meanwhile, the SIC performance in the second case is much worse compared to that in the first case.

In Fig. 2.9, the NMSE performance of the digital canceller in the tank experiment is plotted against the sampling delay. The baseband hydrophone output is obtained by starting

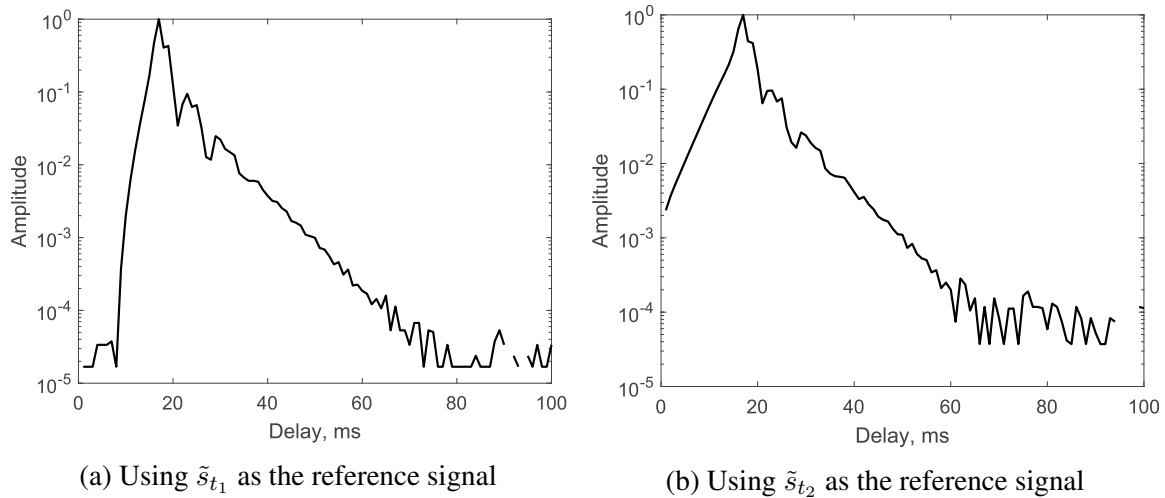


Fig. 2.8 Estimates of the magnitude of the SI channel impulse response in the tank experiment. The channel estimates are obtained by the ERLS adaptive filter with the same desired signal and two time-shifted baseband PA outputs.

the baseband to passband conversion at time  $t_1$ , and the start sampling time of the PA output is denoted as  $t_2$ . The sampling delay is defined as the time difference between  $t_1$  and  $t_2$ . In the tank experiment, the baseband sampling frequency is the same as the symbol rate, and the symbol interval is 1 ms. We consider a range of sampling delay from 0 to 4 ms. It can be seen that the NMSE performance varies significantly even within one symbol duration. As high as 45 dB difference in the NMSE performance can be observed. Similar phenomenon is also reported in [84] regarding the equalizer performance in a band-limited channel.

## 2.2.2 Multi-branch combining scheme

The key idea of the multi-branch combining scheme is to have two time-shifted copies of the baseband PA output as the reference signals to perform digital cancellation in two branches. This is motivated by the dependence of the NMSE performance on the sampling delay shown in Fig. 2.9. It is seen that reliable NMSE performance can be achieved with more than half of the sampling delays within one symbol interval. If the PA output is sampled starting at two sampling instants differing by half symbol duration, we can ensure that a good SIC performance can be achieved at one or both of the branches. The two residual signals are then combined with weight coefficients computed based on the residual variance estimates.

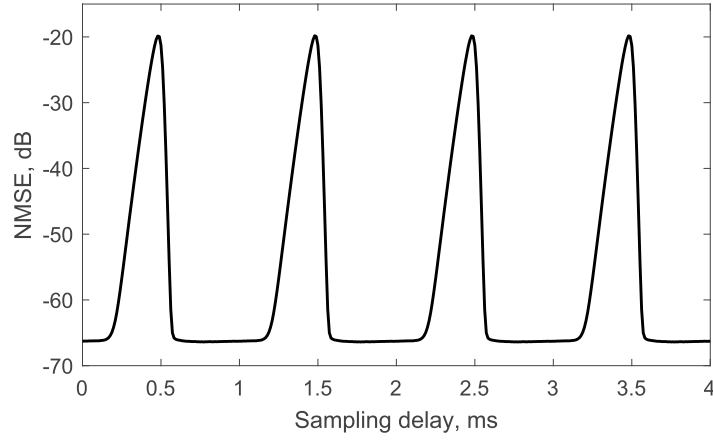


Fig. 2.9 NMSE performance of the digital canceller with different sampling delay in the water tank experiment.

The block diagram of the extended structure of the digital SI canceller is shown in Fig. 2.10. The digitalized PA output  $s(j)$  is now oversampled to twice the symbol rate ( $2f_d$ ). The digital samples  $s(j)$  are interleaved into two branches, with odd samples in signal  $s_1(i)$ , while even samples in  $s_2(i)$ ;  $s_1(i)$  and  $s_2(i)$  are used as the regressors of the two adaptive filters in the first and second branch, respectively. After digital cancellation, the residual signals  $e_1(i)$  and  $e_2(i)$  are combined with different weight coefficients which are computed based on the residual variance estimates in the two branches. The variance on the  $k$ th branch ( $k = 1, 2$ ) at the  $i$ th time instant is estimated by:

$$\sigma_k^2(i) = \alpha \sigma_k^2(i-1) + (1-\alpha) |e_k(i)|^2, \quad (2.2)$$

where  $\alpha$  is a forgetting factor. The weight coefficients  $w_k(i)$  are then computed by:

$$w_k(i) = \frac{1}{\sigma_k^2(i)} \bigg/ \left( \frac{1}{\sigma_1^2(i)} + \frac{1}{\sigma_2^2(i)} \right). \quad (2.3)$$

According to the combining scheme, a small weight coefficient is applied to the branch with high variance (residual signal power), and a large weight coefficient is applied to the branch with high level of SIC. As the sum of the weights equals to one, the level of the

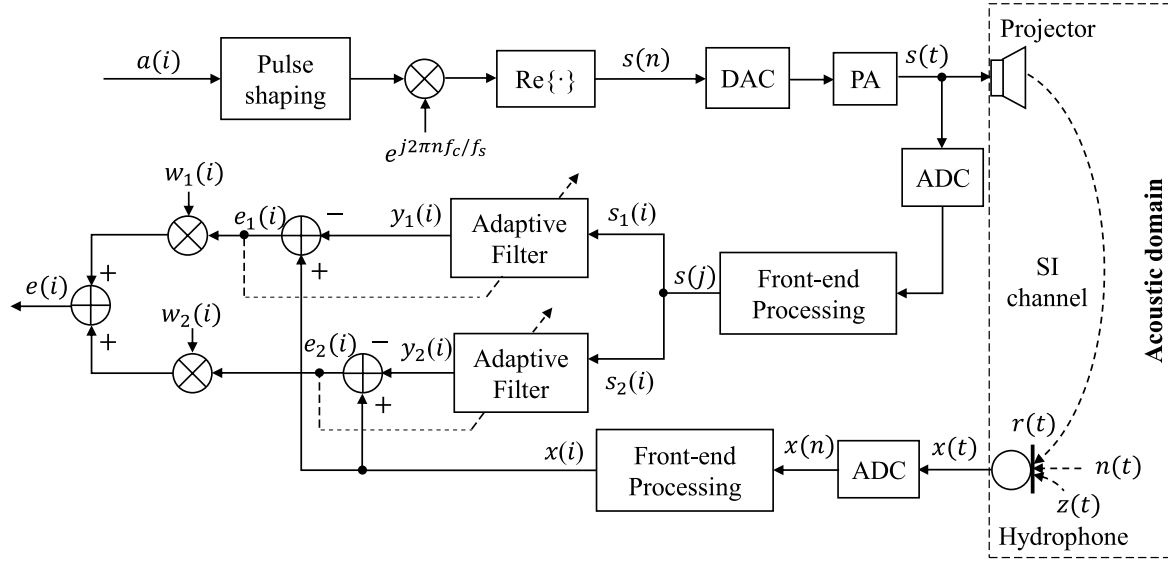


Fig. 2.10 Block diagram of the extended structure of the digital SI canceller. The sample index with sampling rate  $f_s$ , symbol rate  $f_d$  and  $2f_d$  are denoted by  $n$ ,  $i$  and  $j$ , respectively.

received signal is not changed after combining. With this approach, robust SIC performance can be achieved at any sampling time.

### 2.2.3 Evaluation of the extended digital SI canceller

In this section, we investigate the SIC performance in water tank and lake experiments.

#### Tank Experiment

The tank experiment is conducted in the indoor water tank described in Section 1.5. During the experiments, the projector [78] and hydrophone [80] are clamped by a retort stand, separated by 4cm and submerged underwater as shown in Fig. 2.3.

We transmit a BPSK modulated signal with a sampling frequency of  $f_s = 96$  kHz and a carrier frequency of  $f_c = 12$  kHz. The frequency bandwidth is 1.2 kHz. The RRC filter we use has a roll-off factor of 0.2 and a filter length of 14 symbols duration (14 ms). A Hanning window is applied to the RRC filter taps to achieve higher attenuation at the edge of the filter. The transmitted signal length is 15 s, which includes 5 s of zero padding at the beginning of the signal. This silence period is used to measure the background noise level. Here we use

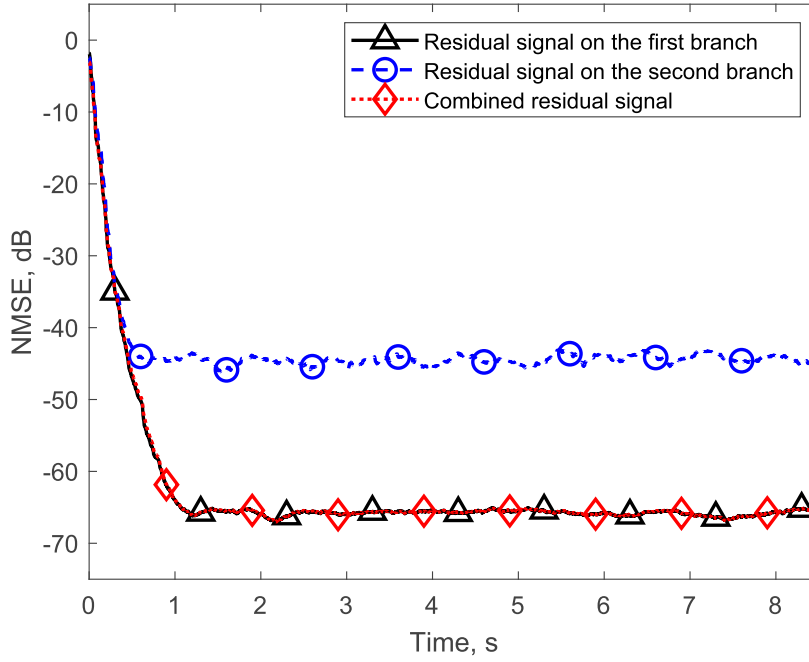


Fig. 2.11 Averaged NMSE performance in the tank experiment. Residual signals in the first and second branches refer to  $e_1(i)$  and  $e_2(i)$  in Fig. 2.10, respectively.

the NMSE level as the indicator for the cancellation performance. The NMSE level at the  $k$ th branch ( $k = 1, 2$ ) is computed by:

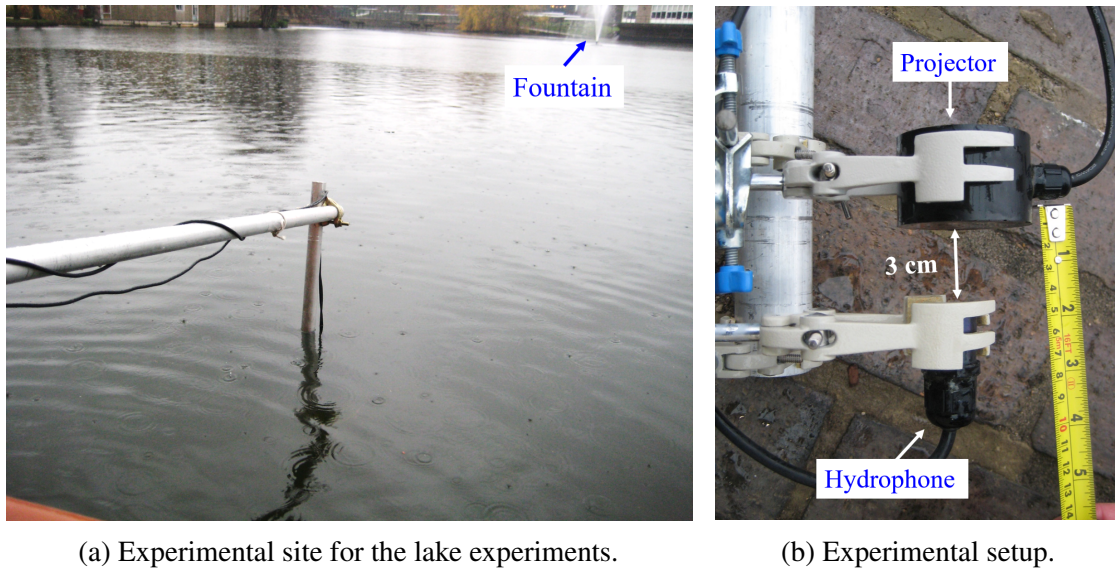
$$\text{NMSE}(i) = \frac{P_e}{P_x} = \frac{|e_k(i)|^2}{P_x}, \quad (2.4)$$

where  $P_x = \sum_{i=0}^{N-1} |x(i)|^2 / N$  is the average power of the desired signal of the adaptive filter,  $N$  is the length of the desired signal,  $P_e = |e_k(i)|^2$  is the instantaneous power of the residual signal  $e_k(i)$ . The NMSE level after combining is computed by:

$$\text{NMSE}(i) = \frac{P_{e_c}}{P_x} = \frac{|e(i)|^2}{P_x}, \quad (2.5)$$

where  $P_{e_c}$  is the instantaneous power of the combined residual signal  $e(i)$ . The steady-state NMSE is computed by averaging the NMSE over the last five seconds of the signal.

Fig. 2.11 shows the NMSE performance in the tank experiment. The NMSE curves are smoothed by averaging the instantaneous NMSE over a period of 0.3 s to provide a



(a) Experimental site for the lake experiments.

(b) Experimental setup.

Fig. 2.12 Transducer configuration and the experimental site for the lake experiments.

clearer view. The length of the adaptive filter is  $L = 100$ , which is long enough to capture the SI channel delay spread. The forgetting factor is  $\lambda = 0.995$ . The parameters of the DCD iterations are chosen as follows: the number of bits representing the impulse response is  $M_b = 16$ , and the number of DCD updates is  $N_u = 4$ . The forgetting factor used for the variance estimation is  $\alpha = 0.95$ . As can be seen in Fig. 2.11, for the first branch, the steady-state NMSE is around  $-66$  dB, while in the second branch the NMSE level is more than 20 dB higher than that in the first branch. The NMSE level of the combined residual signal is approximately the same as that in the first branch after combining the signals in the two branches, showing the effectiveness of the combining scheme.

### Lake experiment

To evaluate the SIC performance in a more practical scenario, lake experiments were conducted. The experimental site is shown in Fig. 2.12 (a). In the lake experiments, the projector and the hydrophone are placed at a depth of 0.5 m, the distance between them is 3 cm (see Fig. 2.12 (b)).

The NMSE performance in the lake experiment is shown in Fig. 2.13. The NMSE curves are smoothed by averaging the instantaneous NMSE over a period of 0.5 s. The averaging

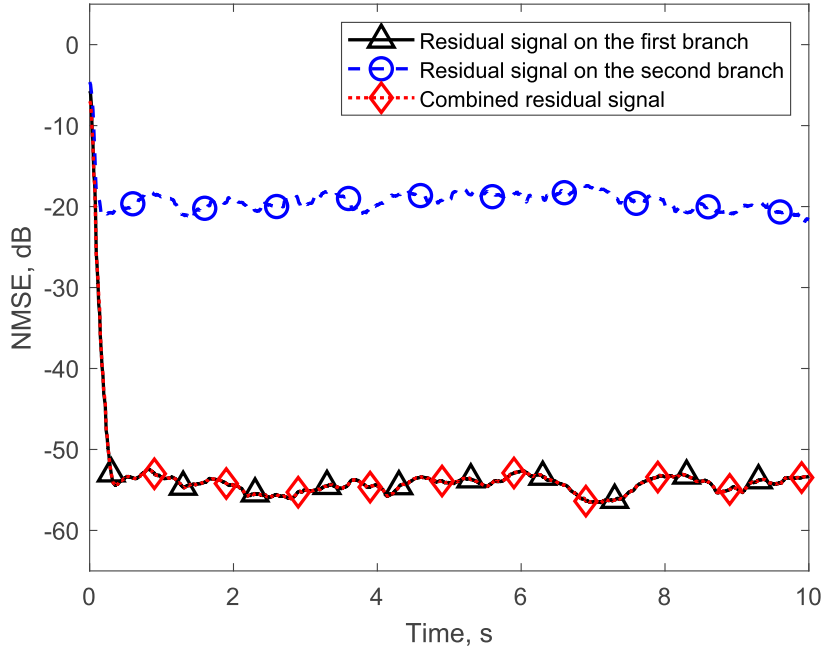


Fig. 2.13 Averaged NMSE performance in the lake experiment. Residual signal in the first and second branches refer to  $e_1(i)$  and  $e_2(i)$  in Fig. 2.10, respectively.

time window used here is longer compared to that of the tank experiment (0.3 s). This is due to the higher fluctuations in the NMSE curves, which are caused by faster time-variation of the SI channel in the lake. We use an adaptive filter length of  $L = 60$ , and a forgetting factor  $\lambda = 0.985$ . As less number of reflections are received in the lake, a shorter filter length is used. For the DCD iterations, the number of bits representing the impulse response is  $M_b = 16$ , and the number of DCD updates is  $N_u = 4$ . The forgetting factor used for the residual variance estimate is  $\alpha = 0.9$ . It can be seen that the steady-state NMSE in the first branch is around  $-54$  dB. For the second branch, the NMSE performance is significantly worse. After combining, the NMSE level of the combined residual signal is at the same level as that of the first (better) branch.

Note that for both the tank and lake experiments, the ERLS-DCD algorithm achieves the same steady-state NMSE level as the classical ERLS algorithm, but with significantly lower complexity. The experimental results in the water tank and lake experiments demonstrate that robust and high level SIC can be achieved with the proposed digital cancellation scheme regardless of the sampling time. The lower level of SIC achieved in the lake experiments

can be explained by faster SI channel variation in the lake experiments attributed by several environmental factors, including the time-varying lake surface. Development of the adaptive filtering algorithms targeting at the time-varying SI channels due to the moving surface waves will be given in Chapters 3 and 4.

## 2.3 Adaptive equalization of the nonlinearity in the hydrophone pre-amplifier

As illustrated in section 2.1, the factors limiting the digital cancellation performance are the nonlinear distortions introduced by the PA in the transmit chain [34], hydrophone pre-amplifier and transducers [50]. In the previous sections, it is shown that the PA nonlinearity can be dealt with by using the PA output as the reference signal for digital cancellation. Without the limitation of PA nonlinearity, the major obstacle comes from the nonlinear distortion introduced by the hydrophone pre-amplifier. In this section, we propose an adaptive equalizer to equalize the nonlinear distortion introduced by the pre-amplifier. The performance of the proposed equalizer is evaluated through two sets of water tank experiments.

### 2.3.1 Adaptive nonlinear equalization

Hydrophones with a long cable normally have an integrated pre-amplifier to avoid the SNR loss. Pre-amplifiers have an almost linear response within a voltage limit. Beyond the limit, they become nonlinear and saturate [49]. In UWA applications operating in the half-duplex mode, the received signal is expected to be relatively weak, such that the pre-amplifier operates in the linear mode. For FD operations, the received signal could be quite strong as it includes both the far-end signal and the strong near-end SI. To achieve a high level of SIC, the nonlinear distortion introduced by the pre-amplifier must be taken into account.

In Fig. 2.14, a block diagram of the FD UWA system including the hydrophone pre-amplifier and an adaptive nonlinear equalizer is given. The received signal before and after the amplification is denoted as  $x(t)$  and  $\tilde{x}(t)$ , respectively. The passband digitalized signal

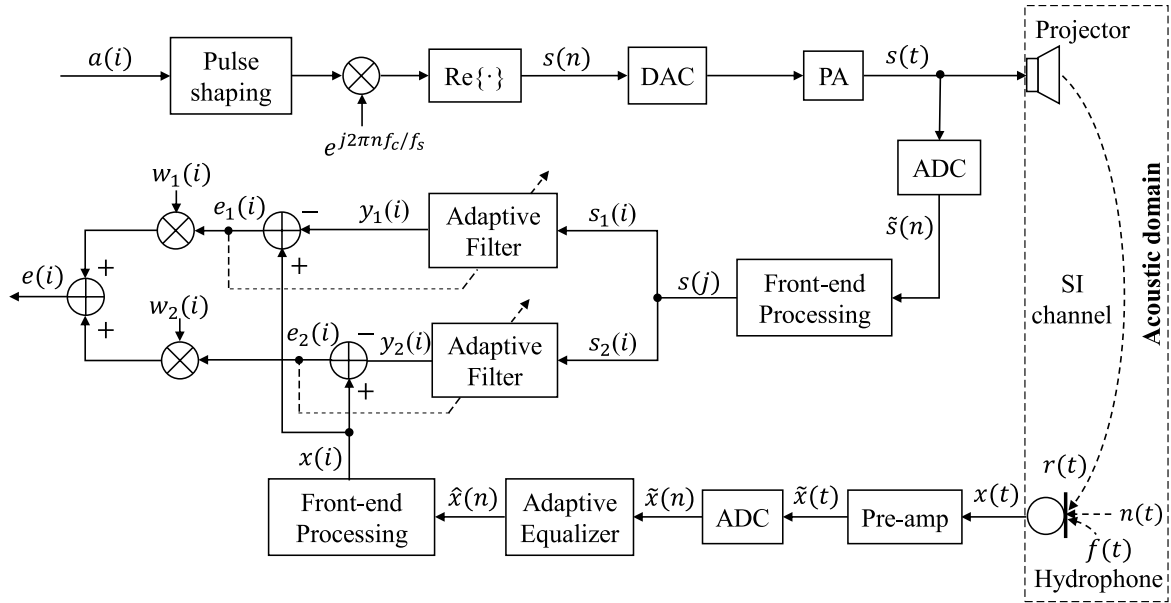


Fig. 2.14 Block diagram of the FD UWA system with nonlinear equalizer.

$\tilde{x}(n)$  is passed to the adaptive equalizer to equalize the nonlinear distortion introduced by the pre-amplifier. Afterwards, the equalized signal  $\hat{x}(n)$  is used as the desired signal in the adaptive filter performing the SI channel estimation.

The Legendre polynomials are used as the BEM for the nonlinear equalization. We assume that the nonlinearity is memoryless. The output of the equalizer can then be written as:

$$\hat{x}(n) = \tilde{x}(n) + \sum_{p \in P} c_p \phi_p(\tilde{x}(n)), \quad n = 1, \dots, N, \quad (2.6)$$

where  $c_p$  are expansion coefficients,  $\phi_p(\cdot)$  is the  $p$ th order Legendre polynomial,  $P$  is a set of Legendre polynomials and  $N$  is the number of samples used for equalization. The Legendre polynomials are defined on an interval  $[-1, 1]$  as shown in Fig. 2.15. Before being applied to the equalizer,  $\tilde{x}(n)$  is normalized to guarantee that the equalizer input is within this interval.

The general idea of the adaptive nonlinear equalizer is to find the expansion coefficients which minimize a cost function. The expansion coefficients are initialized to zero and the coordinate descent search is used for the update. Let  $\mathbf{u} = [-1, 1]$  be a direction vector with elements  $u(d)$ . At the  $m$ th iteration, for the  $d$ th direction, the  $p$ th expansion coefficient is

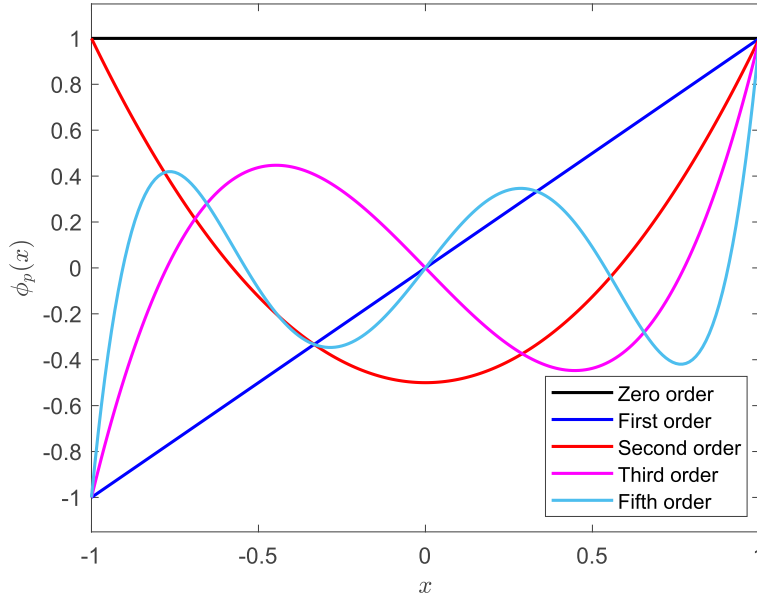


Fig. 2.15 Legendre polynomials.

updated as:

$$c_p^{(m)} = c_p^{(m-1)} + u(d) \cdot \delta, \quad (2.7)$$

where  $\delta$  is a step size. The step size is initialized to  $\delta = H$ , where  $H$  is the maximum possible value of the expansion coefficients; see [86] for more details on the choice of  $H$ . For each tentative update of the expansion coefficient, the equalized signal vector  $\hat{\mathbf{x}} = [\hat{x}(1), \dots, \hat{x}(N)]^T$  and a cost function are computed. If the cost function is reduced, the expansion coefficient  $c_p$  is updated in the direction which minimizes the cost function. If the expansion coefficients remain the same after going through all the basis functions, the step size is reduced by a factor of two.

### 2.3.2 The cost functions

Two cost functions are considered for the adaptive nonlinear equalization. The first one is based on the residual SI level after the SIC. If the nonlinear distortion introduced by the pre-amplifier is equalized, the SI estimation performance will be improved, and thus a lower residual SI level can be achieved. The MSE is used to represent the residual SI level at the adaptive filter output. Thus, the MSE is directly used as the cost function to evaluate

**Algorithm 1** Adaptive nonlinear equalizer (MSE-based)**Input:**  $\tilde{\mathbf{x}}$ **Output:**  $\hat{\mathbf{x}}$ Initialization:  $\mathbf{c}(0) = \mathbf{0}$ ,  $\delta = H$ Compute  $\text{MSE}_{\text{ref}} = \text{MSE}$  as a reference

---

```

for each iteration  $m$  do
  Compute  $\hat{\mathbf{x}}$  based on Equation (2.6)
  for the  $p$ th basis function do
    for the  $d$ th direction of search do
      Tentatively update  $c_p^{(m)}$  based on Equation (2.7)
      Compute the equalizer output  $\hat{\mathbf{x}}^{(m)}$ 
      Compute the MSE
    end
    if the MSE is reduced then
      Find the direction of update  $d$  minimizing the MSE
      For the optimal direction, update  $c_p^{(m)}$  based on Equation (2.7)
      Update  $\text{MSE}_{\text{ref}}$ 
    end
  end
  if  $\mathbf{c}$  has not changed in this iteration then
    Reduce the step size  $\delta$ :  $\delta \leftarrow \delta/2$ 
  end
end

```

---

the performance of the adaptive nonlinear equalizer. The algorithm of the equalizer with the MSE-based cost function is summarized in Algorithm 1. The MSE is computed at the beginning of the algorithm as a reference  $\text{MSE}_{\text{ref}}$ , which will be updated if the cost function is reduced.

The main drawback of using the MSE as the cost function is the high computational complexity. At each iteration, the SI canceller needs to be run  $2|P|$  times, where  $|P|$  (the cardinality of  $P$ ) is the number of basis functions used for equalization. In some applications, the equalization based on minimizing the MSE could be difficult to implement and therefore another cost function is proposed for reducing the complexity.

The other cost function is derived in the frequency domain based on the signal power spectrum. For a linearly amplified signal, the spectrum is centred at the carrier frequency  $f_c$ . When there are nonlinear distortions introduced in the amplification, the signal spectrum also contains higher order harmonics centred at multiples of  $f_c$ . If the nonlinearity is compensated by the equalizer, the power of the harmonics will be reduced. Therefore, we define the

cost function as the ratio of the powers of the harmonics over the fundamental signal power (harmonic-to-signal ratio, HSR), which is given by:

$$\text{HSR} = \frac{P_H}{P_S} = \frac{\sum_{q=2}^Q \sum_{k=f_3(q)/\Delta f}^{f_4(q)/\Delta f} |\hat{X}(k)|^2}{\sum_{k=f_1/\Delta f}^{f_2/\Delta f} |\hat{X}(k)|^2}, \quad (2.8)$$

and

$$\begin{aligned} f_1 &= f_c - B/2, & f_3(q) &= q(f_c - B/2), \\ f_2 &= f_c + B/2, & f_4(q) &= q(f_c + B/2), \end{aligned}$$

where  $P_H$  is the power of the harmonics,  $P_S$  is the fundamental signal power,  $Q$  is the highest order of the harmonics considered,  $B$  represents the signal bandwidth, which is equal to the symbol rate  $B = f_d$ ,  $\Delta f = f_s/N$  is the FFT frequency bin interval and  $\hat{X}(k)$  is computed as the FFT of the equalized signal  $\hat{\mathbf{x}}$ ,

$$\hat{X}(k) = \sum_{n=0}^{N-1} \hat{x}(n) e^{-j2\pi kn/N}, \quad k = 1, \dots, N. \quad (2.9)$$

It is found that, in some scenarios, using the HSR alone is not enough to guarantee good equalization performance. It occurs that the HSR can be reduced at the expense of higher sidelobes of the fundamental signal spectrum. It is shown in subsection 2.3.3 that the sidelobe level of the equalized signal can increase significantly compared to the original level (see Fig. 2.22) when using the HSR as the cost function. To avoid such situations, additional constraints need to be applied to the sidelobes around the fundamental signal.

The power of the sidelobes ( $P_{\text{SL}}$ ) can be computed as:

$$P_{\text{SL}} = \sum_{k \in B_{\text{SL}}/\Delta f} |\hat{X}(k)|^2, \quad (2.10)$$

where  $B_{\text{SL}} = [f_c - b, f_c - a] \cup [f_c + a, f_c + b]$  defines the frequency range of the sidelobes,  $b$  can be chosen to be as large as  $1.5B$  considering the wide spread of the sidelobes as shown

in Fig. 2.22 (f). The parameter  $a$  is chosen to be slightly larger than  $B/2$  to avoid including frequencies with high power within the transition region, in that case, the value of  $P_{\text{SL}}$  could not accurately reflect the level of the sidelobes.

The power of the sidelobes of the hydrophone output is computed at the start of the algorithm to be used as a reference  $P_{\text{ref}}$ . For each update of the expansion coefficients, we also compute  $P_{\text{SL}}$  of the equalized signal and compare it with  $P_{\text{ref}}$ . The  $p$ th expansion coefficient is updated if:

1. The updated sidelobe level is not increased ( $P_{\text{SL}} \leq P_{\text{ref}}$ ).
2. The updated sidelobe level is not much lower than the original level ( $P_{\text{SL}} > \eta P_{\text{ref}}$ , where  $\eta \in [0, 1]$  defines a threshold).

The second constraint is applied to avoid over-equalizing the hydrophone output. Since the PA output is used as the reference signal for SIC, it is undesirable to equalize the nonlinear distortion introduced by the PA. The threshold parameter  $\eta$  depends on the level of nonlinear distortion introduced by the hydrophone pre-amplifier. The stronger the nonlinearity of the pre-amplifier, the smaller threshold parameter should be set.

To compute the cost function, the FFT of the equalized signal needs to be re-computed for each tentative update of the expansion coefficients. To further reduce the complexity,  $\hat{X}(k)$  is updated in a recursive way by:

$$\hat{X}_{\text{new}}(k) = \hat{X}_{\text{past}}(k) + \delta \cdot u(d) X_{\phi}(p, k), \quad (2.11)$$

and

$$X_{\phi}(p, k) = \sum_{n=0}^{N-1} \phi_p(n) e^{-j2\pi kn/N}, \quad (2.12)$$

where  $X_{\phi}(p, k)$  is the FFT of the  $p$ th basis function which only needs to be computed once at the initialization. The algorithm with the HSR-based cost function is summarized in Algorithm 2. The HSR is computed at the beginning of the algorithm as a reference  $\text{HSR}_{\text{ref}}$ .

**Algorithm 2** Adaptive nonlinear equalizer (HSR-based)**Input:**  $\tilde{\mathbf{x}}$ **Output:**  $\hat{\mathbf{x}}$ Initialization:  $\mathbf{c} = \mathbf{0}$ ,  $\delta = H$ ,  $\hat{\mathbf{x}} = \tilde{\mathbf{x}}$ **for** the  $p$ th basis function **do**| Compute  $X_\phi(p, k)$  based on Equation (2.12)**end**Compute  $\hat{X}_{\text{past}}(k)$  based on Equation (2.9)Compute  $\text{HSR}_{\text{ref}} = \text{HSR}$  as a referenceCompute  $P_{\text{ref}} = P_{\text{SL}}$  based on Equation (2.10)**for** each iteration  $m$  **do**| **for** the  $p$ th basis function **do**| | **for** the  $d$ th direction of search **do**| | | Tentatively update  $c_p^{(m)}$  based on Equation (2.7)| | | Compute  $\hat{X}_{\text{new}}(k)$  based on Equation (2.11)

| | | Compute HSR based on Equation (2.8)

| | **end**| | **if** HSR is reduced **then**| | | Find the direction of update  $d$  minimizing HSR| | | Compute  $P_{\text{SL}}$  based on Equation (2.10)| | | **if**  $\eta P_{\text{ref}} < P_{\text{SL}} < P_{\text{ref}}$  **then**| | | | For the optimal direction, update  $c_p^{(m)}$  based on Equation (2.7)| | | | Update the equalizer output  $\hat{\mathbf{x}}$  and  $\hat{X}_{\text{past}}(k)$ | | | | Update  $\text{HSR}_{\text{ref}}$ | | | **end**| | **end**| **end**| **if**  $\mathbf{c}$  has not changed in this iteration **then**| | Reduce the step size  $\delta$ :  $\delta \leftarrow \delta/2$ | **end****end****end****2.3.3 Evaluation of the adaptive nonlinear equalizer**

In this subsection, we investigate the performance of the proposed adaptive nonlinear equalizer in two sets of water tank experiments.

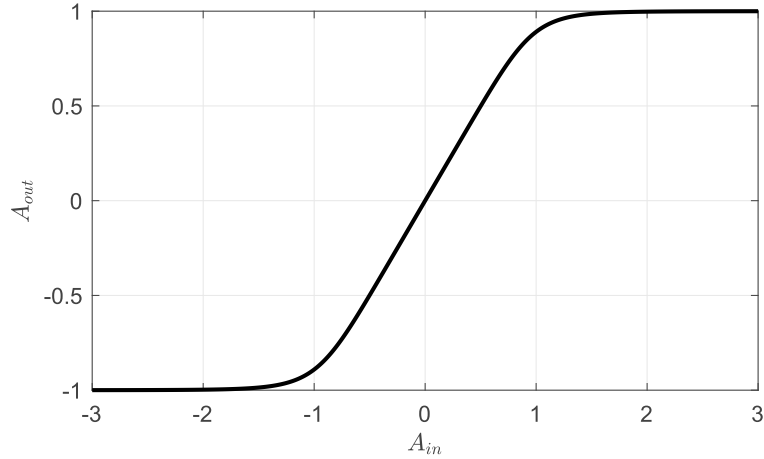


Fig. 2.16 Rapp Model of the nonlinear amplitude response.

### Artificially introduced nonlinearity

We first investigate the performance of the adaptive equalizer for artificially introduced nonlinear distortion in the received signal. The received signal  $\tilde{x}(n)$  is recorded from a hydrophone without pre-amplifier [80] in a water tank experiment.

The experiment is conducted in a 1 m<sup>3</sup> cubic plastic water tank. During the experiment, the projector is placed close to the water surface and the hydrophone is placed close to the bottom. BPSK signals with the root-raised cosine pulse-shaping are transmitted. The parameters of the transmitted signal are set as follows: the roll-off factor is 0.2, the carrier frequency is  $f_c = 12$  kHz, the bandwidth is 1.2 kHz. The sampling rate of the transmitted signal is  $f_s = 96$  kHz and the baseband sampling rate is 1 kHz. Before the transmission, a 5 s silence period is recorded to measure the noise level at the receiver.

The Rapp Model [88] is used as the nonlinear model of the pre-amplifier. The amplitude distortion is given by:

$$\tilde{x}(t) = \frac{x(t)}{\left[|x(t)|^{2\alpha}\right]^{\frac{1}{2\alpha}}}, \quad (2.13)$$

where  $\alpha$  is a parameter which controls the smoothness of the transition region of the response. In Fig. 2.16, we show the amplitude response generated by the Rapp model with  $\alpha = 3$ . The amplitude response can be divided into the linear zone, the transition zone and the saturation zone. We focus on the transition zone since the received signal cannot be equalized once

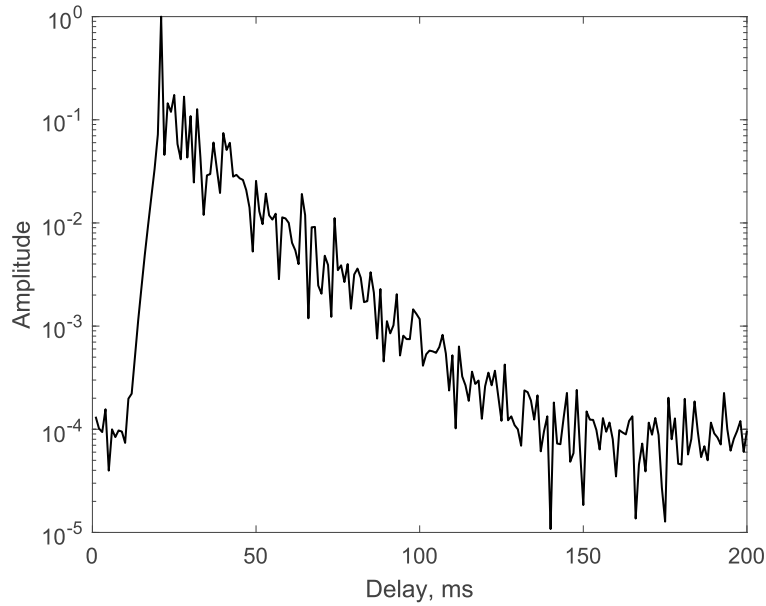


Fig. 2.17 SI channel impulse response in the cubic water tank. A long channel delay spread up to 150 ms can be observed.

it is saturated. The maximum absolute value of the input amplitude is set to 1, so that a substantial part of the signal will be in the transition zone.

The scheme shown in Fig. 2.14 is adopted for the digital SIC. The SRLS adaptive filter [59] is used for the SI channel estimation. The SIC is evaluated by the NMSE performance. The averaged NMSE is computed by averaging the instantaneous NMSE over an 8 s steady-state time interval.

The SI channel in the water tank has a long delay spread of around 150 ms as shown in Fig. 2.17. The NMSE performance of the digital canceller is shown in Fig. 2.18. The filter length is set to  $L = 200$ , and a sliding window length of  $M = 4L = 800$  is used. The SI to noise ratio in this tank experiment is 55 dB. A steady-state NMSE of  $-53$  dB is achieved when we use the original hydrophone output as the desired signal. This NMSE level is used as a benchmark for evaluating the performance of the adaptive equalizer. The steady-state NMSE degrades to  $-46$  dB when the hydrophone output affected by the artificial nonlinearity shown in Fig. 2.16 is used as the desired signal.

We first adapt the equalizer using the MSE-based cost function. The initial step size is set to  $H = 0.1$ . To equalize the nonlinearity which has the amplitude response shown in

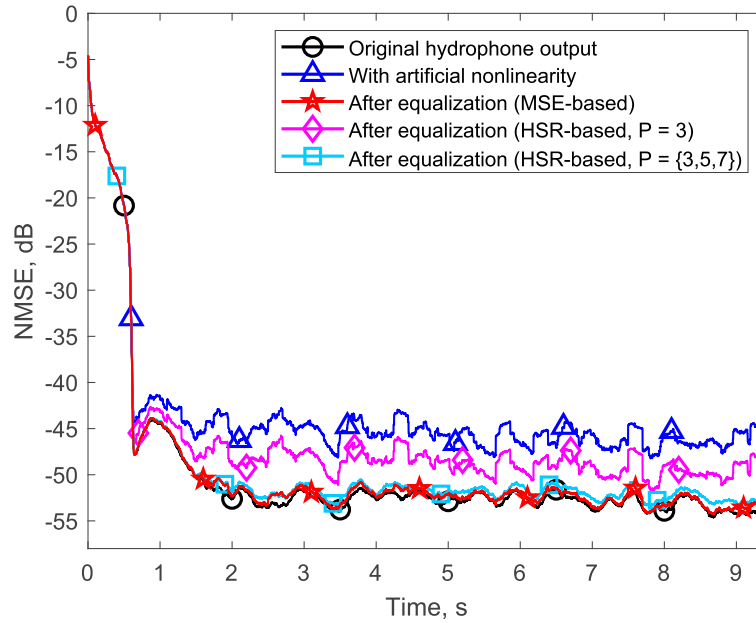


Fig. 2.18 Comparison of the NMSE performance with the simulation data. The simulation data is generated by artificially introducing a nonlinearity to the hydrophone output signal recorded in the tank experiment. The NMSE curves are smoothed by a 200 ms rectangular window.

Fig. 2.16, the Legendre polynomials of odd orders, specifically the third, fifth and seventh-order Legendre polynomials are used. As the MSE-based approach requires the adaptive filtering in each iteration, a small number of iterations  $N_u = 10$  is used to reduce the complexity. Using this approach, the average NMSE is reduced to about  $-53$  dB.

Then, we investigate the performance of the adaptive equalizer which updates the expansion coefficients using the HSR criterion. The signal power spectra before and after introducing the artificial nonlinearity are shown in Fig. 2.19 (a) and (b), respectively. The zoomed spectra around the third harmonic are shown in (d) and (e). It can be seen that the spread of the third harmonic of the original hydrophone output is wider after introducing the nonlinear distortion. Based on our computation, the HSR is increased by 4.1 dB after adding the nonlinear distortion. For equalization, we use the same initial step size as in the MSE-based approach. The number of iterations is  $N_u = 100$ . The power of the sidelobes is computed in the interval  $[f_c - 1.5B, f_c - 0.7B] \cup [f_c + 0.7B, f_c + 1.5B]$ . We use  $\eta = 0.7$  as the threshold of the second constraint.

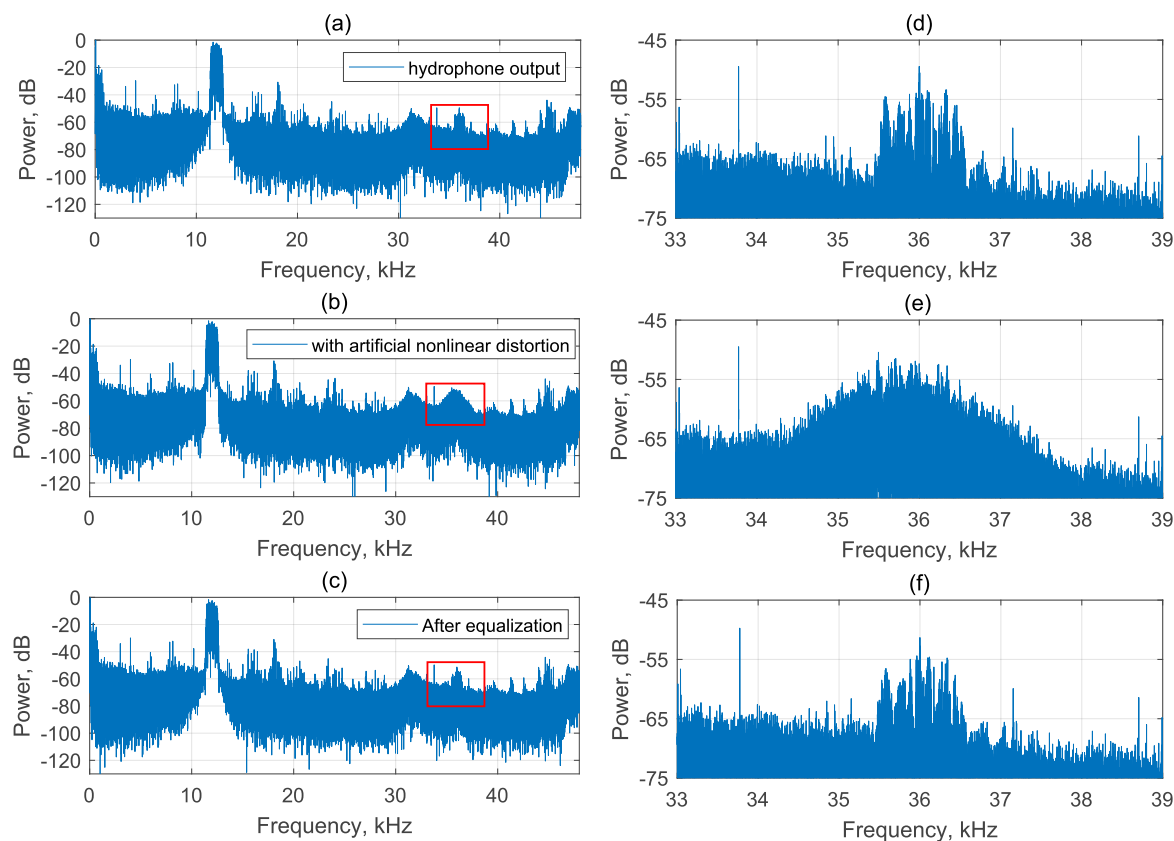


Fig. 2.19 Power spectra of the signals: (a) original hydrophone output; (b) hydrophone output with the artificial nonlinear distortion; (c) nonlinear equalizer output. Zoomed plots of the spectra in (a), (b), (c) are shown in (d), (e), (f), respectively.

As shown in Fig. 2.18, the steady-state NMSE is reduced from  $-46$  dB to about  $-48$  dB when only the third-order Legendre polynomial is used for equalization. The NMSE is further reduced to  $-52$  dB when we include the third, fifth and seventh-order Legendre polynomials. The zoomed power spectrum of the signal after equalization shown in Fig. 2.19 (f) also demonstrates the effectiveness of the nonlinear equalizer as the spectral shape of the third harmonic almost returns to the same shape as that of the original hydrophone output shown in Fig. 2.19 (d). It is seen that both approaches work well in equalizing the artificial nonlinearity added to the received signal.

### Using hydrophone with pre-amplifier

We then evaluate the performance of the proposed nonlinear equalizer with the experimental data recorded from the hydrophone with pre-amplifier [81] in an anechoic water tank. The distance between the projector (Tx) and hydrophone (Rx) is 3 cm as shown in Fig. 2.20. We transmit BPSK signals at  $f_c = 14$  kHz carrier frequency with 1.2 kHz bandwidth. The sampling frequency is  $f_s = 96$  kHz. The SI to noise ratio is around 85 dB.

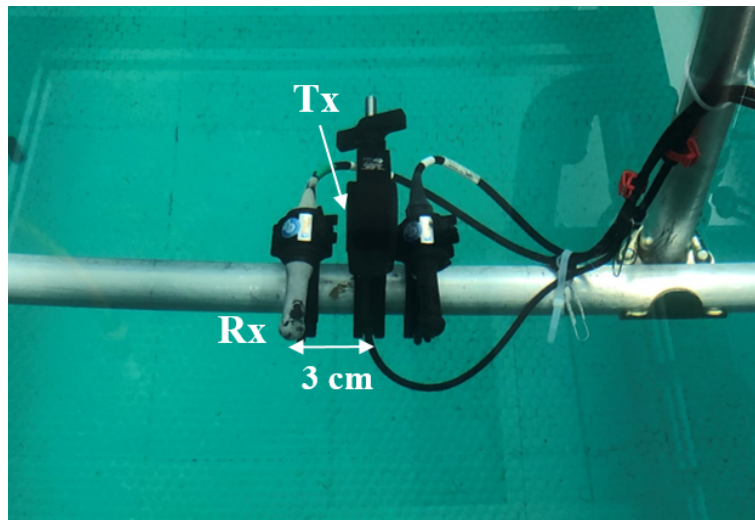


Fig. 2.20 Experimental setup in a 3 m $\times$ 2 m $\times$ 2 m anechoic water tank. The projector and hydrophone are placed at 0.6 m depth.

Unlike the channel impulse response shown in Fig. 2.17, the SI channel in the anechoic water tank only contains the direct path and the first surface reflection. The other reflections are absorbed by the tank walls. The SRLS adaptive filter is used for the SI channel estimation. We use the filter length  $L = 50$  and a sliding window length of  $M = 500$ . When the original hydrophone output is used for SIC, an average NMSE level of  $-69$  dB is achieved.

Then we apply the MSE-based adaptive equalizer with the third Legendre polynomial. For this experiment, the improvement achieved by including higher order polynomials is minor, thus we only use one basis function to reduce the complexity. The initial step size is  $H = 0.01$ , and the number of updates is  $N_u = 10$ . It can be seen in Fig. 2.21 that the average NMSE is reduced to  $-73$  dB. An improvement of about 4 dB in the NMSE performance is achieved.

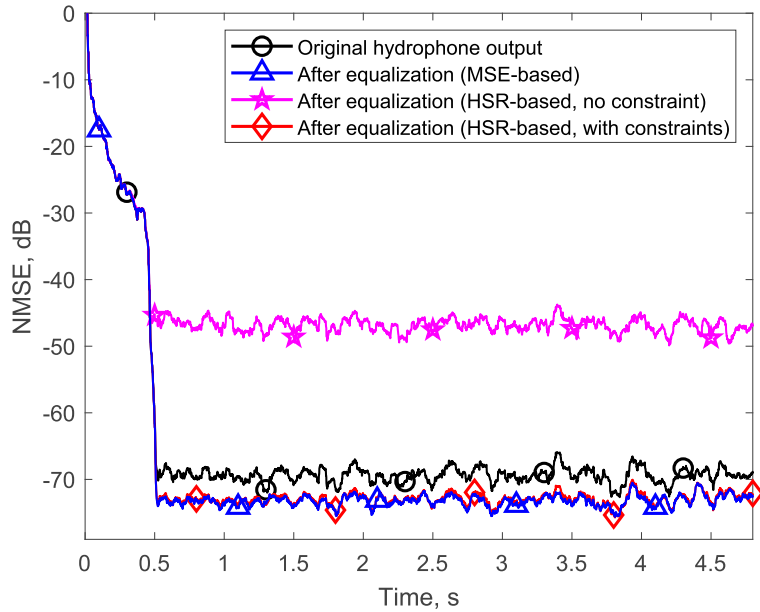


Fig. 2.21 Comparison of the NMSE performance in the anechoic water tank. The NMSE curves are smoothed by a rectangular window of length 50 ms.

For the HSR-based equalizer, we also use the third-order Legendre polynomial as the basis function and with the same step size. The number of updates is  $N_u = 20$ . In Fig. 2.22, we show the power spectra of the PA output, the hydrophone output and the equalized signals under different conditions. Zoomed plots of the spectra are also shown to provide a clear visualisation for the comparison. It can be seen in Fig. 2.22 (g) that the sidelobes of the signal are significantly increased when the HSR with no constraint is used, which results in a poor NMSE performance as shown in Fig. 2.21.

The NMSE performance is around  $-68$  dB without the second constraint. This is due to the over-equalization of the nonlinearity in the hydrophone output. There should be a threshold which defines the maximum reduction in the sidelobe level. In this scenario, we use  $\eta = 0.97$ . In practice, the threshold can be tuned based on the signal spectrum and the MSE performance. The complexity of the equalizer is significantly lower when using the HSR-based cost function, since there is no need for the adaptive filtering providing the highest contribution into the algorithm complexity. After applying both constraints to the cost function, an NMSE of  $-73$  dB is achieved, which is the same as the NMSE performance of the MSE-based equalization.

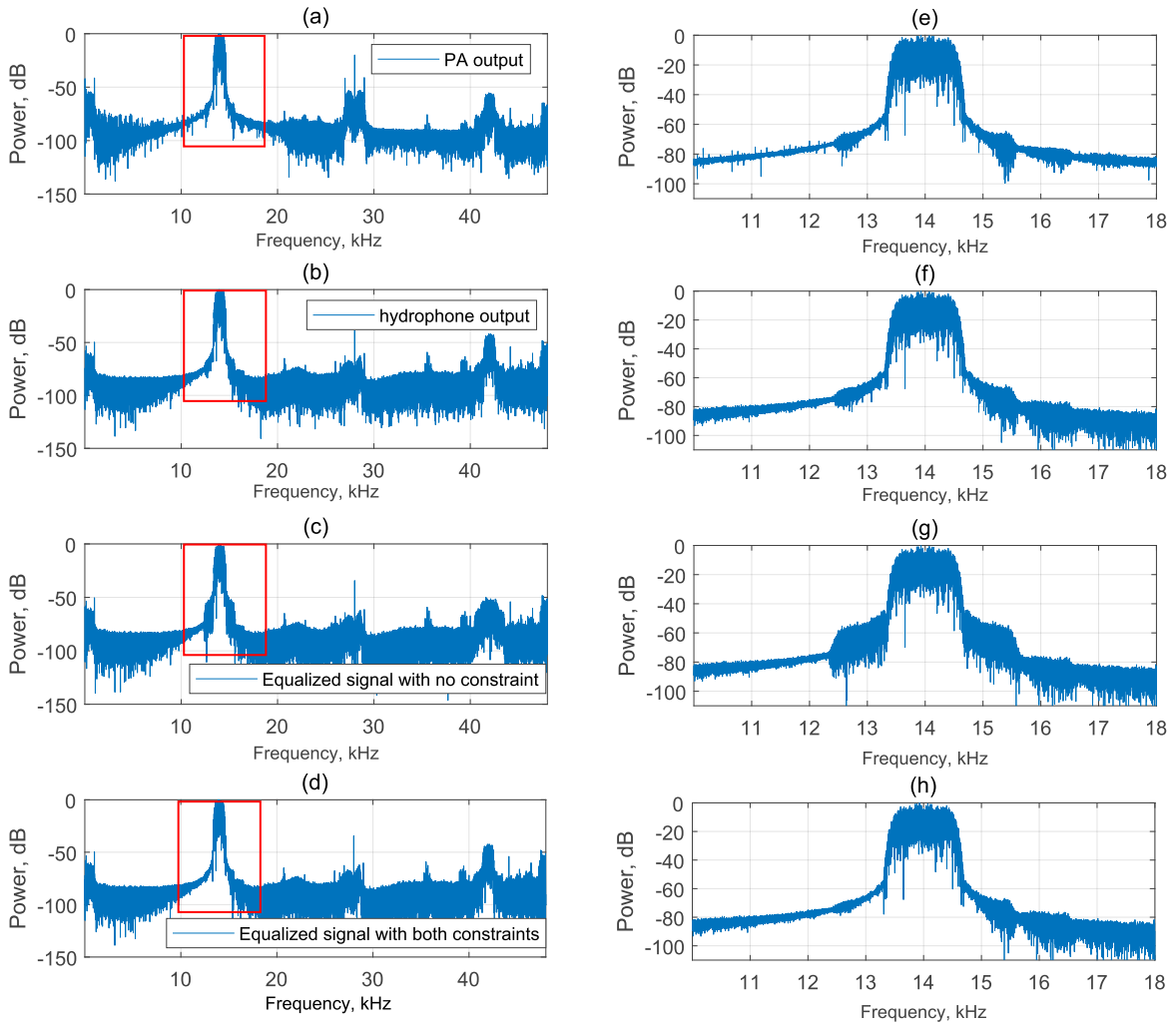


Fig. 2.22 (a) PA output; (b) Original hydrophone output; (c) Signal equalized using HSR as the cost function; (d) Signal equalized using HSR with both constraints. Zoomed plots of the spectra in (a), (b), (c) and (d) are shown in (e), (f), (g) and (h), respectively.

## 2.4 Conclusions

This chapter discusses the main factors affecting the digital cancellation performance in FD UWA systems and propose the general structure of the digital SI canceller which takes into account the PA nonlinearity, the sampling time of the baseband to passband conversion and the nonlinearity introduced by the hydrophone pre-amplifier.

The digital canceller structure presented in Section 2.1 uses the PA output as the reference signal for digital cancellation to include the nonlinear distortions introduced by the PA. In

such a case, a linear adaptive filter is sufficient for SI channel estimation. As demonstrated by the tank experimental results, the digital cancellation performance can be significantly improved by using the PA output as the reference signal compared to the case of using the digital data as the reference signal.

As illustrated in Section 2.1, the adaptive filter used for digital cancellation works in the baseband. This leads to another issue that affects the cancellation performance, the sampling time of the baseband to passband conversion. In Section 2.2, an extended structure of the digital SI canceller with multi-branch combining scheme has been proposed to deal with the sensitivity of the SIC performance to the sampling time. As evaluated by the tank and lake experiments, the extended structure is capable of providing effective SIC regardless of the sampling time.

In Section 2.3, we have proposed a technique for equalizing the nonlinear distortion of signals introduced by the hydrophone pre-amplifier in FD UWA systems. The Legendre polynomials are used as basis functions for the adaptive nonlinear equalization. The expansion coefficients of the basis functions are updated recursively to reduce the cost function. We have considered two cost functions, one is the MSE and the other is derived based on the signal power spectrum to reduce the computational complexity. The performance of the nonlinear equalizer is evaluated in two water tank experiments with BPSK signals. Note that this technique can also be applied to other communication signals such as OFDM. An improvement in the SIC performance has been observed with both experiments when applying the nonlinear equalizer.

## Chapter 3

# Time-Varying Self-Interference Channel Estimation

SI channel estimation is vital for digital cancellation in FD UWA systems. In this chapter, we investigate the SIC performance of the adaptive filters in time-varying SI channels with the digital canceller structure proposed in Chapter 2. In Section 3.2, a new evaluation metric is proposed for measuring the SIC performance. In Section 3.3, a new interpolating adaptive filter (SRLS-P) based on the SRLS algorithm is proposed, which uses parabolic interpolation for estimating the time-varying channels. The applicability of the new evaluation metric is investigated in Section 3.4. Simulation results for the adaptive filters in baseband and passband scenarios are presented in Section 3.4 and Section 3.5, respectively. Section 3.6 compares the SIC performance provided by the adaptive filters using experimental data. In Section 3.7, we draw the conclusions.

The work in this chapter is presented in the paper: L. Shen, Y. Zakharov, B. Henson, N. Morozs, and P. Mitchell, “Adaptive filtering for full-duplex UWA systems with time-varying self-interference channel,” *IEEE Access*, vol. 8, pp. 187 590–187 604, 2020.

### 3.1 Introduction

Classical adaptive filters can efficiently cancel the strong SI in a time-invariant environment with the digital SI canceller structure presented in Chapter 2. However, in practice, the SI channel can be fast time-varying [21], especially when the transmit and receive antennas are positioned close to the sea/lake surface [63, 69, 89]. The main limitation is the tracking ability of the classical adaptive filters. The Kalman filter is considered as a good candidate for estimation of time-varying channels [59, 90]. However, for using the Kalman filter, the channel statistics should be known, which is often not the case in practice. To improve SIC performance in fast time-varying channels, other schemes are required.

In time-varying channels, the SIC performance can be significantly improved if the input signals are delayed with respect to the time-varying estimate of the channel response as shown in Fig. 3.1. However, to our knowledge, this opportunity for FD systems has not been investigated yet.

Introducing a delay between the channel estimate and the inputs to the adaptive filter results in a problem in measuring the cancellation performance. The residual SI power is normally used to characterise the FD system performance [21, 38, 41], which can be measured by the MSE [48]. However, the MSE in an adaptive filter with a delay is unsuitable for this purpose, since, in this case, unlike the classical RLS algorithms, the same data is used for channel estimation and computation of the MSE, resulting in over-fitting. Therefore, another measurement of SIC performance is required when using adaptive filters with a delay.

### 3.2 Evaluation of SIC performance

The MSE and the mean squared deviation (MSD) are normally used for evaluating the channel estimation performance. In subsection 3.2.1, we discuss if it is practical to use these two metrics to evaluate the SIC performance in FD systems. In subsection 3.2.2, a new metric, the SICF, is proposed for evaluation of the SIC performance.

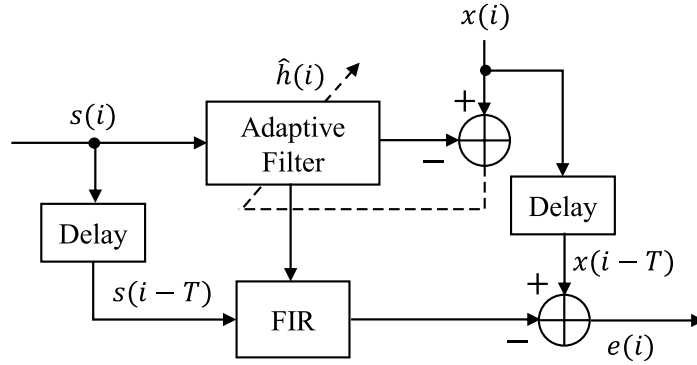


Fig. 3.1 Adaptive filter with a delay.

### 3.2.1 MSE and MSD performance

Consider the SIC scheme shown in Fig. 3.1. In this scheme,  $x(i)$  is a baseband version of the signal received by the hydrophone, and it is modelled as:

$$x(i) = \mathbf{h}^H(i)\mathbf{s}(i) + z(i), \quad (3.1)$$

where  $\mathbf{h}(i)$  is the baseband SI channel response at time instant  $i$ ,  $s(i)$  is the baseband version of the PA output signal,  $\mathbf{s}(i) = [s(i), \dots, s(i-L+1)]^T$ , and  $L$  is the channel length. The signal  $z(i)$  contains the far-end signal, as well as noise signals such as the ambient noise, ADC noise, etc. In terms of an adaptive filter operating in the identification mode,  $s(i)$  is the regressor and  $x(i)$  is the desired signal [59, 90]. Using these signals, the adaptive filter produces an estimate  $\hat{\mathbf{h}}(i+T)$  of  $\mathbf{h}(i)$ . Note that, in classical adaptive filters,  $T = 0$  and it is assumed that the estimate  $\hat{\mathbf{h}}(i)$  is obtained using the regressor and desired signal up to time instant  $i-1$ . In this case, the FIR filter shown in Fig. 3.1 is not required since it is the same as the FIR filter within the adaptive filter with the same input. However, if  $T > 0$ , the regressors of these FIR filters are different, they are  $\mathbf{s}(i)$  for the adaptive filter and the delayed regressor  $\mathbf{s}(i-T)$  for the FIR filter. Based on this channel estimate, the SI is cancelled by recovering the SI signal as  $\hat{\mathbf{h}}^H(i)\mathbf{s}(i-T)$  and subtracting it from the received signal:

$$e(i) = x(i-T) - \hat{\mathbf{h}}^H(i)\mathbf{s}(i-T). \quad (3.2)$$

The performance of an adaptive filter is most often evaluated using the MSE [59, 90]. The MSE is defined as:

$$\text{MSE}(i) = \text{E}\{|e(i)|^2\}, \quad (3.3)$$

where  $\text{E}\{\cdot\}$  denotes the expectation.

For a classical adaptive filter (with  $T = 0$ ), the SIC performance can be evaluated by computing the MSE. However, by adjusting parameters of an adaptive filter with a delay (non-causal adaptive filter), it is possible to make the MSE even lower than the ‘noise-plus-far-end-signal’ floor, although this does not mean that the SIC performance is good. It means that not only the SI is cancelled, but also a part of the far-end signal (i.e., the signal of interest) is also cancelled. Essentially, the adaptive filter is over-fitted, since, due to the delay, the same data is used for training the adaptive filter and for the MSE computation. In these scenarios, the MSE becomes an unreliable metric for assessment of the SIC performance.

From the interference cancellation point of view, the SIC performance can be evaluated by how much the near-end SI is cancelled. Therefore, everything apart from the near-end SI is treated as the signal of interest (including far-end signal and the noise), which should be recovered. The signal to interference ratio (SIR) at the SI canceller can be written as:

$$\text{SIR}(i) = \frac{\sigma_z^2}{\text{E}\{|\varepsilon(i)|^2\}}, \quad (3.4)$$

where  $\sigma_z^2 = \text{E}\{|z(i)|^2\}$ ,  $z(i)$  is the signal of interest that includes the far-end signal and the noise, and  $\varepsilon(i)$  is the residual interference.

If the far-end signal and the error signal are not correlated, then the residual interference  $\varepsilon(i)$  can be represented as:

$$\varepsilon(i) = e(i) - z(i - T), \quad (3.5)$$

and substituting (3.1) and (3.2) into (3.5), we have:

$$\varepsilon(i) = [\mathbf{h}(i - T) - \hat{\mathbf{h}}(i)]^H \mathbf{s}(i - T). \quad (3.6)$$

Assuming that  $s(i)$  are uncorrelated for different  $i$  and uncorrelated to  $\hat{\mathbf{h}}(i)$ , we have:

$$\mathbb{E}\{\mathbf{s}(i-T)\mathbf{s}^H(i-T)\} = \sigma_s^2 \mathbf{I}_L, \quad (3.7)$$

where  $\sigma_s^2 = \mathbb{E}\{|s(i)|^2\}$  is the variance of the signal  $s(i)$ , which is assumed stationary. Then using (3.6) and (3.7), we obtain:

$$\mathbb{E}\{|\varepsilon(i)|^2\} = \sigma_s^2 \mathbb{E}\{\|\mathbf{h}(i-T) - \hat{\mathbf{h}}(i)\|_2^2\} \quad (3.8)$$

$$= \sigma_s^2 \text{MSD}(i-T), \quad (3.9)$$

where the MSD is defined as:

$$\text{MSD}(i) = \mathbb{E}\{\|\mathbf{h}(i) - \hat{\mathbf{h}}(i+T)\|_2^2\}. \quad (3.10)$$

Finally, we obtain:

$$\text{SIR}(i) = \frac{\sigma_z^2}{\sigma_s^2} \cdot \frac{1}{\text{MSD}(i-T)}. \quad (3.11)$$

Thus, the MSD is a useful characteristic of an adaptive filter operating within an SI canceller. It shows how much the ratio between powers of the signal of interest (including noise) and near-end interference improves due to the accuracy of the near-end channel estimation. However, the MSD computation requires knowledge of the true channel response  $\mathbf{h}(i)$ , which is unavailable in most practical scenarios. Another important issue is that (3.11) is only applicable if  $\hat{\mathbf{h}}(i)$  and  $s(i)$  are uncorrelated, which may not be the case for adaptive filters with delay.

### 3.2.2 SIC Factor

In [21, 38, 41, 51], the interference cancellation gain, which is defined as the ratio of the near-end SI power to the residual SI power, is used for evaluating the performance of the SI canceller. Note that the residual SI is computed as in (3.5) assuming that the far-end signal is not correlated with the error signal. This assumption is no longer valid when adaptive

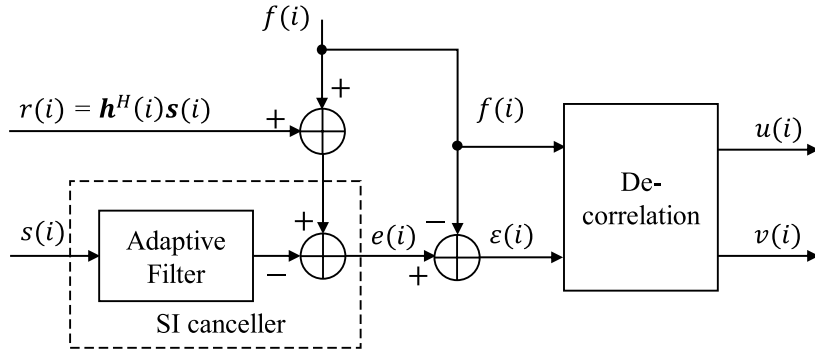


Fig. 3.2 Block diagram of FD system with SIC;  $r(i)$  is the baseband received SI,  $s(i)$  is the regressor (baseband PA output),  $f(i)$  is the artificially added far-end signal,  $e(i)$  is the error signal at the adaptive filter output and  $\varepsilon(i)$  is the residual signal that might be correlated with  $f(i)$ ;  $u(i)$  and  $v(i)$  are the modified (uncorrelated) signal of interest and residual interference, respectively.

filters with delay are used. We now propose the SICF, which is shown to provide a good indication of the cancellation performance. It does not require the knowledge of the true channel response, and can be used in practice for adaptive filters with and without the delay. This SICF can be used to evaluate the SIC performance without the need of implementing a whole FD system.

Here we consider the SIC problem from the far-end signal detection point of view. The higher far-end signal to residual interference ratio at the SI canceller output, the better the SIC performance. In this scenario, the far-end signal is the signal of interest, and everything else is treated as interference (including noise). Since the far-end signal level is typically higher than the receiver's noise floor, the noise is ignored in the derivation below to simplify the expression. Although the noise is ignored in our derivation, the metric SICF is applicable in the case when the noise is present; this can be seen in numerical results presented in Section 3.4.

Fig. 3.2 illustrates our description below. We artificially add to the SI signal  $r(i)$  a known signal  $f(i)$  assumed to be a far-end signal. The level of the signal  $\sigma_f^2 = E\{|f(i)|^2\}$  is chosen to guarantee a predefined input SIR:

$$\text{SIR}_{\text{in}}(i) = \frac{\sigma_f^2}{E\{|r(i)|^2\}}. \quad (3.12)$$

The SI canceller (shown in Fig. 3.2) subtracts the SI estimate produced by the adaptive filter from the received signal  $r(i) + f(i)$ . The canceller output  $e(i)$  contains the signal of interest  $f(i)$  and a residual signal  $\varepsilon(i)$ :

$$e(i) = f(i) + \varepsilon(i), \quad (3.13)$$

and since both signals  $e(i)$  and  $f(i)$  are available after the cancellation, the residual signal  $\varepsilon(i)$  can be computed as  $\varepsilon(i) = e(i) - f(i)$ .

Here we measure the SIC performance as a factor of improvement in the SIR ratio due to the SIC and compute the SICF as:

$$\text{SICF}(i) = \frac{\text{SIR}_{\text{out}}(i)}{\text{SIR}_{\text{in}}(i)}. \quad (3.14)$$

By introducing the artificially added far-end signal, the SICF that we propose evaluates the SI canceller performance taking into account the loss of the far-end signal after SIC.

For classical adaptive filters without delay, the signal of interest  $f(i)$  and the residual  $\varepsilon(i)$  are uncorrelated, thus  $\text{SIR}_{\text{out}}(i)$  can be computed as a ratio of their variances. For adaptive filters with delay, due to the over-fitting in the adaptive filter, in general, these two signals are correlated. Therefore, in this case, we cannot use their ratio for computing  $\text{SIR}_{\text{out}}(i)$ , another approach is required.

We now assume that the signal of interest  $f(i)$  is attenuated due to the imperfection of the adaptive filter. More specifically, we rewrite (3.13) as:

$$e(i) = \alpha f(i) + [(1 - \alpha)f(i) + \varepsilon(i)] \quad (3.15)$$

$$= u(i) + v(i), \quad (3.16)$$

where the modified signal of interest  $u(i) = \alpha f(i)$  and the modified residual interference component  $v(i) = (1 - \alpha)f(i) + \varepsilon(i)$  are uncorrelated.

We now find the coefficient  $\alpha$  that zeroes the correlation between  $u(i)$  and  $v(i)$ :

$$\text{E}\{u(i)v^*(i)\} = \text{E}\{\alpha f(i)[(1 - \alpha)f(i) + \varepsilon(i)]^*\} = 0. \quad (3.17)$$

From (3.17), we find  $\alpha$  as:

$$\alpha = 1 + \frac{1}{\sigma_f^2} \mathbb{E}\{f^*(i)\varepsilon(i)\}. \quad (3.18)$$

After finding  $\alpha$ , the modified signal of interest  $u(i)$  and residual interference  $v(i)$  can be computed from (3.15), and the ratio of their variances can now be used for computation of  $\text{SIR}_{\text{out}}(i)$ .

In experiments, the mathematical expectation in (3.18) is replaced by the average over a time interval after convergence of the adaptive filter. The output SIR can be computed as:

$$\text{SIR}_{\text{out}} = \frac{\|\mathbf{u}\|_2^2}{\|\mathbf{v}\|_2^2}, \quad (3.19)$$

where  $\mathbf{u} = [u(0), \dots, u(N_c - 1)]^T$  is a  $N_c \times 1$  vector of the signal of interest,  $\mathbf{v} = [v(0), \dots, v(N_c - 1)]^T$ , and  $N_c$  is the averaging interval. The averaging interval  $N_c$  is preferred to be longer than the coherence time of the SI channel.

Note that the far-end signal we used to compute the SICF is artificially added to the received signal, thus it is known and later is removed. The SICF is intended to be used for adjusting the parameters of the adaptive filters to ensure the optimal SIC performance. In practical systems, the SICF can still be computed with an artificial far-end signal for parameter tuning at the training stage without far-end transmission.

### 3.3 Proposed SRLS-P adaptive filter

In this section, we review the ERLS and SRLS adaptive filters, consider their delayed versions, and propose a new adaptive filter based on the SRLS algorithm and parabolic approximation of channel variation in time; we call it the SRLS-P adaptive filter.

### 3.3.1 Classical ERLS and SRLS adaptive filters

At every time instant  $i$ , an RLS adaptive filter updates the solution vector  $\hat{\mathbf{h}}(i)$  according to the normal equation:

$$\mathbf{R}(i)\mathbf{h}(i) = \boldsymbol{\beta}(i), \quad (3.20)$$

where  $\mathbf{R}(i)$  is an  $L \times L$  autocorrelation matrix,  $\boldsymbol{\beta}(i)$  is an  $L \times 1$  cross-correlation vector, and  $L$  is the filter length. The autocorrelation matrix and cross-correlation vector are approximated by averaging in time.

For the classical ERLS adaptive filter,  $\mathbf{R}(i)$  and  $\boldsymbol{\beta}(i)$  can be updated as:

$$\mathbf{R}(i) = (\lambda - 1)\mathbf{R}(i - 1) + \mathbf{s}(i)\mathbf{s}^H(i), \quad (3.21)$$

$$\boldsymbol{\beta}(i) = (\lambda - 1)\boldsymbol{\beta}(i - 1) + x^*(i)\mathbf{s}(i), \quad (3.22)$$

where  $\lambda$  is the forgetting factor,  $\mathbf{s}(i) = [s(i), s(i - 1), \dots, s(i - L + 1)]^T$  is the regressor at the  $i$ th time instant, and  $x(i)$  is the  $i$ th sample of the desired signal. The weights of the time average window is the exponential  $\lambda^{|i-p|}$ ,  $p \leq i$ .

For the classical SRLS adaptive filter, the update of  $\mathbf{R}(i)$  and  $\boldsymbol{\beta}(i)$  can be written as [86, 91]:

$$\mathbf{R}(i) = \mathbf{R}(i - 1) + \mathbf{s}(i)\mathbf{s}^H(i) - \mathbf{s}(i - M)\mathbf{s}^H(i - M), \quad (3.23)$$

$$\boldsymbol{\beta}(i) = \boldsymbol{\beta}(i - 1) + x^*(i)\mathbf{s}(i) - x^*(i - M)\mathbf{s}(i - M), \quad (3.24)$$

where  $M$  is the sliding window length. The time average window is a constant over the time interval  $[i - M + 1, i]$ , and zero otherwise. Fig. 3.3 shows the position of the time window in the SRLS algorithm with respect to the time varying channel response  $\mathbf{h}(i)$ .

### 3.3.2 Delayed ERLS and SRLS adaptive filters

Since  $\mathbf{R}(i)$  and  $\boldsymbol{\beta}(i)$  are obtained by averaging in time, the current channel estimate  $\hat{\mathbf{h}}(i)$  can be seen as an average of the true channel response over past time instants. If the SI channel is

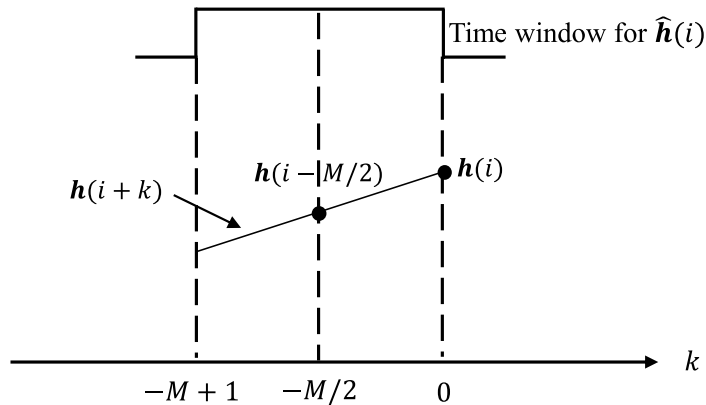


Fig. 3.3 Time-varying channel and time windows of the SRLSd algorithm.

time-invariant,  $\hat{\mathbf{h}}(i)$  can be an accurate estimate of  $\mathbf{h}(i)$ . However, for a time-varying channel, the channel estimate  $\hat{\mathbf{h}}(i)$  cannot accurately represent the true channel impulse response  $\mathbf{h}(i)$ .

For the SRLS adaptive filter, the channel estimate  $\hat{\mathbf{h}}(i)$  can be seen as an average of  $\mathbf{h}(i)$  over the past  $M$  time instants. As shown in Fig. 3.3, if we assume that the channel response varies linearly in the vicinity of  $i$ , then its average over the rectangular window is equal to  $\mathbf{h}(i - M/2)$ . In such a case,  $\hat{\mathbf{h}}(i)$  is a more accurate estimate of  $\mathbf{h}(i - M/2)$  than  $\mathbf{h}(i)$ . Therefore, using the delay  $T = M/2$  in the scheme shown in Fig. 3.1 should provide an improvement in the SIC performance compared to the case when  $T = 0$ . In Section 3.4, we demonstrate that this is indeed the case. For the ERLS adaptive filter, the time window is infinite in length, and it is more difficult to determine the optimal delay which provides the highest level of cancellation. Moreover, in Section 3.4, we also show that even for the same forgetting factor  $\lambda$ , different channel realisations require different  $T$ . Therefore, our proposed adaptive filter is based on the SRLS algorithm, for which the optimal delay is well defined. We call the ERLS and SRLS algorithms with delays as ERLSd and SRLSd, respectively, to distinguish them from the classical RLS algorithms.

### 3.3.3 SRLS-P adaptive filter

Compared to the SRLS algorithm, the SRLSd adaptive filter improves the MSD performance, and, as a result, it improves the SIC performance by applying the current channel estimate

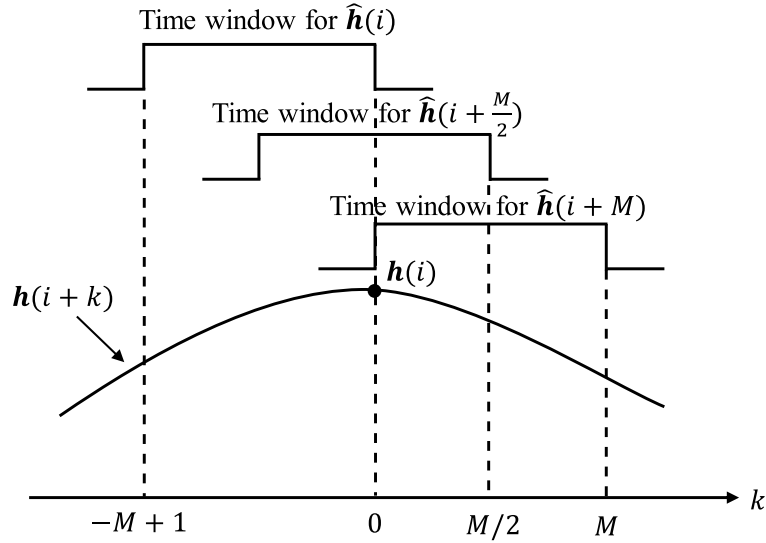


Fig. 3.4 Time-varying channel and time windows of the SRLS-P algorithm.

found at the  $i$ th time instant to the delayed regressor  $s(i - M/2)$ , corresponding to the middle of the averaging time window of length  $M$ . It changes the way the SI signal is reconstructed, but the channel estimates are computed in the same way as in the classical SRLS adaptive filter.

In fast time-varying channels, the channel estimation performance provided by the SRLSd algorithm is still limited, since the channel estimate can be viewed as simply an average of the true channel response over  $M/2$  past and  $M/2$  future samples. To improve the tracking ability in fast time-varying channels, we propose the SRLS-P adaptive filter. The key idea of the algorithm is the parabolic interpolation of the channel time variation using the estimates  $\hat{\mathbf{h}}(i)$  provided by the SRLS algorithm.

We assume that the time-varying channel response fits a second-order algebraic polynomial within a short time interval around the time instant  $i$ , as shown in Fig. 3.4:

$$\mathbf{h}(i+k) = \mathbf{h}_0(i) + \mathbf{h}_1(i)k + \mathbf{h}_2(i)k^2, \quad (3.25)$$

where  $k = -M + 1, \dots, M$ , and  $\mathbf{h}_0(i)$ ,  $\mathbf{h}_1(i)$  and  $\mathbf{h}_2(i)$  are three  $L \times 1$  vectors to be estimated. From (3.25), it can be seen that  $\mathbf{h}(i) = \mathbf{h}_0(i)$ , and thus an estimate of  $\mathbf{h}_0(i)$  can be used as an estimate of the channel response  $\mathbf{h}(i)$  at time instant  $i$ .

The channel estimate  $\hat{\mathbf{h}}(i+k)$  computed by the SRLS algorithm in scenarios without noise can be expressed as (see Appendix B):

$$\hat{\mathbf{h}}(i+k) = \frac{1}{M} \mathbf{R}^{-1}(i+k) \sum_{m=-M+k+1}^k \mathbf{R}_{i+m} \mathbf{h}(i+m), \quad (3.26)$$

where  $\mathbf{R}(i) = \mathbf{S}^H(i)\mathbf{S}(i)$  is the  $L \times L$  auto-correlation matrix of the regressor,  $\mathbf{S}(i) = [\mathbf{s}(i), \mathbf{s}(i-1), \dots, \mathbf{s}(i-M+1)]^T$  is an  $M \times L$  observation matrix,  $\mathbf{s}(i)$  is the regressor at the  $i$ th time instant and  $\mathbf{R}_{i+m} = \mathbf{s}(i+m)\mathbf{s}^H(i+m)$ .

By substituting (3.25) into (3.26) for  $k=0$ ,  $k=M/2$ , and  $k=M$ , we obtain a system of equations with respect to the unknown  $3L \times 1$  vector  $\mathbf{z} = [\mathbf{h}_0(i); \mathbf{h}_1(i); \mathbf{h}_2(i)]$ . By solving the system, we obtain an estimate  $\hat{\mathbf{h}}_0(i)$  of  $\mathbf{h}_0(i)$ , which is also the new channel estimate  $\tilde{\mathbf{h}}(i)$  of  $\mathbf{h}(i)$ .

More specifically, we have:

$$\begin{aligned} \hat{\mathbf{h}}(i) &= \frac{1}{M} \mathbf{R}^{-1}(i) \\ &\times \sum_{m=-M+1}^0 \mathbf{R}_{i+m} [\mathbf{h}_0(i) + m\mathbf{h}_1(i) + m^2\mathbf{h}_2(i)] \\ &= \mathbf{h}_0(i) + \mathbf{A}_1 \mathbf{h}_1(i) + \mathbf{A}_2 \mathbf{h}_2(i), \end{aligned} \quad (3.27)$$

where

$$\mathbf{A}_1 = \mathbf{R}^{-1}(i) \sum_{m=-M+1}^0 m \mathbf{R}_{i+m}, \quad (3.28)$$

$$\mathbf{A}_2 = \mathbf{R}^{-1}(i) \sum_{m=-M+1}^0 m^2 \mathbf{R}_{i+m}. \quad (3.29)$$

Similarly, we obtain:

$$\hat{\mathbf{h}}(i + M/2) = \mathbf{h}_0(i) + \mathbf{B}_1 \mathbf{h}_1(i) + \mathbf{B}_2 \mathbf{h}_2(i), \quad (3.30)$$

$$\hat{\mathbf{h}}(i + M) = \mathbf{h}_0(i) + \mathbf{C}_1 \mathbf{h}_1(i) + \mathbf{C}_2 \mathbf{h}_2(i), \quad (3.31)$$

where

$$\mathbf{B}_1 = \mathbf{R}^{-1}(i + M/2) \sum_{m=-M/2+1}^{M/2} m \mathbf{R}_{i+m}, \quad (3.32)$$

$$\mathbf{B}_2 = \mathbf{R}^{-1}(i + M/2) \sum_{m=-M/2+1}^{M/2} m^2 \mathbf{R}_{i+m}, \quad (3.33)$$

and

$$\mathbf{C}_1 = \mathbf{R}^{-1}(i + M) \sum_{m=1}^M m \mathbf{R}_{i+m}, \quad (3.34)$$

$$\mathbf{C}_2 = \mathbf{R}^{-1}(i + M) \sum_{m=1}^M m^2 \mathbf{R}_{i+m}. \quad (3.35)$$

We now arrive at the system of equations:

$$\begin{cases} \mathbf{h}_0(i) + \mathbf{A}_1 \mathbf{h}_1(i) + \mathbf{A}_2 \mathbf{h}_2(i) = \hat{\mathbf{h}}(i), & (3.36) \\ \mathbf{h}_0(i) + \mathbf{B}_1 \mathbf{h}_1(i) + \mathbf{B}_2 \mathbf{h}_2(i) = \hat{\mathbf{h}}(i + M/2), & (3.37) \\ \mathbf{h}_0(i) + \mathbf{C}_1 \mathbf{h}_1(i) + \mathbf{C}_2 \mathbf{h}_2(i) = \hat{\mathbf{h}}(i + M), & (3.38) \end{cases}$$

or, in a compact form,

$$\mathbf{Dz} = \hat{\mathbf{h}}, \quad (3.39)$$

where  $\hat{\mathbf{h}} = [\hat{\mathbf{h}}(i); \hat{\mathbf{h}}(i + M/2); \hat{\mathbf{h}}(i + M)]$  and

$$\mathbf{D} = \begin{bmatrix} \mathbf{I}_L & \mathbf{A}_1 & \mathbf{A}_2 \\ \mathbf{I}_L & \mathbf{B}_1 & \mathbf{B}_2 \\ \mathbf{I}_L & \mathbf{C}_1 & \mathbf{C}_2 \end{bmatrix}. \quad (3.40)$$

**Algorithm 3** SRLS-P algorithm**Input:**  $\mathbf{s}, \mathbf{x}, L, M, \epsilon$ **Output:**  $\tilde{\mathbf{h}}$ Initialization:  $\hat{\mathbf{h}}(0) = \mathbf{0}, \mathbf{R}(i) = \mathbf{0}$  for  $i \leq 0$ **for** every sample  $i$  **do**    Update  $\mathbf{S}(i)$  and  $\mathbf{x}(i)$      $\mathbf{R}(i) = \mathbf{S}^H(i)\mathbf{S}(i) + \epsilon\mathbf{I}_L$      $\boldsymbol{\beta}(i) = \mathbf{S}^H(i)\mathbf{x}(i)$      $\hat{\mathbf{h}}(i) = \mathbf{R}^{-1}(i)\boldsymbol{\beta}(i)$     Compute  $\mathbf{A}_1, \mathbf{A}_2, \mathbf{B}_1, \mathbf{B}_2, \mathbf{C}_1, \mathbf{C}_2$  as in (3.28), (3.29), and (3.32)-(3.35)    Generate the matrix  $\mathbf{D}$  as in (3.40) and vector  $\hat{\mathbf{h}} = [\hat{\mathbf{h}}(i); \hat{\mathbf{h}}(i + M/2); \hat{\mathbf{h}}(i + M)]^T$     Solve the system of equations  $\mathbf{D}\mathbf{z} = \hat{\mathbf{h}}$      $\tilde{\mathbf{h}}(i) = \hat{\mathbf{h}}_0(i) = [\mathbf{z}]_{1,\dots,L}$ **end**

After solving the system in (3.39), the estimate of the impulse response is found as the first  $L$  elements in the vector  $\mathbf{z}$ :

$$\tilde{\mathbf{h}}(i) = \hat{\mathbf{h}}_0(i) = [\mathbf{z}]_{1,\dots,L}. \quad (3.41)$$

The SRLS-P adaptive algorithm is summarized in Algorithm 3, where  $\epsilon$  is a regularization parameter,  $\mathbf{s}$  is the PA output,  $\mathbf{x}$  is the received signal,  $\mathbf{I}_L$  is an  $L \times L$  identity matrix,  $\mathbf{x}(i) = [x(i), x(i-1), \dots, x(i-M+1)]^T$  is an  $M \times 1$  desired signal vector at the  $i$ th time instant.

The complexity of the SRLS-P algorithm will be dominated by the complexity of solving the system of equations in (3.39). Directly solving the system of equation requires an order of  $L^3$  arithmetic operations. The complexity can be reduced by solving the system of equation recursively based on the solution obtained at the previous time instant using the DCD algorithm [86]. In such a case, the complexity reduces to an order of  $N_u L$  operations, where  $N_u$  is the number of DCD updates, which is typically a small number.

### 3.4 Baseband simulation results

In this section, we first show that the delayed RLS algorithms provide improvement in the MSD performance and then investigate the dependence of the performance on the delay. It will be shown that, for the SRLSd algorithm, the optimal delay is  $T = M/2$ , as discussed

in Section 3.3.2. However, for the ERLSd algorithm, there is no one-to-one relationship between the optimal delay and the forgetting factor  $\lambda$ .

We show that the MSE is useful for characterising the SIC performance if  $T = 0$ , i.e., for classical RLS algorithms. However, if  $T > 0$ , the MSE is not a useful characteristic for this purpose. We then show that the proposed SICF metric is suitable for characterising the SIC performance for both the cases, in particular by comparing it with the bit error rate (BER) performance of a far-end signal after the SIC.

In the simulation, we set the filter length to  $L = 50$ , and model the SI channel using the specified-spectra based simulator as described in Section 1.4.2. To simulate the decaying power delay profile in UWA channels, the parameter  $\gamma$  in (1.2) is chosen to make the ratio between the variance of latest arrivals and that of the first arrivals equal to 80 dB.

We assume a sampling frequency  $f_d = 1$  kHz, so that one channel tap delay is 1 ms. The parameter  $f_{\max}$  is used to define the maximum speed of the channel variation. To model fast time-varying channels, we use  $f_{\max} = 1$  Hz; for slow time-varying channels,  $f_{\max} = 0.1$  Hz.

In Fig. 3.5, a snapshot of the channel impulse response generated through the aforementioned process is shown, which has a similar shape as the SI channel impulse response obtained in our water tank experiments [1].

### 3.4.1 MSD performance of RLS algorithms with a delay

Fig. 3.6 shows the normalized MSD ( $\text{MSD}(i)/\|\mathbf{h}(i)\|_2^2$ ) as a function of the delay  $T$  against  $M$  for the SRLSd algorithm. The MSD performance is averaged over 20 simulation trials. The choice of  $M$  depends on the channel variation speed, the level of noise and other interference. The faster the channel variation, the smaller  $M$  should be chosen. The higher the noise level, the higher  $M$  is required. The SRLSd algorithm can provide a significant improvement in the MSD performance compared to the SRLS algorithm ( $T = 0$ ). It can be seen that the optimal delay is  $T = M/2$ . The minimum MSD is achieved at  $T = M/2 = 50$  for  $M = 100$ . Fig. 3.6 also shows that with further increase in the delay  $T$ , the MSD increases and, as expected, reaches the same level at  $T = M$  as at  $T = 0$ .

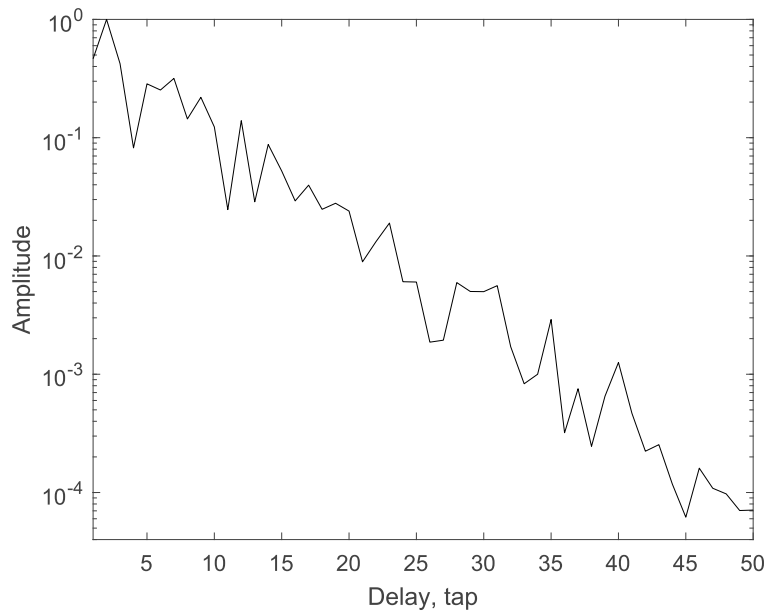


Fig. 3.5 A snapshot of the channel impulse response.

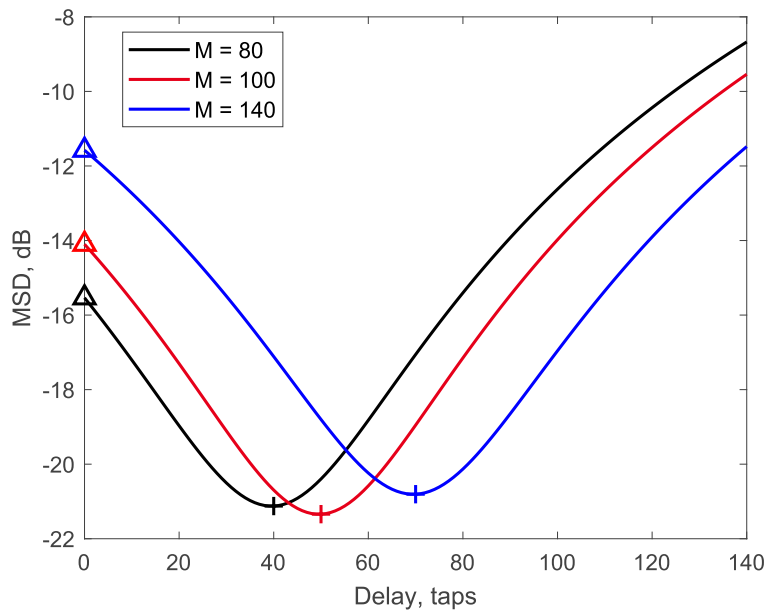


Fig. 3.6 MSD performance of the SRLS (Delay  $T = 0$ ) and SRLSd algorithms. The optimal delay minimising the MSD is  $T = M/2$ .

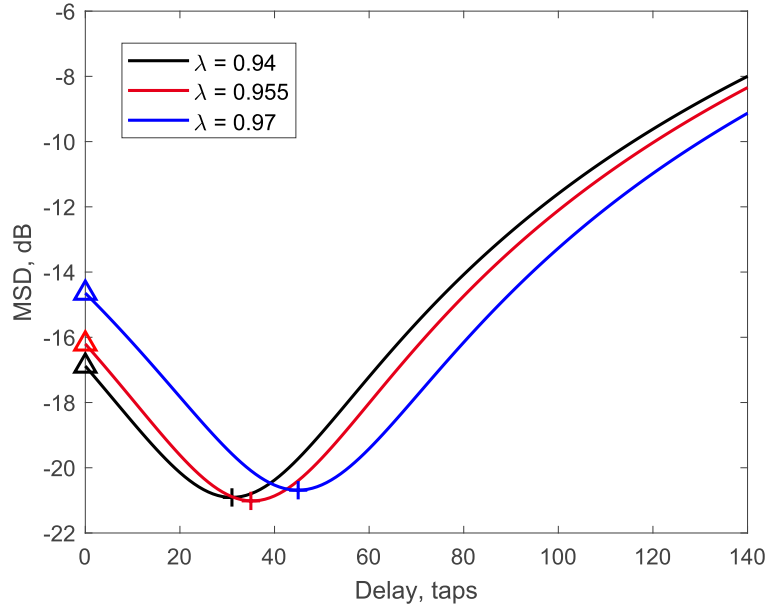


Fig. 3.7 MSD performance of the ERLS (Delay  $T = 0$ ) and ERLSd algorithms.

In Fig. 3.7, we observe that the MSD performance of the ERLS algorithm can also be improved by introducing a delay. As can be seen, in this simulation scenario, the minimum MSD is achieved for  $\lambda = 0.955$  and  $T = 37$ . For  $\lambda = 0.94$  and  $\lambda = 0.97$ , the minimum MSD is achieved at  $T = 31$  and  $T = 45$ , respectively. For the ERLS algorithm, from Fig. 3.7, one can arrive at the following approximate expression for the optimal delay  $T_{\text{opt}}$ :

$$T_{\text{opt}} \approx \frac{\beta}{\sqrt{1 - \lambda}}, \quad (3.42)$$

where  $\beta = 7.8$ . Note that (3.42) cannot provide the optimal delay precisely, it can only be used as a reference.

To investigate if the dependencies between the optimal delay and the window parameters can be applied generally, we ran 1000 simulation trials to find the distribution of the optimal delay for the SRLSd and ERLSd adaptive filters, with  $M = 100$  and  $\lambda = 0.955$ . The results show that, for the SRLSd algorithm, the optimal delay is always  $T = M/2$  in all simulation trials. However, for the ERLSd adaptive filter, the minimum MSD is obtained at  $T = 37$  in 91.5% of the trials, while, in the other trials, the optimal delay is  $T = 36$  or  $T = 38$ .

### 3.4.2 MSE, MSD and SIC performance of SRLS, SRLSd and SRLS-P algorithms

Fig. 3.8 presents the MSE, MSD and SICF of the adaptive filters in slow and fast varying channels. The MSE, MSD and SIC performance are computed over the steady-state part of the learning curve from 1000 to 5000 samples. The average interval for the SIC factor computation is 4 s. These three evaluation metrics are all averaged over 20 simulation trials. We consider the case when the power of the far-end signal is significantly higher than the noise power, thus the noise is not added to the far-end signal. The far-end signal to SI ratio is set to  $-43$  dB.

We can see that, for the SRLS algorithm ( $T = 0$ ), the optimal sliding window length  $M$  found from the MSE and MSD curves is about the same ( $M = 60$  or  $70$ ). However, for the other algorithms with  $T > 0$ , the optimal  $M$  corresponding to the minimum MSE and MSD are different.

The SRLS-P adaptive filter has a significantly improved MSD performance compared to the SRLSd algorithm, which in turn outperforms the SRLS algorithm. Note that, in the SRLS-P algorithm, there are  $3L$  unknown parameters to be estimated. Therefore, since the estimation interval in the SRLS-P algorithm is  $2M$ , the estimation requires the window length to be at least  $M = 3L/2 = 75$ ; this explains the high MSD at low  $M$ .

The results in Fig. 3.8 show that the MSE is lower than the far-end signal to SI ratio for the SRLSd adaptive filter with  $M < 80$ . This indicates that the far-end signal is partly cancelled, therefore the MSE is not useful as a performance measure here. In Fig. 3.8 (e) and (f), we show the SICF of the adaptive filters together with the inverse MSD. It is seen that the SICF and the inverse MSD for the SRLS adaptive filter are nearly the same, as expected from (3.11). For the adaptive filters with delay, there is some discrepancy between them for small  $M$ . We will show in the next section that the proposed SICF metric provides a better indication of performance of the SI canceller than the MSD.

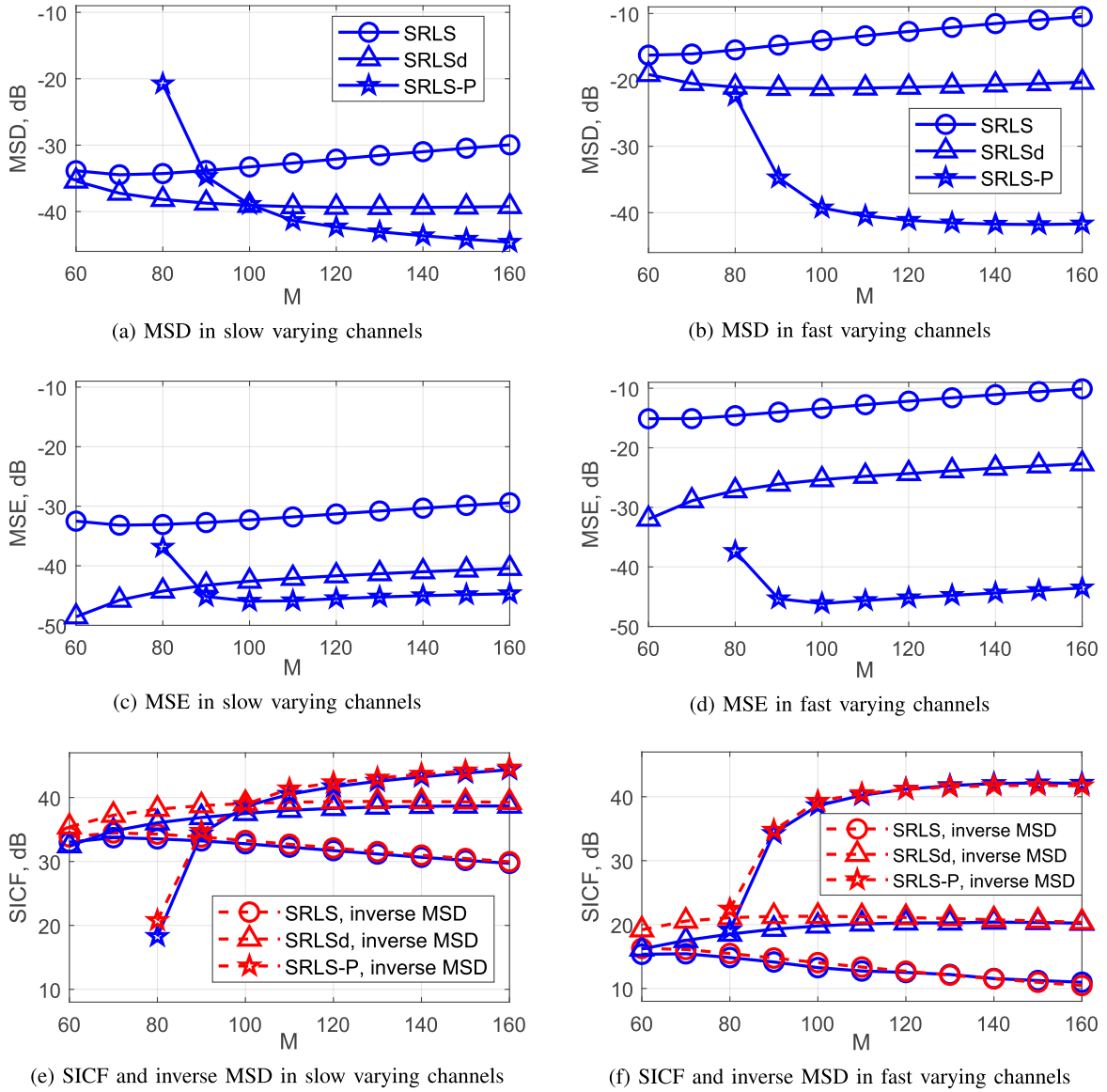


Fig. 3.8 MSD, MSE and SIC performance of the SRLS, SRLSd, and SRLS-P adaptive filters in slow and fast varying SI channels.

### 3.4.3 MSD, SIC and BER performance of SRLSd and SRLS-P algorithms

We now investigate the relationship between the MSD, SIC and BER performance provided by the SI canceller in the fast time-varying channel ( $f_{\max} = 1$  Hz) when using the SRLSd and SRLS-P algorithms.

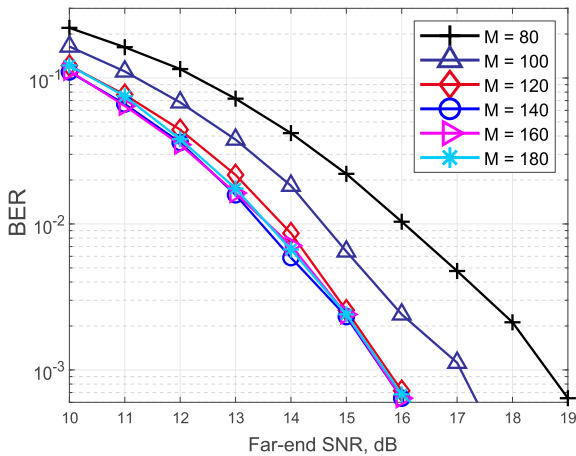
Fig. 3.9 shows these three characteristics for different values of  $M$ . We run 500 simulation trials, and in each trial a new time-varying channel is generated. The length of the realization is 15s. The received signal is generated by adding the far-end signal and noise to the SI channel output. Samples of the noise are generated as Gaussian random zero-mean numbers. The noise variance  $\sigma_n^2$  is set according to the SI to noise ratio ( $\text{SNR}_{\text{SI}}$ ), which is defined as:

$$\text{SNR}_{\text{SI}} = \frac{\text{E}\{|x(i)|^2\}}{\sigma_n^2}. \quad (3.43)$$

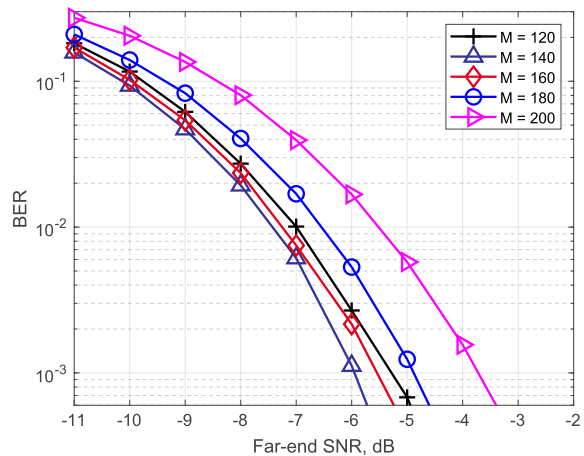
We use the BPSK direct sequence spread spectrum signal as the far-end signal. The chip rate is 1 kHz, the spreading factor is 250. The far-end channel is assumed to be a single path channel. The far-end signal level is defined by the far-end SNR as  $\sigma_f^2/\sigma_n^2$ . Here we set  $\text{SNR}_{\text{SI}} = 43$  dB. The SICF is computed over the steady-state period from 2 to 15 s, which is about ten times longer than the time correlation of the SI channel.

The performance of the SRLSd algorithm is shown in Fig. 3.9 (a), (c) and (e). Fig. 3.9 (a) shows the detection performance after SIC, which is an important indicator of the FD system performance. The best detection performance is achieved with  $M = 140$  or  $M = 160$  when the far-end SNR is lower than 16 dB. The BER slightly degrades for  $M = 120$ , and further degrades for smaller  $M$ . However, the MSD gives a different indication as the minimum MSD is achieved with  $M = 100$  or  $M = 120$  when the far-end SNR is lower than 16 dB.

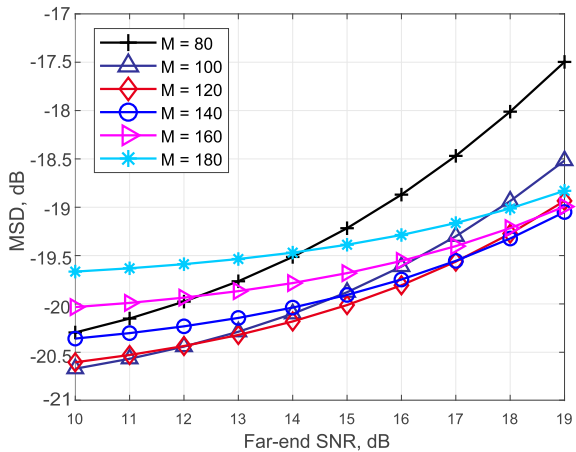
The SICF indicates that the best performance is achieved with  $M = 140$  when the far-end SNR lower than 14 dB and with  $M = 160$  when the far-end SNR between 14 dB and 19 dB. It is clear that the SICF provides a better indication of the optimal  $M$  for the detection performance. More importantly, in practice, the MSD is difficult to compute since the true



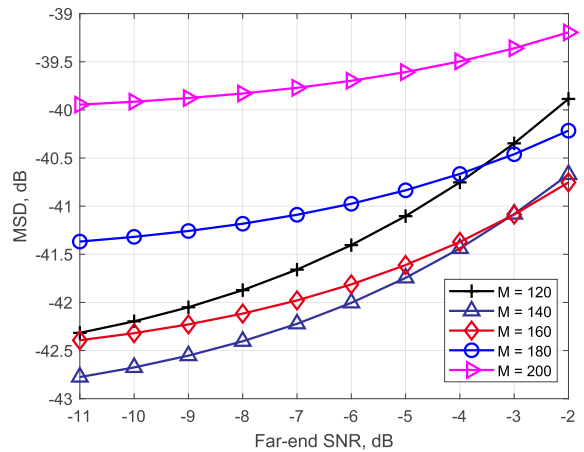
(a) BER performance for the SRLSd adaptive filter.



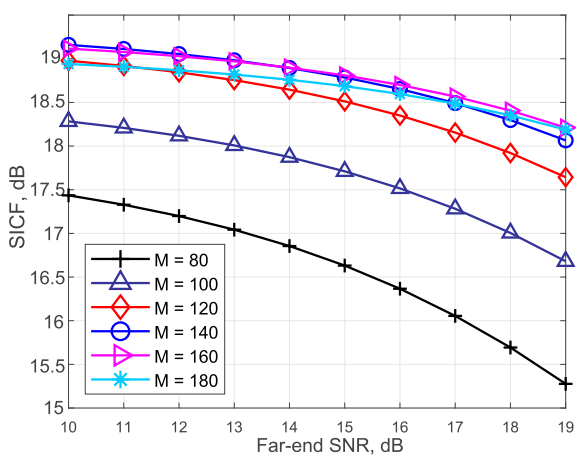
(b) BER performance for the SRLS-P adaptive filter.



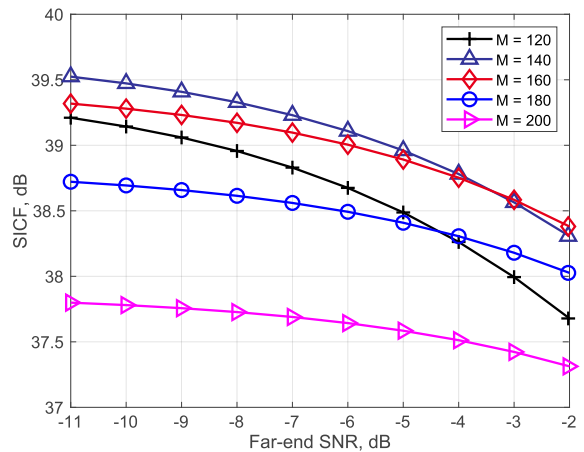
(c) MSD performance for the SRLSd adaptive filter.



(d) MSD performance for the SRLS-P adaptive filter.



(e) SIC performance for the SRLSd adaptive filter.



(f) SIC performance for the SRLS-P adaptive filter.

Fig. 3.9 BER, MSD and SIC performance for the SRLSd and SRLS-P adaptive filters in the fast varying SI channel.

channel response is unknown, whereas the proposed SICF metric is computed without such knowledge as explained in Section 3.2.

In Fig. 3.9 (b), (d) and (f), the BER, MSD and SIC performance of the SRLS-P algorithm are shown. The far-end SNR now varies from  $-11$  dB to  $-2$  dB. We consider much lower far-end signal level compared to that used for the SRLSd algorithm to generate the BER curves, as the SIC performance is significantly improved with the SRLS-P algorithm. It is seen that the optimal detection performance is achieved with  $M = 140$ . The dependence between  $M$  and the BER performance is consistent with that of the MSD and the SICF. Overall, the SRLS-P algorithm with optimal  $M$  outperforms the SRLSd adaptive filter by around 20 dB in terms of the MSD and SICF. It is observed that the BER curve with the optimal  $M$  is also shifted in the far-end SNR by about the same value.

### 3.5 Passband simulation results

In this section, we investigate the SIC scheme shown in Fig. 2.10 with the SRLS, SRLSd and SRLS-P adaptive filters in a passband simulation scenario with time-varying SI channel. The SI channel has one direct path between the projector and hydrophone and one path due to reflection from a time-varying surface. The reflected path is 20 dB weaker than the direct path. The surface is modelled as a sinusoid wave of 0.5 m amplitude and 3 s period. The projector and hydrophone are vertically separated by a distance of 0.5 m, their depths are 9.5 m and 10 m, respectively. We will show that the SIC performance can be significantly improved by the SRLS-P adaptive filter which accurately models the channel variation caused by the time-varying surface reflection.

In the simulation, a 10 s signal with BPSK modulation at a 12 kHz carrier frequency and with 1.2 kHz signal bandwidth is transmitted. The symbol rate is  $f_d = 1$  kHz. The BPSK symbols are pulse shaped using the root-raised cosine filter with a roll-off factor of 0.2. The sampling rate of the passband signal is 96 kHz.

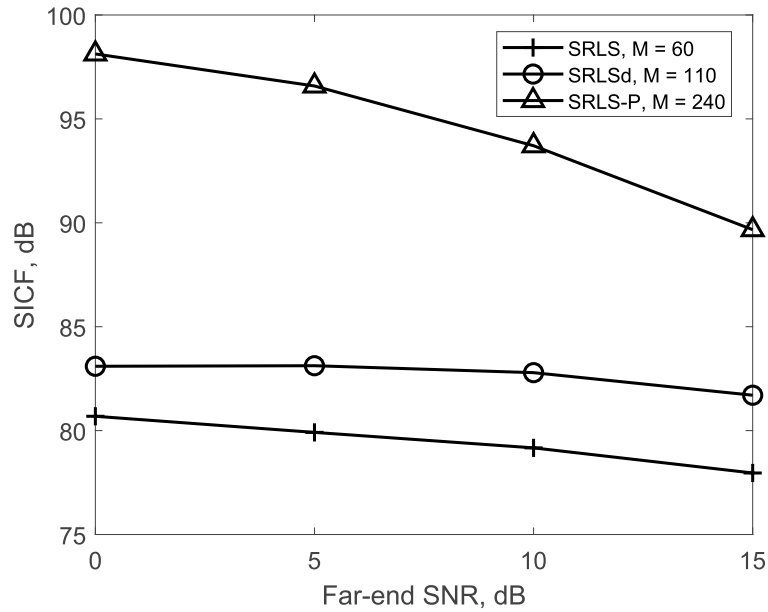


Fig. 3.10 SIC performance of adaptive filters in the passband simulation.

The received signal at the hydrophone is generated by adding the far-end signal and noise to the SI channel output. Here we set  $\text{SNR}_{\text{SI}} = 100$  dB and consider the far-end SNR between 0 dB and 15 dB.

Fig. 3.10 shows the SIC performance of the SRLS, SRLSd and SRLS-P adaptive filters. The SIC factor is computed over the time interval from 2 s to 10 s, i.e., the average interval for computing the SICF is 8 s. For each adaptive filter, the parameter  $M$  is adjusted to provide the highest SICF. The filter length is  $L = 40$ , which is long enough to cover both the main path and the surface reflection. With the SRLS adaptive filter, around 81 dB of SIC can be achieved at 0 dB far-end SNR ( $M = 60$ ). The SICF is improved by 3 dB when the SRLSd adaptive filter ( $M = 110$ ) is used, and it is further improved to 98 dB (by 14 dB) with the SRLS-P adaptive filter ( $M = 240$ ).

## 3.6 Experimental results

In this section, we investigate the SIC performance of the SRLS, SRLSd and SRLS-P adaptive filters in the lake experiment with the SIC scheme shown in Fig. 2.10. In the experiment, a

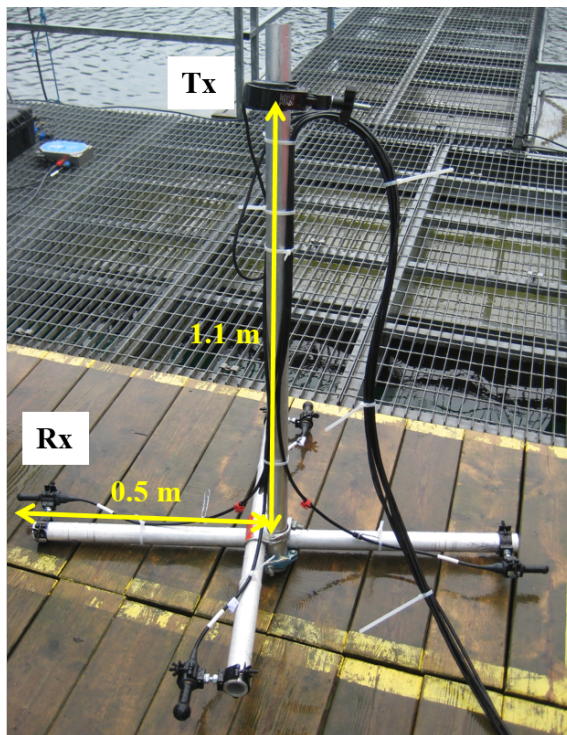


Fig. 3.11 The configuration of the lake experiments (Tx: projector; Rx: hydrophone).

Zoom F4 multitrack recorder [74] with a high-resolution 24-bit ADC is used to record the PA output and the hydrophone output. The PA output is fed to the recorder through an attenuator to avoid truncation of the signal or causing damage to the recorder due to the high voltage level.

The configuration and experimental setup are shown in Fig. 3.11 and 3.12, respectively. The lake depth at the experimental site is around 8 m. The distance between the projector and the hydrophone is around 1.3 m. The hydrophone is placed at 4 m depth. The experimental site is positioned in the middle of the lake. A photo of the lake surface during the experiments is given in Fig. A.1 (a). It was observed during the experiment that the amplitude of the surface waves varied from 5 cm to 10 cm. More information on the experimental site can be found in [79].

In the experiment, we transmit a 15 s BPSK signal at the carrier frequency  $f_c = 14$  kHz with a bandwidth of 1.2 kHz; the symbol rate is  $f_d = 1$  kHz; the pulse shaping roll-off factor is 0.2. The sampling rate is  $f_s = 96$  kHz. At 14 kHz, the transmit voltage response of the

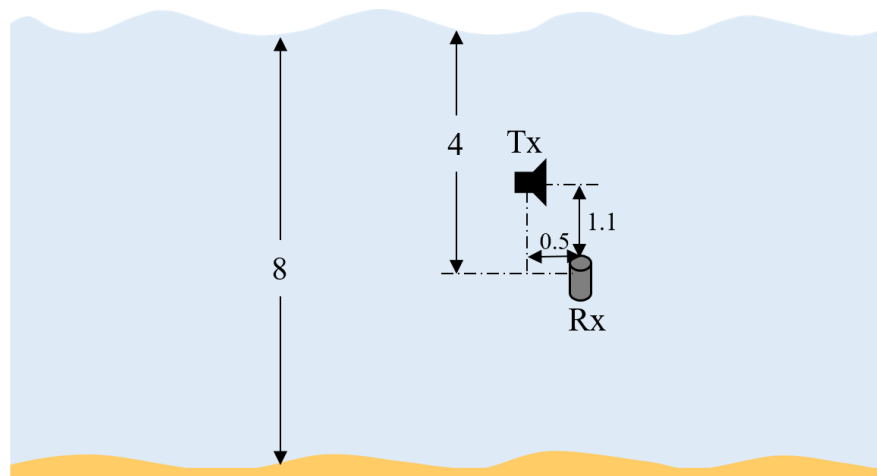


Fig. 3.12 The experimental setup. The distances are shown in meters.

transducer [78] is 118 dB re  $\mu\text{Pa}/\text{V}$  at 1 m. During the experiment, the sound pressure level at 1 m range is around 166 dB re  $\mu\text{Pa}$ .

In Fig. 3.13, we show the SI channel estimates obtained with the SRLS-P adaptive filter, which provides the highest SICF among the adaptive filters we considered. It can be seen that the SI channel consists of a strong and stable direct path and multiple fast time-varying paths due to reflections from the mounting system and from the lake surface and bottom. The direct path is the one associated with the highest amplitude (at tap 12). Apart from the direct path, there are also a few relatively stable reflections from the structure we used to fix the projector and hydrophone (shown in Fig. 3.11). Assuming the sound speed is 1500 m/s, the delay between the direct path and the first surface reflection should be around 3.4 ms. This is consistent with the channel estimates, as the first surface reflection arrives at the 16th tap. The rest of the multipath components are due to multiple reflections from the surface, bottom and the mounting system.

In the experiment, the SI to noise ratio is around 48 dB. The filter length is  $L = 80$ , which is long enough to cover the channel delay spread, including the direct path and multiple reflections from the surface and bottom. The SICF is computed over the time interval from 2 s to 15 s, i.e., over an interval of 13 s. Fig. 3.14 shows the SIC performance of the adaptive filters with the optimal sliding window lengths  $M$ . For the SRLS adaptive filter, at 0 dB

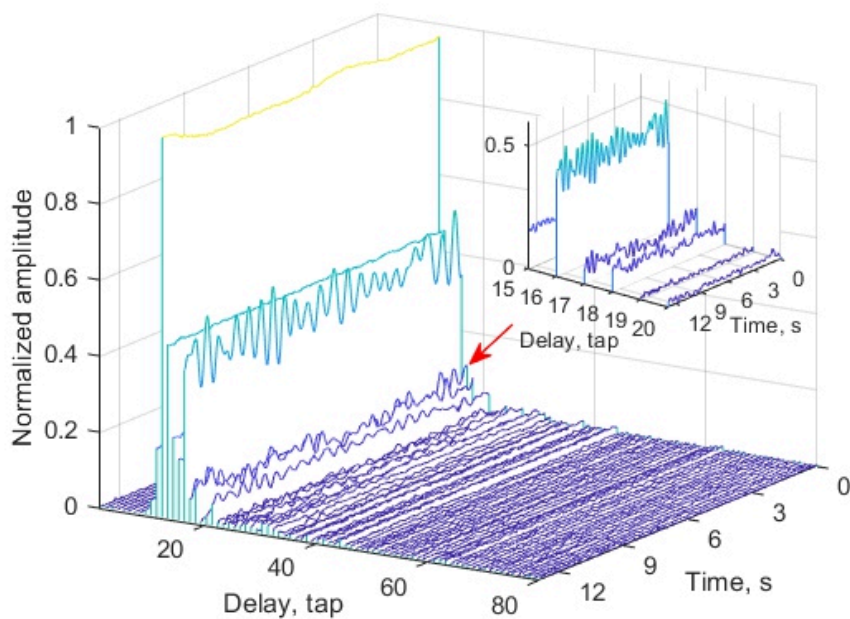


Fig. 3.13 SI channel estimate in the lake experiment. The channel delay spread is around 80 ms. It is observed that the first surface reflection (at the 16th tap) is fast-varying. The rest of the multipath components are the surface and the bottom reflections.

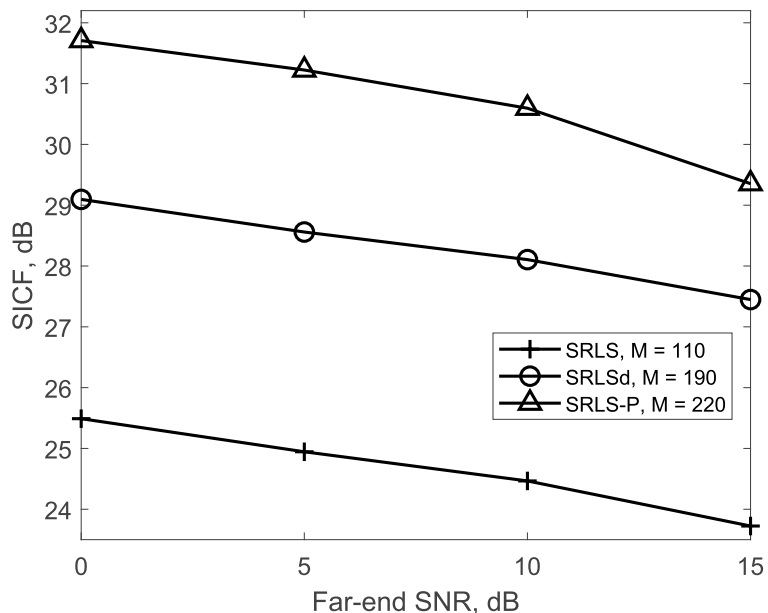


Fig. 3.14 SIC performance of adaptive filters in the lake experiment. The sliding window length  $M$  is chosen to provide the best performance of each adaptive filter.

far-end SNR, 25.5 dB of SIC is achieved when  $M = 110$ . The SICF is improved to 29 dB when the SRLSd adaptive filter with  $M = 190$  is used. The SRLS-P adaptive filter with  $M = 220$  achieves 32 dB of SICF.

The experimental results demonstrate that the SRLS-P adaptive filter provides the best SIC performance among the three adaptive filters. More than 6 dB improvement in the SICF can be achieved by using the SRLS-P adaptive filter compared to that of the SRLS adaptive filter.

However, it is seen that even with the SRLS-P adaptive filter, the level of the residual SI is still higher than the level of the far-end signal. At 0 dB far-end SNR, with 32 dB of SICF, the residual SI is 16 dB higher than the far-end signal. At 15 dB far-end SNR, the SICF is around 29 dB, and the residual SI is 4 dB higher than the far-end signal. However, with such a level of the SIC it becomes possible to detect far-end signals with specific modulation techniques, such as the spread-spectrum modulation as demonstrated in Section 3.4.

It can be seen that the improvement in SICF for the lake experiment is lower than that achieved in the passband simulation. The power spectral density computed for the first reflection from the lake surface (with an amplitude of about 0.4 as seen in Fig. 3.13), has shown that  $f_{\max} > 2$  Hz. For the further reflections from the lake surface and bottom, as can be seen in Fig. 3.13, the variation speed is even higher. With  $M = 220$ , the product of the estimation window length (0.44 s) by  $f_{\max}$  is already close to one, which is less than the Nyquist lower boundary. With such settings, one cannot expect high accuracy of estimating the SI channel due to high modelling errors [92]. Still, the SRLS-P algorithm shows improvement by 5.5 to 6 dB against the SRLS algorithm and by 1.5 to 2.5 dB against the SRLSd algorithm.

The estimation accuracy could have been improved using lower  $M$ . However, for the identifiability, the number of available signal samples ( $2M$ ) should be higher than the number of unknown parameters ( $3L$ ), i.e.  $M > 3L/2$ . For  $M$  very close to the boundary  $3L/2$ , the algorithm performance is limited (see Fig. 3.8). Reduction in  $L$  allows smaller  $M$ , but, in this case, the SIC performance will be limited by the SI arrivals being truncated by the filter.

### 3.7 Conclusions

In this chapter, the SICF has been proposed as a practical measure of the SIC performance in FD UWA systems. The SICF has been investigated in comparison with the MSE, MSD and BER. It is shown through numerical simulation that the proposed metric provides a good indication of the SI canceller performance.

To improve the SIC performance of the RLS adaptive filters, we have considered their delayed versions, the SRLSd and ERLSd adaptive filters. The dependence of the SIC performance on the delay of the input signals for these adaptive filters has been investigated using numerical simulations. We have shown that, for the SRLSd adaptive filter, the optimal delay is the half of the sliding window length. For the ERLSd adaptive filter, the relationship between the optimal delay and the forgetting factor can differ for different channel realizations, although, with an optimal delay, the ERLS adaptive filter can provide the same level of SIC performance as the SRLSd adaptive filter.

We have proposed the SRLS-P adaptive filter, which is based on the SRLS algorithm and modelling the channel response variation within a short time interval as a second-order algebraic polynomial. The SIC performance of the SRLS-P adaptive filter has been investigated and compared with that of the SRLS and SRLSd adaptive filters using numerical and lake experiments. Results show that the SRLS-P algorithm achieves the highest SICF among these adaptive filters.

# Chapter 4

## Basis Expansion Model Adaptive Filtering for Self-Interference Cancellation

In Chapter 3, we have proposed the SRLS-P adaptive filter for channel estimation of fast-varying SI channels, which exploits a parabolic approximation of the time-varying SI channel response. For the SRLS-P adaptive filter, one specific order of basis function is considered and the computational complexity is high. In this Chapter, we combine the SRLS adaptive algorithm with the BEM approach and propose low-complexity interpolating adaptive filters for estimation of fast time-varying channels. Specifically, as an example, we use the Legendre polynomials as the basis functions and solve the system of equations using DCD iterations, thus the name the SRLS-L-DCD adaptive filter. A sparse algorithm (HSRLS-L-DCD) based on homotopy iterations is then proposed to exploit the sparsity in the expansion coefficients. In Section 4.2, the SRLS-L adaptive filter and techniques proposed to reduce its complexity are described. Section 4.3 presents the proposed HSRLS-L-DCD adaptive filter. Section 4.4 investigates the channel estimation performance of the proposed algorithms and known algorithms in an FD scenario. In Section 4.5, the SIC performance of the proposed algorithms is investigated in FD lake experiments. In Section 4.6, conclusions are drawn.

The work in this chapter is presented in the paper: L. Shen, Y. Zakharov, L. Shi, and B. Henson, “BEM adaptive filtering for SI cancellation in FD underwater acoustic systems,” *submitted to Signal Processing*, Under review.

## 4.1 Introduction

Classical adaptive filtering algorithms such as the RLS algorithm, when used in identification scenarios, predict the channel response for the next time instant based on input data received at the current and past time instants. In general, for time-varying channels, predictive estimators are less accurate than interpolating estimators. The later, however, are non-causal since they require input data not only from the past but also from future time instants. If an application can accept a tracking delay, the interpolating adaptive filtering can significantly improve the identification performance.

In communication systems, BEMs are widely used for block (non-adaptive) estimation of time-varying channels, e.g. see [93–105]. The most often used BEMs are the Karhunen-Loeve functions [94, 96], discrete prolate spheroidal functions [98, 101–103], generalized complex exponentials [97–99], B-splines [100, 106], and algebraic polynomials [104, 107] including Legendre polynomials [108, 109]. With a BEM, estimation of a realization of the random process describing the time-variant channel is transformed into estimation of a vector of time-invariant expansion coefficients [101].

In [110], a predictive RLS adaptive filter was proposed based on representation of the time variation with algebraic polynomials. In Chapter 3, an interpolating adaptive filter based on the SRLS algorithm was proposed. This adaptive filter exploits a parabolic approximation of the time-varying SI channel response; however, it has a high complexity. In [104], a local basis function (LBF) estimator is proposed which combines the BEM and weighted least squares approaches. The LBF estimator provides an excellent tracking performance at the expense of a high computational complexity. A recursive computation is proposed to reduce the LBF estimator complexity for real-valued data for specific choices of basis functions; however, the overall complexity is still high. In [105], a fast version of the LBF

estimator (fLBF) is proposed with two steps, pre-estimation and post-filtering. The key idea is to find an initial estimate of the system impulse response by the ERLS algorithm, and then denoise the pre-estimated response by the LBF estimator. It is indicated in [105] that the fLBF algorithm can provide approximately the same performance as that of the LBF algorithm with significantly lower complexity under certain assumptions. This is verified by simulation results for a two-tap system. We show in Section 4.4 that the performance of the fLBF estimator in FD scenarios, with a large number of taps, is not as good as that of the LBF estimator.

For SI channels in FD UWA systems, different multipath components may have different speed of time variation. The direct path between the transmitter and receiver and other paths with reflection from static objects can be slowly varying in time, whereas paths with reflection from a moving sea/lake surface can be fast-varying [63, 69, 89]. Therefore, in addition to the normal sparsity of the UWA channel [61] there will be an extra sparsity in the basis expansion coefficients. This sparsity can be exploited to improve the SIC performance.

## 4.2 Proposed SRLS-L adaptive filter

In subsection 4.2.1, we introduce the signal model. In subsection 4.2.2, we describe the BEM based SRLS algorithm in a general form and specify it for Legendre polynomials. Finally, in subsection 4.2.3, we propose techniques for reducing the algorithm complexity by exploiting the time-shifted structure of the regressor.

### 4.2.1 Signal model

The observed discrete-time signal at time instant  $i$  is given by

$$x(i) = \mathbf{h}^H(i)\mathbf{s}(i) + n(i), \quad (4.1)$$

where  $\mathbf{s}(i) = [s(i), s(i-1), \dots, s(i-L+1)]^T$  is an  $L \times 1$  regressor vector,  $s(i)$  is the input signal to the system (channel) with a time-varying impulse response  $\mathbf{h}(i)$  to be identified, and  $n(i)$  is a noise signal. For derivation in this section, we will ignore the noise  $n(i)$ .

We assume that within a time interval  $[i - M_o, i + M_o]$  centred at the time instant  $i$ , the time-varying response can be accurately approximated by  $(P + 1)$  basis functions  $\phi_p(k)$  [104]:

$$\mathbf{h}(i+k) = \sum_{p=0}^P \mathbf{c}_p(i) \phi_p(k), \quad k = -M_o, \dots, M_o, \quad (4.2)$$

where  $M_o = (M - 1)/2$  and  $M$  is the sliding window length; here, for convenience of presentation, we will assume that  $M$  is odd, however the results can be easily extended to the case of even  $M$ . The  $L \times 1$  vectors of expansion coefficients  $\mathbf{c}_p(i)$  should be estimated, where  $L$  is the length of the impulse response.

The orthogonal Legendre algebraic polynomials, which we will be using as an example BEM, are defined as [111]:

$$L_p(\tau) = \frac{1}{2^p p!} \frac{d^p}{d\tau^p} [(\tau^2 - 1)^p], \quad -1 < \tau < 1, \quad p \geq 0. \quad (4.3)$$

Fig. 2.15 shows different orders of the Legendre polynomials. The basis functions  $\phi_p(k)$  are then given by:

$$\phi_p(k) = L_p\left(\frac{2k}{M-1}\right). \quad (4.4)$$

### 4.2.2 SRLS-L algorithm

We now consider the following vectors:

$$\mathbf{b}_p(i) = \mathbf{S}^T(i) \mathbf{W} \Phi_p \mathbf{x}^*(i), \quad p = 0, \dots, P, \quad (4.5)$$

where  $\Phi_p = \text{diag}\{\phi_p(M_o), \dots, \phi_p(-M_o)\}$  is an  $M \times M$  diagonal matrix,  $\mathbf{S}(i) = [s(i), \dots, s(i-M+1)]^T$  is the  $M \times L$  regressor matrix,  $\mathbf{x}(i) = [x(i), x(i-1), \dots, x(i-M+1)]^T$  is an  $M \times 1$  desired signal vector, and  $\mathbf{W} = \text{diag}\{w(M_o), \dots, w(-M_o)\}$  is an  $M \times M$  diagonal matrix, where the diagonal elements (weights) form a non-negative symmetric bell-shaped

window. The weights are applied to put more emphasis on the data close to the middle of the time window [104, 105]. Equation (4.5) can be written as:

$$\begin{aligned}\mathbf{b}_p(i) &= \sum_{k=0}^{2M_o} \psi_p(M_o - k) \mathbf{s}(i - k) \mathbf{s}^H(i - k) \mathbf{h}(i - k) \\ &= \sum_{k=-2M_o}^0 \psi_p(M_o + k) \mathbf{R}(i + k) \mathbf{h}(i + k),\end{aligned}\quad (4.6)$$

where  $\psi_p(k) = w(k)\phi_p(k)$ , and the second equality is obtained by replacing  $k$  with  $-k$ ,  $\mathbf{R}(i) = \mathbf{s}(i)\mathbf{s}^H(i)$  and, further replacing  $i$  with  $i + M_o$ ,

$$\mathbf{b}_p(i + M_o) = \sum_{k=-M_o}^{M_o} \psi_p(k) \mathbf{R}(i + k) \mathbf{h}(i + k). \quad (4.7)$$

By substituting (4.2) into (4.7), we obtain:

$$\begin{aligned}\mathbf{b}_p(i + M_o) &= \sum_{k=-M_o}^{M_o} \psi_p(k) \mathbf{R}(i + k) \sum_{q=0}^P \mathbf{c}_q(i) \phi_q(k) \\ &= \sum_{q=0}^P \mathcal{R}_{p,q}(i) \mathbf{c}_q(i),\end{aligned}\quad (4.8)$$

where

$$\begin{aligned}\mathcal{R}_{p,q}(i) &= \sum_{k=-M_o}^{M_o} \psi_p(k) \mathbf{R}(i + k) \phi_q(k) \\ &= \sum_{k=-M_o}^{M_o} w(k) \phi_p(k) \mathbf{R}(i + k) \phi_q(k) \\ &= \sum_{k=-M_o}^{M_o} \varphi_p(k) \mathbf{R}(i + k) \varphi_q(k),\end{aligned}\quad (4.9)$$

and  $\varphi_p(k) = \sqrt{w(k)}\phi_p(k)$ . By further denoting

$$\mathcal{R}(i) = \begin{bmatrix} \mathcal{R}_{0,0}(i) & \dots & \mathcal{R}_{0,P}(i) \\ \dots & \dots & \dots \\ \mathcal{R}_{P,0}(i) & \dots & \mathcal{R}_{P,P}(i) \end{bmatrix}, \quad (4.10)$$

Table 4.1 SRLS-L algorithm

| Step | Equation   |
|------|--|
|      | for $i > 0$ , repeat:  |
| 1    | Generate vectors $\mathbf{b}_p(i + M_o)$ using (4.5)   |
| 2    | Compute matrices $\mathcal{R}_{p,q}(i)$ as in (4.9)  |
| 3    | Generate the matrix $\mathcal{R}(i)$ as in (4.10) and vector $\mathbf{b}(i)$   |
| 4    | Find a solution $\hat{\mathbf{c}}$ to the system $[\mathcal{R}(i) + \epsilon \mathbf{I}_{(P+1)L}] \mathbf{c}(i) = \mathbf{b}(i)$ |
| 5    | Compute the estimate $\hat{\mathbf{h}}(i) = \sum_{p=0}^P \hat{\mathbf{c}}_p(i) \phi_p(0)$  |

$\mathbf{b}(i) = [\mathbf{b}_0^T(i + M_o), \dots, \mathbf{b}_P^T(i + M_o)]^T$  and  $\mathbf{c}(i) = [\mathbf{c}_0^T(i), \dots, \mathbf{c}_P^T(i)]^T$ , we obtain a system of equations with respect to the unknown  $(P + 1)L \times 1$  vector  $\mathbf{c}(i)$ :

$$\mathcal{R}(i)\mathbf{c}(i) = \mathbf{b}(i). \quad (4.11)$$

By solving this system, we find an estimate  $\hat{\mathbf{c}}(i)$  of the expansion coefficients  $\mathbf{c}(i)$  for representation of the time-varying impulse response  $\mathbf{h}(i)$  in (4.2). We are only interested in the estimate for  $k = 0$ ; therefore, the channel estimate at time instant  $i$  is given by:

$$\hat{\mathbf{h}}(i) = \sum_{p=0}^P \hat{\mathbf{c}}_p(i) \phi_p(0). \quad (4.12)$$

The SRLS-L algorithm is summarized in Table 4.1, where  $\epsilon > 0$  is a regularization parameter used to stabilize the solution of the system in (4.11). Note that the sliding window length  $M$  in the SRLS-L algorithm should satisfy the condition  $M > (P+1)L$ ; otherwise, the matrix  $\mathcal{R}(i)$  will have a rank less than  $(P + 1)L$  and the system (4.11) will be ill-conditioned.

In [104], the LBF estimator is proposed under the same concept. However, the LBF estimator is only applicable for real-valued data and it is of a high complexity. A recursive computation scheme was proposed in [104] to reduce the complexity of the LBF estimator, but the complexity is still high (see complexity analysis in Appendix C). In addition, to allow the recursive computation, there are constraints on the choice of basis functions. On the other hand, the adaptive filter that we propose has no constraint on the choice of basis functions, it is also designed for complex-valued systems and its complexity is lower than that of the LBF

estimator. We show in subsection 4.2.3 how the complexity of the SRLS-L adaptive filter can be significantly reduced.

### 4.2.3 Complexity of the SRLS-L adaptive filter

In this subsection, the complexity analysis is presented for the complex-valued SRLS-L algorithm and techniques are proposed to reduce the complexity.

The complexity of the SRLS-L algorithm is mainly determined by the computation of the matrices  $\mathcal{R}_{p,q}(i)$  in (4.9) and vectors  $\mathbf{b}_p(i + M_o)$  in (4.5) and solving the system of equations (4.11). We first show how the complexity of the matrix and vector computation can be reduced and then discuss a reduction in complexity by recursively solving the system of equations.

#### Matrix $\mathcal{R}_{p,q}(i)$

The direct computation of the matrix  $\mathcal{R}_{p,q}(i)$  would require  $4ML^2$  MAC (multiply and accumulate) operations. We will show that this can be reduced by recursive computations and by using the FFTs. Firstly, we show that  $\mathcal{R}_{p,q}(i)$  can be efficiently computed using elements in  $\mathcal{R}_{p,q}(i - 1)$ .

*Proposition:* The following relationship holds for elements  $[\mathcal{R}_{p,q}(i)]_{m+1,n+1}$ ,  $m, n = 1, \dots, L - 1$ , of the matrix  $\mathcal{R}_{p,q}(i)$ :

$$[\mathcal{R}_{p,q}(i)]_{m+1,n+1} = [\mathcal{R}_{p,q}(i - 1)]_{m,n}. \quad (4.13)$$

*Proof:* The matrix  $\mathcal{R}_{p,q}(i)$  in (4.9) can be represented as:

$$\mathcal{R}_{p,q}(i) = \sum_{k=-\infty}^{\infty} v_{p,q}(k) \mathbf{R}(i + k), \quad (4.14)$$

where coefficients  $v_{p,q}(k)$  are defined as:

$$v_{p,q}(k) = \begin{cases} w(k)\phi_p(k)\phi_q(k), & \text{if } -M_o \leq k \leq M_o \\ 0, & \text{otherwise} \end{cases}. \quad (4.15)$$

This can also be rewritten as:

$$\mathcal{R}_{p,q}(i) = \sum_{k=-\infty}^{\infty} v_{p,q}(k-i)\mathbf{R}(k). \quad (4.16)$$

The  $(m+1, n+1)$ th element of  $\mathcal{R}_{p,q}(i)$  is given by:

$$[\mathcal{R}_{p,q}(i)]_{m+1,n+1} = \sum_{k=-\infty}^{\infty} v_{p,q}(k-i)[\mathbf{R}(k)]_{m+1,n+1}. \quad (4.17)$$

Since  $[\mathbf{R}(k)]_{m+1,n+1} = s(k-m)s^*(k-n)$ , we have:

$$[\mathcal{R}_{p,q}(i)]_{m+1,n+1} = \sum_{k=-\infty}^{\infty} v_{p,q}(k-i)s(k-m)s^*(k-n). \quad (4.18)$$

The  $(m, n)$ th element of  $\mathcal{R}_{p,q}(i-1)$  is given by:

$$[\mathcal{R}_{p,q}(i-1)]_{m,n} = \sum_{k=-\infty}^{\infty} v_{p,q}(k-i+1)[\mathbf{R}(k)]_{m,n}. \quad (4.19)$$

Since  $[\mathbf{R}(k)]_{m,n} = s(k-m+1)s^*(k-n+1)$ , we obtain:

$$\begin{aligned} [\mathcal{R}_{p,q}(i-1)]_{m,n} &= \sum_{k=-\infty}^{\infty} v_{p,q}(k-i+1)s(k-m+1)s^*(k-n+1) \\ &= \sum_{k=-\infty}^{\infty} v_{p,q}(k-i)s(k-m)s^*(k-n) \\ &= [\mathcal{R}_{p,q}(i)]_{m+1,n+1}. \end{aligned} \quad (4.20)$$

This equality holds for  $m, n = 1, \dots, L-1$ .

This proposition shows that  $(L-1)^2$  elements of the matrix  $\mathcal{R}_{p,q}(i)$  at time instant  $i$  are the same as elements of the matrix  $\mathcal{R}_{p,q}(i-1)$  at time instant  $i-1$ . Therefore, only  $2L-1$

elements of the matrix  $\mathcal{R}_{p,q}(i)$  require computation. Since the matrix  $\mathcal{R}_{p,q}(i)$  is Hermitian, only one column of length  $L$  should be updated. Thus, the complexity of the computation of  $\mathcal{R}_{p,q}(i)$  is reduced from  $4ML^2$  to  $4ML$  MACs.

We now show how the FFT can be used to further reduce the complexity. We only need to compute the first column of the matrix  $\mathcal{R}_{p,q}(i)$ . This column can be represented as

$$\begin{aligned} [\mathcal{R}_{p,q}(i)]_{:,1} &= \sum_{k=-M_o}^{M_o} v_{p,q}(k)s(i+k)\mathbf{s}^*(i+k) \\ &= \sum_{k=-M_o}^{M_o} \tilde{v}_{p,q}(k)\mathbf{s}^*(i+k), \end{aligned} \quad (4.21)$$

where  $\tilde{v}_{p,q}(k) = v_{p,q}(k)s(i+k)$ . We therefore can think of the column  $[\mathcal{R}_{p,q}(i)]_{:,1}$  as a result of convolution of sequences  $[s^*(i - M_o - L + 1), \dots, s^*(i + M_o)]$  and  $\tilde{v}_{p,q}(k)$ ,  $k = -M_o, \dots, M_o$ . The time-domain convolution can be replaced with frequency-domain multiplication based on the convolution theorem [112] and the use of FFTs. FFTs of size  $(M + L)$  are used to include the length of the sequence  $M$  and the maximum delay  $L$ . One needs to compute FFTs of these two sequences, multiply them (taking one of them as complex-conjugate), and compute the inverse FFT. Therefore, the complexity of these computations is about three FFT operations of size  $(L + M)$ . This is instead of the direct computation, which would require about  $4ML$  MACs.

Thus, depending on the filter length  $L$  and the sliding window length  $M$ , the complexity of computing the matrix  $\mathcal{R}_{p,q}(i)$  at every time instant  $i$  can be either  $4ML$  MACs or 3 FFTs of size  $(L + M)$ , whatever is smaller.

As an example, for the case of  $M = 145$  and  $L = 80$ , direct computation of the matrix  $\mathcal{R}_{p,q}(i)$  would require  $3.7 \times 10^6$  MACs. Instead, direct computation of one column  $[\mathcal{R}_{p,q}(i)]_{:,1}$  would require  $4.6 \times 10^4$  MACs. The complexity is further reduced to around  $5.3 \times 10^3$  MACs when using the FFTs as described above.

**Vector  $\mathbf{b}_p(i + M_o)$** 

The direct computation of the vector requires  $4ML$  MAC operations. Note that (4.5) can be thought of as convolution of the sequences  $s(i+k)$  of length  $(L+M)$  and  $\mathbf{x}_p^*(i) = \mathbf{W}\Phi_p\mathbf{x}^*(i)$  of length  $M$ . This again can be done using the FFT of length  $(L+M)$  with a complexity of three FFT operations of size  $(L+M)$ .

**System of equations (4.11)**

A direct solution of the system in (4.11) would require about  $4(P+1)^3L^3$  MACs. However, the expansion coefficient vector at time instant  $i$  can be updated based on the estimate  $\hat{\mathbf{c}}(i-1)$  found at the previous time instant:

$$\hat{\mathbf{c}}(i) = \hat{\mathbf{c}}(i-1) + \Delta\mathbf{c}(i). \quad (4.22)$$

The system of equation at Step 4 of the algorithm in Table 4.2 is replaced by:

$$\left[ \mathcal{R}(i) + \varepsilon\mathbf{I}_{(P+1)L} \right] \Delta\mathbf{c}(i) = \mathbf{r}(i), \quad (4.23)$$

where  $\mathbf{r}(i)$  is a residual vector computed as:

$$\mathbf{r}(i) = \mathbf{b}(i) - \mathcal{R}(i)\hat{\mathbf{c}}(i-1). \quad (4.24)$$

The computation of the residual vector requires about  $4(P+1)^2L^2$  MACs. An estimate of the increment  $\Delta\mathbf{c}(i)$  can be found recursively using the leading DCD algorithm [86, 87] presented in Table 4.2, where  $H$  is an initial step size,  $M_b$  is the maximum number of bits used to represent the solution vector,  $N_u$  defines the maximum number of ‘successful’ DCD iterations per time instant,  $\alpha$  is the direction vector, and  $\delta$  is the step size used for updating the solution vector. Solving the system of equation in (4.23) would require at most  $4N_u(P+1)L + M_b$  additions.

The SRLS-L algorithm directly solves the system of equations, and therefore its overall complexity is  $3(P+1)^2/2 + 3(P+1)$  FFT operations of size  $(L+M)$  and extra about

Table 4.2 Leading DCD algorithm

| Step | Input: $P, L, H, M_b, N_u, \hat{\mathbf{c}}, \mathcal{R}, \mathbf{r}$<br>Initialization: $\delta = H, u = 0$ | Output: $\hat{\mathbf{c}}$ |
|------|--|----------------------------|
|      | for $m = 1, \dots, M_b$  |                            |
| 1    | $\delta = \delta/2, \boldsymbol{\alpha} = [\delta, -\delta, j\delta, -j\delta], \text{Flag} = 1$             |                            |
| 2    | While $u \leq N_u$ and Flag = 1  |                            |
| 3    | $[n, s] = \arg \max_{t=1, \dots, (P+1)L} \{ \Re(r_t) ,  \Im(r_t) \}$   |                            |
| 4    | if $s = 1$ , then $r_{\text{tmp}} = \Re(r_n)$ ,  |                            |
| 5    | else $r_{\text{tmp}} = \Im(r_n)$   |                            |
| 6    | if $r_{\text{tmp}} > (\alpha/2)\mathcal{R}_{n,n}$  |                            |
| 7    | $\hat{\mathbf{c}}_n = \hat{\mathbf{c}}_n + \text{sign}(r_{\text{tmp}})s\boldsymbol{\alpha}$                  |                            |
| 8    | $\mathbf{r} = \mathbf{r} - \text{sign}(r_{\text{tmp}})\boldsymbol{\alpha}\mathbf{R}^{(n)}$                   |                            |
| 9    | $u = u + 1$  |                            |
| 10   | else, Flag = 0   |                            |
|      | end  |                            |

$4(P + 1)^3 L^3$  MACs for solving the system of equations. The overall complexity of the SRLS-L-DCD adaptive filter, which approximately solves the system of equations, is  $3(P + 1)^2/2 + 3(P + 1)$  FFT operations of size  $(L + M)$ , and extra about  $4(P + 1)^2 L^2$  MACs and  $4N_u(P + 1)L + M_b$  additions for DCD iterations. The complexity of the SRLS-L and SRLS-L-DCD algorithms will be compared with the complexity of other algorithms in Section 4.4.

### 4.3 Homotopy SRLS-L-DCD adaptive filter

For fast-varying channels with a large delay spread, the minimum sliding window length required is significantly increased when high orders of the basis functions are used. In practice, there is sparsity in the expansion coefficients. By exploiting the sparsity, the sliding window length can be reduced, which in turn will improve the tracking performance of the SRLS-L algorithm.

In this section, we modify the SRLS-L algorithm by exploiting the sparsity in the expansion coefficients and propose a new sparse adaptive filter well suited to estimation of fast time-varying channels. Specifically, the sparse recovery problem is solved using the

homotopy principle and DCD iterations. The new adaptive filter is named the HSRLS-L-DCD adaptive filter.

In the SRLS-L and SRLS-L-DCD algorithms, the LS criterion is used (or weighted LS criterion if non-uniform weightings are used) resulting in a system of equations solved directly or using DCD iterations, respectively. In the HSRLS-L-DCD algorithm, we find a solution by minimizing the following cost function [113]:

$$J[\mathbf{c}(i)] = \frac{1}{2} \mathbf{c}^H(i) \mathcal{R}(i) \mathbf{c}(i) - \Re\{\mathbf{c}^H(i) \mathbf{b}(i)\} + \tau \tilde{\mathbf{w}}^T(i) \|\mathbf{c}(i)\|, \quad (4.25)$$

where the first two terms represent the LS cost, the third term is a penalty function ( $\ell_1$  norm of the solution) that favours sparse solutions,  $\tau$  is a positive regularization parameter which controls the balance between the LS fitting and the penalty and  $\tilde{\mathbf{w}}$  is a weight vector which is updated in reweighting iterations [114].

If the estimate at the previous time instant  $\hat{\mathbf{c}}(i-1)$  is used as a warm-start as shown in (4.22), then (4.25) can be replaced with:

$$\Delta J[\Delta \mathbf{c}(i)] = \frac{1}{2} \Delta \mathbf{c}^H(i) \mathcal{R}(i) \Delta \mathbf{c}(i) - \Re\{\Delta \mathbf{c}^H(i) \mathbf{r}(i)\} + \tau \tilde{\mathbf{w}}^T(i) \|\mathbf{c}(i)\|. \quad (4.26)$$

The LS- $\ell_1$  optimization problem can be solved by the homotopy  $\ell_1$ -DCD ( $\text{H}\ell_1$ -DCD) algorithm [115], which is based on homotopy with respect to the regularization parameter  $\tau$ . If  $\tau$  is high, the third term of (4.26) dominates the cost function and forces the cardinality of the support to zero. The parameter  $\tau$  is initialized to the highest possible value which guarantees that the algorithm starts with a zero support. This is done to allow us to keep a low dimension of the problem and to reduce the complexity [115]. After each homotopy iteration, the regularization parameter is reduced by a positive factor  $\gamma < 1$ .

The  $\text{H}\ell_1$ -DCD algorithm is summarized in Table 4.3. In adaptive filtering, homotopy iterations are distributed in time to reduce the complexity [91, 116]. Therefore, only one homotopy iteration is performed at each time instant. In each homotopy iteration, an element

Table 4.3  $H\ell_1$ -DCD algorithm

|      |   |
|------|---|
|      | Input parameters: $M_0, P, L, H, M_b, N_u, \tau, \gamma, \mu_d, \mu_c, \mu_w$   |
|      | Output: $\hat{\mathbf{c}}, \tilde{\mathbf{w}}$  |
| Step | Initialization: $I = \emptyset, \mathcal{R} = \mathcal{R}(i), \mathbf{c} = \mathbf{0}, \mathbf{b} = \mathbf{r}(i), \tilde{\mathbf{w}} = \mathbf{1}_L$   |
|      | for $i > 0$ , repeat:   |
| 1    | $\tau = \max_k  b_k $   |
| 2    | Remove $t$ th element from $I$ ( $I \leftarrow I \setminus t$ ), if<br>$t = \arg \min_{k \in I} \frac{1}{2}  c_k ^2 \mathcal{R}_{k,k} + \Re\{c_k^* b_k\} - \tau \tilde{w}_k  c_k $<br>and $\frac{1}{2}  c_k ^2 \mathcal{R}_{k,k} + \Re\{c_k^* b_k\} - \tau \tilde{w}_k  c_k  < 0$ |
| 3    | If the $t$ th element is removed, then update:<br>$\mathbf{b} = \mathbf{b} + c_t \mathcal{R}^{(t)}$   |
| 4    | Include $t$ th element into the support ( $I \leftarrow I \cup t$ ), if<br>$t = \arg \max_{k \in I} \frac{( b_k  - \tau \tilde{w}_k)^2}{\mathcal{R}_{k,k}}$ and $ b_k  > \tau \tilde{w}_k$  |
| 5    | Update the regularization parameter: $\tau = \gamma \tau$   |
| 6    | Approximately solve the LS- $\ell_1$ optimization on the support $I$<br>using the leading $\ell_1$ -DCD algorithm [116]   |
| 7    | Debiasing according to (4.27)   |
| 8    | Reweighting according to (4.28)   |

is added or removed from the support  $I$  based on the criteria given in Step 2 and 4 of Table 4.3 (see details in [115]). Then, the LS- $\ell_1$  optimization problem is approximately solved on the support by using the leading  $\ell_1$ -DCD algorithm [116]. The leading  $\ell_1$ -DCD algorithm used at Step 6 is summarized in Table 4.4, where the parameter  $\mu_c$  defines the stopping threshold  $T_c$ . The algorithm stops when the magnitude of the maximum residual element is smaller than  $T_c$ . The leading  $\ell_1$ -DCD algorithm operates in the same manner as the leading DCD algorithm, the only difference is in the cost function of the optimization problem.

After the leading  $\ell_1$ -DCD algorithm terminates, the support is re-estimated using the hard thresholding [113]:

$$I = \{k : |c_k| > \mu_d \max_k \{|c_k|\}\}, \quad (4.27)$$

where  $\mu_d$  is a predefined parameter between zero and one. Then, the weight vector is recursively updated as:

$$\tilde{\mathbf{w}}(i) = (1 - \mu_w) \tilde{\mathbf{w}}(i-1) + \mu_w \bar{\mathbf{w}}, \quad (4.28)$$

Table 4.4 Leading  $\ell_1$ -DCD algorithm

| Step | Input: $H, M_b, N_u, \mu_c, \mathbf{c}, \mathcal{R}, \mathbf{b}$<br>Initialization: $\delta = H, u = 0$         | Output: $\hat{\mathbf{c}}$ |
|------|---|----------------------------|
| 1    | $T_c = \mu_c \max_k  b_k $<br>for $m = 1, \dots, M_b$   |                            |
| 2    | $\delta = \delta/2, \boldsymbol{\alpha} = [\delta, -\delta, j\delta, -j\delta], \text{Flag} = 1$                |                            |
| 3    | While $u < N_u$ and Flag = 1, repeat:   |                            |
| 4    | $t = \operatorname{argmax}_{k \in I}  b_k $   |                            |
| 5    | if $ b_t  < T_c$ , break  |                            |
| 6    | for $k = 1, \dots, 4$ ,<br>$\Delta J(k) = -\Re\{\alpha_k^* b_t\} + \tau \tilde{w}_t ( c_t + \alpha_k  -  c_t )$ |                            |
| 7    | Find $J_{\min} = \min_k \Delta J(k)$ and $q = \operatorname{arg} \min_k \Delta J(k)$                            |                            |
| 8    | If $J_{\min} < -\frac{1}{2} \delta^2 \mathcal{R}_{t,t}$ , do:   |                            |
| 9    | $c_t = c_t + \alpha_q$  |                            |
| 10   | $\mathbf{b} = \mathbf{b} - \alpha_q \mathcal{R}^{(t)}$  |                            |
| 11   | $u = u + 1$   |                            |
| 12   | else, Flag = 0  |                            |
|      | end   |                            |

where  $\mu_w \in (0, 1]$  is a parameter which defines the update rate. Elements of the weight vector  $\bar{\mathbf{w}}$  are given by:

$$\bar{w}_k = \begin{cases} 0, & k \in I \\ 1, & \text{otherwise.} \end{cases}$$

## 4.4 Numerical results

In this section, we investigate by simulation the identification performance of the SRLS-L algorithm in time-varying channels; we compare it with the LBF estimator [104] and its fast version, the fLBF estimator [105]. In subsection 4.4.1, we describe the simulation scenario. In subsection 4.4.2, the identification performance of the algorithms is investigated. Finally, subsection 4.4.3 compares the complexity of the algorithms.

### 4.4.1 Simulation scenario

The simulation scenario is based on the channel information obtained in an FD lake experiment. Details of the lake experiment are given in Section 4.5. The SI channel impulse

response measured in the lake experiment is shown in Fig. 4.1. This is obtained using the third-order HSRLS-L-DCD adaptive filter which achieves in this experiment the best SIC performance among the adaptive algorithms that we considered. In this scenario, the SI to noise ratio is 71 dB. The symbol rate is  $f_d = 1$  kHz, thus the adaptive filter taps are separated by a 1 ms interval. The filter length is set to  $L = 80$ .

The channel is modelled as described in Section 1.4.2. The  $l$ th tap of the time-varying channel response  $h(i)$  is modelled as a stationary random process with a power spectral density  $G_h(2\pi f)$ , which is uniform within the frequency interval  $f \in [-f_{\max}, f_{\max}]$ , and independent of random processes describing the other taps. The variance of each multipath component is generated based on the power delay profile obtained using the channel estimates shown in Fig. 4.1. The power delay profile is shown in Fig. 4.2. It is the average power of each multipath component, which is computed based on the channel estimates obtained in the lake experiment.

It can be seen in Fig. 4.1 that the SI channel contains several strong taps, which are almost time-invariant; these are the direct path and reflections from stationary parts of the experimental equipment and lake bottom. The first fast time-varying tap is due to the reflection from the time-varying lake surface. Further taps are due to more complicated reflections (bottom-surface, surface-equipment, etc.), which include the surface reflection; thus, they are also fast varying. Therefore, it is sensible to use different cut-off frequencies  $f_{\max}^{(l)}$  of random processes describing time variation of different taps.

We identify the cut-off frequency of the  $l$ th tap based on the periodogram, which is computed as:

$$G_l(k) = \left| \sum_{n=0}^{N-1} \hat{h}_l(n) e^{-j2\pi kn/N} \right|^2, \quad k = 0, \dots, N-1, \quad (4.29)$$

where  $N$  is the number of samples of the  $l$ th tap over a time period (10 s in our experiment, see Fig. 4.1), and  $\hat{h}_l(n)$  is the estimate of the  $l$ th multipath component in the experiment. For the  $l$ th tap, we find the maximum index  $k_{\max}$  among  $k$  that satisfies,

$$G_l(k) > \eta \max_{k,l} G_l(k), \quad (4.30)$$

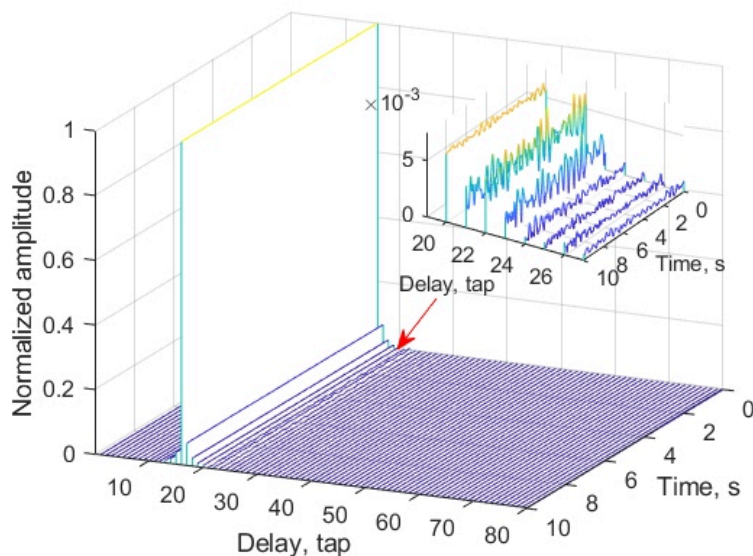


Fig. 4.1 Impulse response variation in the FD lake experiment. The lake surface is relatively calm during this experiment (see Fig. A.1 (b)). The lake depth is around 8 m. The distance between the transmitter (Tx) and receiver (Rx) is 7 cm. They are positioned at a depth of 4 m. It can be observed in the enlarged plot that the first few surface and bottom reflections are fast-varying.

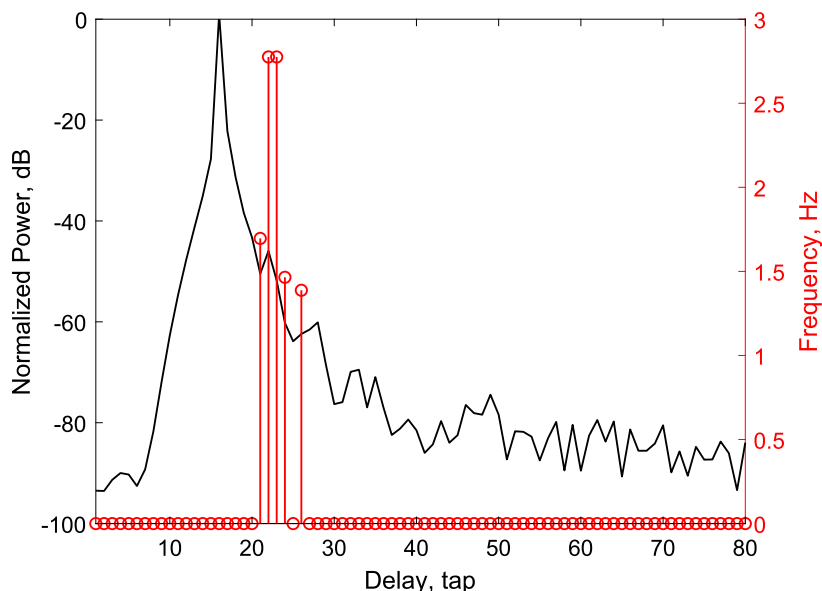


Fig. 4.2 Power delay profile (black curve) and cut-off frequency (red stem) of the multipath components in the FD lake experiment. The power of the multipaths are normalized with respect to the path with the maximum power. We plot the power delay profile and cut-off frequencies in the same figure to show the variance and speed of variation of the multipath components.

where  $\eta$  is a threshold parameter; we set  $\eta = -75$  dB. Then, we have the cut-off frequency of the  $l$ th multipath as  $f_{\max}^{(l)} = k_{\max} \Delta f$ , where  $\Delta f = f_d/N$ .

The cut-off frequencies  $f_{\max}^{(l)}$  of all multipath components are shown in Fig. 4.2. It can be seen that the first few taps around the direct path (at the 16th tap) have  $f_{\max} = 0$ , which means that these paths are almost time-invariant. Several taps associated with the first surface reflection are fast-varying with different variation speeds, and the maximum variation speed is close to 3 Hz. This is consistent with the time-varying channel estimates observed in Fig. 4.1.

#### 4.4.2 MSD performance

In this subsection, we investigate the identification performance of the classical SRLS, SRLS-L and HSRLS-L-DCD adaptive filters. The performance of the LBF [104] and fLBF estimators [105] are also investigated based on the MATLAB codes provided in [117] for comparison. Note that the MATLAB codes in [117] were converted into the complex-valued versions before using them in our simulations.

The normalized MSD ( $\text{MSD}(i)/\|\mathbf{h}(i)\|_2^2$ ) is used for evaluating the identification performance. It is averaged over an interval of 10 s after convergence.

The MSD performance of the adaptive filters from  $P = 0$  to  $P = 3$  are shown in Fig. 4.3. For each adaptive filter, we consider two cases, e.g., for the ‘SRLS-L’ adaptive filter, the uniform weighting is used, and for ‘SRLS-L, weighted’, a non-negative symmetric bell-shaped window (such as the Hanning window) is applied. The parameters of the adaptive filters are chosen to provide their best MSD performance. The optimal sliding window length  $M$  for every adaptive filter is shown in Table 4.5.

We first consider the adaptive algorithms without weighting (solid curves). As can be seen, an MSD performance of around  $-49$  dB is achieved by the classical SRLS algorithm. As expected, the SRLS-L adaptive filters achieve identical performance as that of the LBF estimator. On the other hand, the fLBF estimator shows an inferior performance, which does not change much over  $P$ . It is seen that the MSD performance can be significantly improved by using the SRLS-L adaptive filters. The higher order of polynomial  $P$  is, the better the

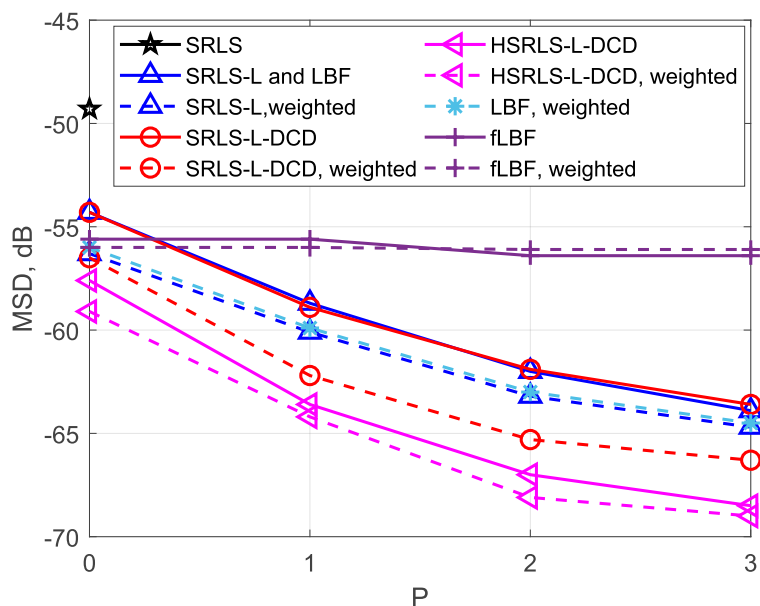


Fig. 4.3 MSD performance of the adaptive algorithms against the polynomial order ( $P$ ) in the simulation generated based on the lake experiment.

Table 4.5 Optimal  $M$  for the adaptive filters

| Adaptive filter                               | $M$ |
|---|-----|
| SRLS  | 105 |
| SRLS-L, SRLS-L-DCD and LBF, $P = 0$           | 145 |
| SRLS-L, SRLS-L-DCD and LBF, $P = 1$           | 185 |
| SRLS-L, SRLS-L-DCD and LBF, $P = 2$           | 305 |
| SRLS-L, SRLS-L-DCD and LBF, $P = 3$           | 385 |
| SRLS-L, SRLS-L-DCD and LBF, weighted, $P = 0$ | 185 |
| SRLS-L, SRLS-L-DCD and LBF, weighted, $P = 1$ | 205 |
| SRLS-L, SRLS-L-DCD and LBF, weighted, $P = 2$ | 325 |
| SRLS-L, SRLS-L-DCD and LBF, weighted, $P = 3$ | 405 |
| fLBF, $P = 0$ and $P = 1$                     | 165 |
| fLBF, $P = 2$ and $P = 3$                     | 385 |
| fLBF, weighted, $P = 0$ and $P = 1$           | 205 |
| fLBF, weighted, $P = 0$ and $P = 1$           | 545 |
| HSRLS-L-DCD, $P = 0$                          | 105 |
| HSRLS-L-DCD, $P = 1$                          | 105 |
| HSRLS-L-DCD, $P = 2$                          | 185 |
| HSRLS-L-DCD, $P = 3$                          | 265 |
| HSRLS-L-DCD, weighted, $P = 0$                | 125 |
| HSRLS-L-DCD, weighted, $P = 1$                | 125 |
| HSRLS-L-DCD, weighted, $P = 2$                | 265 |
| HSRLS-L-DCD, weighted, $P = 3$                | 345 |

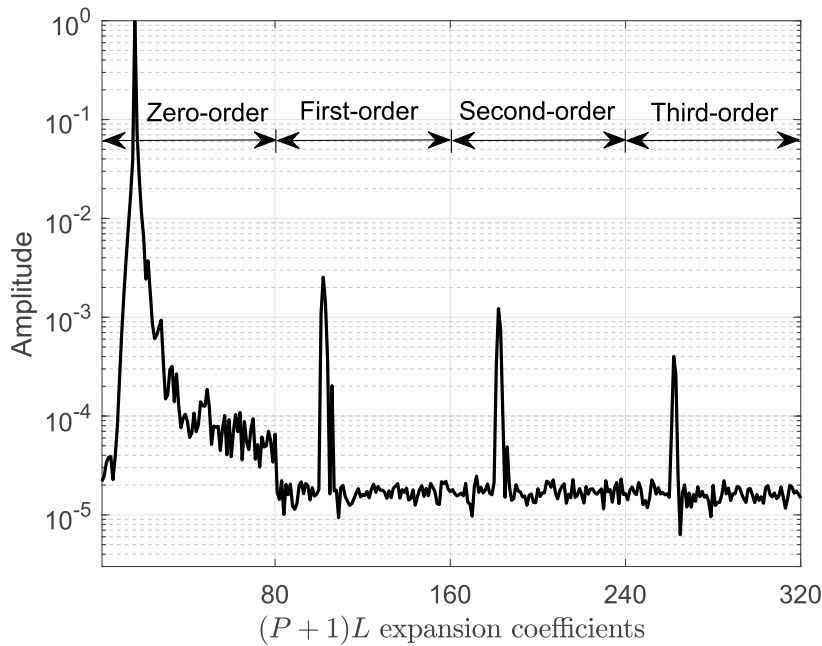


Fig. 4.4 Estimates of expansion coefficients when using the HSRLS-L-DCD algorithm.

MSD performance. The third-order SRLS-L adaptive filter outperforms the classical SRLS adaptive filter by 13.5 dB. Note that the fLBF estimator is no longer considered for SIC in FD lake experiments in this chapter due to its inferior performance.

It is obvious that the shorter time window  $M$  is used, the better the tracking performance can be achieved. However, for the identifiability,  $M$  should be longer than the number of estimated parameters, i.e., it should satisfy  $M > (P + 1)L$ . The number of parameters to be estimated is reduced if the channel is sparse. This in turn allows reducing the window length  $M$ . This can be done using the HSRLS-L-DCD algorithm.

In Fig. 4.4, we show estimates of the expansion coefficients obtained using the HSRLS-L-DCD algorithm. It can be seen that the expansion coefficients for the first-order, second-order and third-order basis functions exhibit a clear sparse structure. It contains several strong taps corresponding to the time-varying paths and the rest of them have magnitudes close to zero. Such a channel allows us to use a shorter estimation window as the number of non-zero elements required to be estimated is smaller.

Table 4.6 Parameters used for the HSRLS-L-DCD algorithm

|         | $\gamma$ | $\mu_d$              | $\mu_w$ |
|---------|----------|----------------------|---------|
| $P = 0$ | 0.85     | $1.5 \times 10^{-4}$ | 0.9     |
| $P = 1$ | 0.7      | $6 \times 10^{-4}$   | 0.8     |
| $P = 2$ | 0.75     | $4 \times 10^{-5}$   | 0.8     |
| $P = 3$ | 0.7      | $1 \times 10^{-5}$   | 0.85    |

Table 4.7 Parameters used for the adaptive filters with DCD iterations,  $H = 1$  and  $M_b = 24$ .

| Adaptive filter                | $N_u$ |
|--------------------------------|-------|
| SRLS-L-DCD, $P = 0$            | 12    |
| SRLS-L-DCD, $P = 1$            | 16    |
| SRLS-L-DCD, $P = 2$            | 64    |
| SRLS-L-DCD, $P = 3$            | 80    |
| SRLS-L-DCD, weighted, $P = 0$  | 4     |
| SRLS-L-DCD, weighted, $P = 1$  | 8     |
| SRLS-L-DCD, weighted, $P = 2$  | 8     |
| SRLS-L-DCD, weighted, $P = 3$  | 8     |
| HSRLS-L-DCD, $P = 0$           | 4     |
| HSRLS-L-DCD, $P = 1$           | 64    |
| HSRLS-L-DCD, $P = 2$           | 64    |
| HSRLS-L-DCD, $P = 3$           | 64    |
| HSRLS-L-DCD, weighted, $P = 0$ | 1     |
| HSRLS-L-DCD, weighted, $P = 1$ | 32    |
| HSRLS-L-DCD, weighted, $P = 2$ | 32    |
| HSRLS-L-DCD, weighted, $P = 3$ | 32    |

Detailed parameters used for the HSRLS-L-DCD algorithm are given in Table 4.6. As shown in Table 4.5, the optimal  $M$  for the HSRLS-L-DCD algorithms (from  $P = 1$  to  $P = 3$ ) are significantly reduced compared to the SRLS-L algorithms. Meanwhile, the MSD performance is further improved. With  $M = 265$ , the third-order HSRLS-L-DCD algorithm outperforms the classical SRLS algorithm by 19.1 dB.

Then, we consider the case when the bell-shaped weightings are applied to the basis functions (dashed line curves in Fig. 4.3). It is clear that the weighting improves the MSD performance for most of the adaptive algorithms, especially for non-sparse algorithms. The symmetric bell-shaped windowing helps to put emphasis on the data around the middle of the estimation time window. It can be seen from Table 4.5 that a slightly longer sliding window length is required for the weighted SRLS-L adaptive filters, which indicates that the overall

complexity of the weighted SRLS-L adaptive filters is slightly increased. However, as shown in Table 4.7, fewer DCD iterations are required for the weighted SRLS-L-DCD algorithm. Similar conclusions can be drawn for the HSRLS-L-DCD adaptive filters.

### 4.4.3 Complexity comparison

In this subsection, we compare the complexity of the SRLS-L, SRLS-L-DCD, and HSRLS-L-DCD adaptive filters at a time instant in terms of number of MACs, divisions and square-roots. We also compare them with the complexity of the LBF estimator which provides the same MSD performance as the SRLS-L adaptive filter.

The complexity analysis of the SRLS-L, SRLS-L-DCD and HSRLS-L-DCD algorithms is given in subsections 4.2.2 and Appendix D. Based on that, the overall complexities of the adaptive algorithms at every time instant are given in Table 4.8 with the optimal window lengths  $M$  in Table 4.5 and the filter length  $L = 80$ . We compute the complexity of the FFT operation of size  $(L + M)$  as  $(L + M) \log_2(L + M)$  MAC operations.

Combined with the simulation results shown in Fig. 4.3, several conclusions can be drawn from Table 4.8. First, the SRLS-L adaptive filters implemented using the proposed techniques achieve the same performance, but require only about one-fifth of the overall complexity compared to that of the LBF estimators. Further, the complexity of the SRLS-L adaptive filters is significantly reduced by using the DCD iterations, especially for higher-order SRLS-L-DCD algorithms; the overall complexity can be reduced by about hundreds of times. The complexity of the HSRLS-L-DCD algorithm is almost the same as that of the SRLS-L-DCD algorithm, however, the MSD performance is improved by an extra 2 to 3 dB when using the HSRLS-L-DCD algorithm.

Although by applying the Hanning window allows a reduction in the number of DCD iterations, at the same time, the required sliding window length  $M$  is increased, thus the overall complexity is about the same in all cases.

Table 4.8 Overall complexity of the adaptive filters per sample

|                                      | MACs              | $\div$ and $\sqrt{\quad}$ |
|--------------------------------------|-------------------|---------------------------|
| LBF (weighted), $P = 0$              | $9.6 \times 10^6$ |                           |
| LBF (weighted), $P = 1$              | $7.5 \times 10^7$ |                           |
| LBF (weighted), $P = 2$              | $2.5 \times 10^8$ |                           |
| LBF (weighted), $P = 3$              | $5.9 \times 10^8$ |                           |
| SRLS-L and SRLS-L, weighted, $P = 0$ | $2.1 \times 10^6$ |                           |
| SRLS-L and SRLS-L, weighted, $P = 1$ | $1.6 \times 10^7$ |                           |
| SRLS-L and SRLS-L, weighted, $P = 2$ | $5.5 \times 10^7$ |                           |
| SRLS-L and SRLS-L, weighted, $P = 3$ | $1.3 \times 10^8$ |                           |
| SRLS-L-DCD, $P = 0$                  | $3.7 \times 10^4$ |                           |
| SRLS-L-DCD, $P = 1$                  | $1.4 \times 10^5$ |                           |
| SRLS-L-DCD, $P = 2$                  | $3.7 \times 10^5$ |                           |
| SRLS-L-DCD, $P = 3$                  | $6.6 \times 10^5$ |                           |
| SRLS-L-DCD, weighted, $P = 0$        | $3.7 \times 10^4$ |                           |
| SRLS-L-DCD, weighted, $P = 1$        | $1.4 \times 10^5$ |                           |
| SRLS-L-DCD, weighted, $P = 2$        | $3.2 \times 10^5$ |                           |
| SRLS-L-DCD, weighted, $P = 3$        | $5.8 \times 10^5$ |                           |
| HSRLS-L-DCD, $P = 0$                 | $3.5 \times 10^4$ | 206                       |
| HSRLS-L-DCD, $P = 1$                 | $1.4 \times 10^5$ | 422                       |
| HSRLS-L-DCD, $P = 2$                 | $3.1 \times 10^5$ | 652                       |
| HSRLS-L-DCD, $P = 3$                 | $5.6 \times 10^5$ | 865                       |
| HSRLS-L-DCD, weighted, $P = 0$       | $3.5 \times 10^4$ | 216                       |
| HSRLS-L-DCD, weighted, $P = 1$       | $1.4 \times 10^5$ | 418                       |
| HSRLS-L-DCD, weighted, $P = 2$       | $3.2 \times 10^5$ | 643                       |
| HSRLS-L-DCD, weighted, $P = 3$       | $5.7 \times 10^5$ | 851                       |

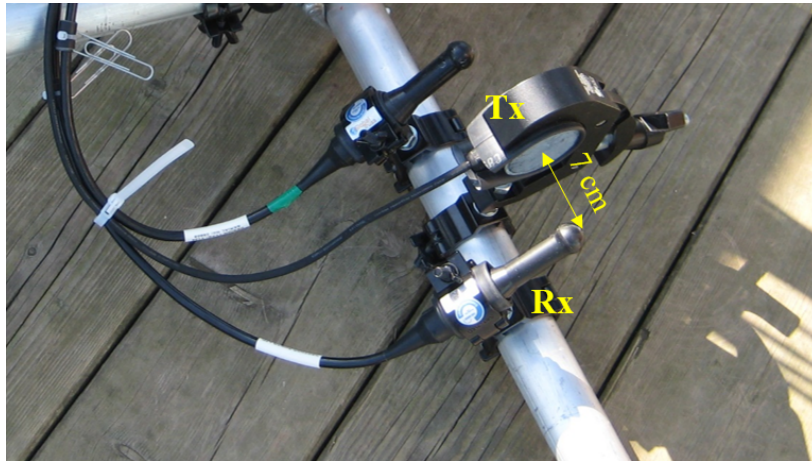


Fig. 4.5 Projector (Tx) and hydrophone (Rx) in the lake experiment.

## 4.5 Experimental results in lake experiments

In this section, the adaptive filters are used for the SI channel estimation with the scheme in Fig. 2.10 in the FD lake experiments. In the lake experiment, the true channel response is unknown, and therefore the MSD performance cannot be measured. Instead we measure the SICF for evaluating the cancellation performance.

### 4.5.1 Experimental setup and transmitted signals

The antenna configuration in the lake experiment is shown in Fig. 4.5. The distance between the transmitter (Tx) and receiver (Rx) is 7 cm. They are positioned at a depth of 4 m. The lake depth is around 8 m. During the experiment, the amplitude of the lake surface waves varies from 5 cm to 10 cm. A photo of the lake surface during the lake experiments is given in Fig. A.1 (b).

In the experiment, BPSK signals are transmitted; an RRC filter with a roll-off factor of 0.2 is used for the pulse shaping. The BPSK signals are transmitted at one of the three carrier frequencies  $f_c = 12, 32$  or 80 kHz with 1.2 kHz bandwidth. For the transmitted signal with 80 kHz carrier frequency, a wider frequency bandwidth of 4.8 kHz is also considered.

### 4.5.2 Experimental vs simulation results

We first consider the FD experiment at the carrier frequency 32 kHz. In this experiment, the SI to noise ratio is around 71 dB. The SICF is computed over a 10 s interval after the convergence of the adaptive filter. Table 4.9 shows the SICF and the optimal value of  $M$  providing the best cancellation for each of the adaptive algorithms. With  $P = 3$ , the SRLS-L algorithm improves the SICF by 8.5 dB compared to the classical SRLS algorithm. On top of that, the third-order HSRLS-L-DCD algorithm improves the SICF by an extra 3.7 dB, thus outperforming the classical SRLS algorithm by 12.2 dB. The SIC performance is slightly improved (around 1 dB) when weightings are applied for the SRLS-L algorithms. For the HSRLS-L-DCD algorithms, no noticeable difference is observed.

Table 4.9 SICF (in dB) in the lake experiment and in simulation (Sim),  $f_c = 32\text{kHz}$ ,  $f_d = 1\text{kHz}$ ;  $L = 80$ .

| Adaptive filter                | $M$ | SICF (Lake) | SICF (Sim) |
|--------------------------------|-----|-------------|------------|
| SRLS                           | 105 | 51.2        | 48.4       |
| SRLS-L, $P = 0$                | 185 | 55.5        | 52         |
| SRLS-L, $P = 1$                | 225 | 57.7        | 56         |
| SRLS-L, $P = 2$                | 325 | 58.9        | 59.5       |
| SRLS-L, $P = 3$                | 385 | 59.7        | 61.9       |
| SRLS-L, weighted, $P = 0$      | 225 | 56.7        | 53.5       |
| SRLS-L, weighted, $P = 1$      | 245 | 58.8        | 57.8       |
| SRLS-L, weighted, $P = 2$      | 385 | 60.1        | 61         |
| SRLS-L, weighted, $P = 3$      | 445 | 60.7        | 62.7       |
| HSRLS-L-DCD, $P = 0$           | 105 | 57.3        | 54.7       |
| HSRLS-L-DCD, $P = 1$           | 105 | 60.9        | 60.5       |
| HSRLS-L-DCD, $P = 2$           | 165 | 62.3        | 63.3       |
| HSRLS-L-DCD, $P = 3$           | 225 | 63.4        | 65.5       |
| HSRLS-L-DCD, weighted, $P = 0$ | 165 | 56.9        | 56         |
| HSRLS-L-DCD, weighted, $P = 1$ | 165 | 60.5        | 60.9       |
| HSRLS-L-DCD, weighted, $P = 2$ | 285 | 62.6        | 64.5       |
| HSRLS-L-DCD, weighted, $P = 3$ | 285 | 63.6        | 65.9       |

In Section 4.4, we considered a simulation scenario which is based on the SI channel estimates obtained in this experiment. To ensure a fair comparison, we use the same parameters for the adaptive filters in both the simulation and the lake experiment. We can see

Table 4.10 SICF in the lake experiment,  
 $f_c = 12\text{kHz}$ ,  $f_d = 1\text{kHz}$  and  $L = 100$ .

| Adaptive filter                | $M$ | SICF, dB |
|--------------------------------|-----|----------|
| SRLS                           | 145 | 43.4     |
| SRLS-L, $P = 0$                | 165 | 46.7     |
| SRLS-L, $P = 1$                | 225 | 49.6     |
| SRLS-L, $P = 2$                | 385 | 51.4     |
| SRLS-L, $P = 3$                | 525 | 52.1     |
| SRLS-L, weighted, $P = 0$      | 285 | 48.6     |
| SRLS-L, weighted, $P = 1$      | 285 | 50.8     |
| SRLS-L, weighted, $P = 2$      | 465 | 52.7     |
| SRLS-L, weighted, $P = 3$      | 545 | 53.1     |
| HSRLS-L-DCD, $P = 0$           | 165 | 49       |
| HSRLS-L-DCD, $P = 1$           | 165 | 52.7     |
| HSRLS-L-DCD, $P = 2$           | 265 | 55.3     |
| HSRLS-L-DCD, $P = 3$           | 285 | 56       |
| HSRLS-L-DCD, weighted, $P = 0$ | 225 | 50.1     |
| HSRLS-L-DCD, weighted, $P = 1$ | 225 | 52.7     |
| HSRLS-L-DCD, weighted, $P = 2$ | 325 | 55.7     |
| HSRLS-L-DCD, weighted, $P = 3$ | 345 | 56.3     |

that the SICFs in the simulation match very well to that in the experiment. This result further demonstrates that the channel modelling process we used in subsection 4.4.1 works well.

### 4.5.3 Experiments with different carrier frequencies and bandwidths

We now consider three experimental data sets with different carrier frequencies and bandwidths. This is done to investigate how consistent is the improvement in the SIC performance achieved with the proposed adaptive filters in practical scenarios. The experimental results are shown in Tables 4.10 and 4.11.

In the first experiment, the BPSK signal is transmitted at the carrier frequency  $f_c = 12\text{ kHz}$  at the symbol rate  $f_d = 1\text{ kHz}$ . The SI to noise ratio is around 65 dB. In this experiment, the channel delay spread is longer compared to the  $f_c = 32\text{ kHz}$  channel. Therefore, we use a filter length of  $L = 100$ . The parameters of the algorithms are chosen to provide the best SIC performance. It can be seen in Table 4.10 that the SICF can be improved by using higher order basis functions. With  $P = 3$ , the SRLS-L algorithm outperforms

Table 4.11 SIC factor (in dB) in the lake experiment,  $f_c = 80\text{kHz}$ .

| Adaptive filter           | $f_d = 1\text{kHz}, L = 60$ |            | $f_d = 4\text{kHz}, L = 240$ |            |
|---------------------------|-----------------------------|------------|------------------------------|------------|
|                           | $M$                         | SIC factor | $M$                          | SIC factor |
| SRLS                      | 85                          | 47.1       | 505                          | 47.4       |
| SRLS-L, $P = 0$           | 135                         | 49.9       | 465                          | 49.7       |
| SRLS-L, $P = 1$           | 165                         | 49.6       | 685                          | 50.6       |
| SRLS-L, $P = 2$           | 265                         | 50.6       | 965                          | 50.4       |
| SRLS-L, $P = 3$           | 345                         | 50.4       | 1325                         | 50.8       |
| SRLS-L, weighted, $P = 0$ | 185                         | 50.8       | 685                          | 50.8       |
| SRLS-L, weighted, $P = 1$ | 205                         | 51.3       | 805                          | 51.6       |
| SRLS-L, weighted, $P = 2$ | 325                         | 51.3       | 1205                         | 51.4       |
| SRLS-L, weighted, $P = 3$ | 345                         | 51.4       | 1385                         | 51.6       |
| HSRLS-L-DCD, $P = 0$      | 65                          | 52.4       | 265                          | 52.7       |
| HSRLS-L-DCD, $P = 1$      | 65                          | 54         | 265                          | 55.7       |
| HSRLS-L-DCD, $P = 2$      | 105                         | 55.8       | 425                          | 57         |
| HSRLS-L-DCD, $P = 3$      | 115                         | 56.5       | 445                          | 57.4       |

the classical SRLS algorithm by 8.7 dB. Additional 3.9 dB of SIC is achieved with the third-order HSRLS-L-DCD algorithm by exploiting the sparsity in the expansion coefficients. Again, the SIC performance is slightly improved by applying weightings when using the SRLS-L adaptive algorithm. However, the improvement in the performance of the HSRLS-L-DCD algorithm, especially for the higher-order cases, is almost negligible (within 0.5 dB). Therefore, we only apply weighting to the SRLS-L adaptive filter for the rest of the data.

In Tables 4.11, we show the SIC performance of the 80 kHz signal with 1 kHz and 4 kHz frequency bandwidth. The SI to noise ratio in both experiments is around 65 dB. Due to the high attenuation at higher frequencies, the SI channel delay spread is reduced. The adaptive filter length is  $L = 60$  for the signal with 1 kHz bandwidth, and  $L = 240$  for the 4 kHz bandwidth.

The SIC performance in both cases is very close. The SICF is slightly better with the 4 kHz bandwidth. This could be attributed to the clearer multipath structure due to the higher delay resolution. Another observation is that the optimal estimation time window length for the HSRLS-L-DCD algorithms is much smaller compared to the SRLS-L algorithm. With  $P = 3$ , the estimation time window of the HSRLS-L-DCD algorithm is about twice

shorter compared to that of the SRLS-L algorithm. This explains the improvement in the SIC performance.

## 4.6 Conclusions

In this chapter, low complexity interpolating adaptive filters which combine the SRLS adaptive filter and BEM approach (specifically, the Legendre polynomials) are proposed for identification of time-varying channels. Techniques are proposed to reduce the complexity of the adaptive filters using the FFT and DCD algorithms. To exploit the sparsity in the expansion coefficients, a novel sparse adaptive filter, the HSRLS-L-DCD algorithm is proposed. The MSD performance of the proposed adaptive filters is investigated and compared with that of the LBF estimator in a simulation which mimics an FD lake experiment. Complexity analysis is presented for all the algorithms used in the simulation. FD lake experiments are conducted to evaluate the SIC performance of the proposed adaptive filters. Results show that the proposed adaptive filtering algorithms significantly improve the SIC performance compared to classical RLS algorithm. Moreover, the proposed algorithms are of comparatively low complexity, and due to the use of DCD iterations, are well suited to hardware (such as FPGA) implementation, which makes them good candidates for practical implementation.



# Chapter 5

## Self-Interference Cancellation with Multiple Transducers

This chapter describes two SIC schemes with multiple projectors or hydrophones in FD UWA systems. In Section 5.1, we propose an SIC scheme with two projectors which cancels the SI in the acoustic domain. In Section 5.2, a two-stage SIC scheme with two hydrophones is proposed to deal with the time-varying surface reflections. In Section 5.3, conclusions are drawn.

The work in this chapter is presented in the papers: Y. Wang, Y. Li, L. Shen, and Y. Zakharov, “Acoustic-domain self-interference cancellation for full-duplex underwater acoustic communication systems,” in *IEEE Asia-Pacific Signal and Information Processing Association Annual Summit and Conference*, 2019, pp. 1112–1116; L. Shen, B. Henson, Y. V. Zakharov, and P. Mitchell, “Two-stage self-interference cancellation in full-duplex underwater acoustic systems,” in *MTS/IEEE Oceans - Marseille*, 2019, pp. 1–6.

### 5.1 Acoustic-domain SIC with two projectors

In terrestrial radio communication systems, SIC can be done in the radio domain using three antennas [23, 26, 118, 119]. The key idea is to separate two transmit antennas from the receiver antenna with distances of  $d$  and  $d + \lambda/2$ , where  $\lambda$  is a wavelength at the operating

frequency, so that the signals from the two transmit antennas cancel each other at the receive antenna. However, in UWA systems, due to the wide bandwidth of communication signals and multipath propagation, such a scheme cannot achieve a good cancellation performance.

In this section, we propose a scheme for adaptive SIC of wideband signals in the acoustic domain by using two projectors and one hydrophone. The performance of the proposed scheme is investigated by numerical simulation. The simulation results show that the proposed scheme can reduce the SI to the noise level in time-invariant scenarios.

### 5.1.1 FD system structure with two projectors

The FD UWA system with the proposed acoustic SIC scheme is shown in Fig. 5.1. The system operates at two different sampling rates. The high sampling rate is used for signal reception, while the adaptive filters work at the low sampling rate. The transmitted symbols  $a(i)$  are pulse-shaped by an RRC filter and then up-sampled to the sampling rate  $f_s$  and up-shifted to the carrier frequency  $f_c$  as illustrated in Fig. 5.2.

The FD system contains two projectors. The first projector is used to transmit the data  $a(i)$  intended for the far-end user. The SI signal  $r_1(t)$  received at the hydrophone is from the first projector. The second projector emits a signal to produce the acoustic signal  $r_2(t)$  at the hydrophone that cancels  $r_1(t)$  from the first projector. The primary and secondary acoustic channels are denoted as  $\mathbf{h}_1$  and  $\mathbf{h}_2$ , respectively; both  $\mathbf{h}_1$  and  $\mathbf{h}_2$  are unknown. The weight vector  $\hat{\mathbf{w}}_1(i)$  is adapted in such a way that the transmitted data  $a(i)$  after passing through the filter  $\hat{\mathbf{w}}_1(i)$  and the secondary channel  $\mathbf{h}_2$  form a signal  $r_2(t)$  that cancels  $r_1(t)$  from the primary path. The delay  $\tau$  in the transmit chain is introduced to compensate for the delay in the adaptive filter  $\hat{\mathbf{w}}_1(i)$ . At the receiver, the passband received signal  $x_1(t)$  is analogue-to-digital converted and transformed into the baseband equivalent signal  $e_1(i)$  after front-end processing (see Fig. 2.2).

Since the main focus here is to investigate the performance of the acoustic SIC scheme, we assume that there is no quantization errors introduced by the DAC in the simulations.

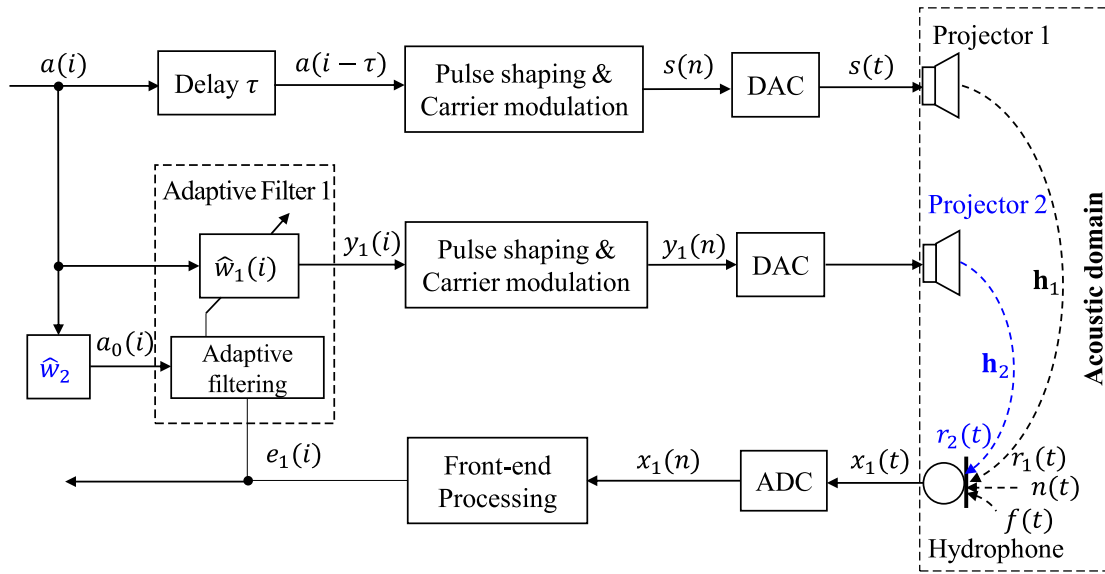


Fig. 5.1 Block diagram of acoustic SIC for FD UWA system. Index  $n$  is used for samples at the high sampling rate  $f_s$  and index  $i$  is used for samples at the lower sampling rate  $f_d$ . The first projector is used for data transmission, and the second projector is used to emit a cancellation signal.

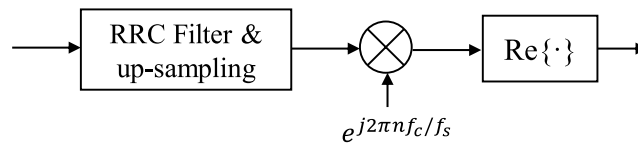


Fig. 5.2 Pulse shaping and carrier modulation.

### 5.1.2 Acoustic SIC scheme

In the previous chapters, the adaptation and the SIC are both performed in the digital domain by an adaptive filter. In this scheme, the cancellation is done in the acoustic domain, whereas the adaptation is done in the digital domain.

Note that the signal  $a_0(i)$  is used as the regressor in the adaptive filter instead of the original data  $a(i)$ . It is found that the performance can be significantly improved if the regressor is generated by pre-filtering the data  $a(i)$  in a filter with the baseband estimate of the secondary path  $h_2$ . Therefore, the proposed acoustic cancellation scheme operates in two steps. In the first step, the secondary path is estimated, thus producing the weight vector  $\hat{w}_2$ . In the second step, the adaptive filter updates the weight vector  $\hat{w}_1(i)$ , while

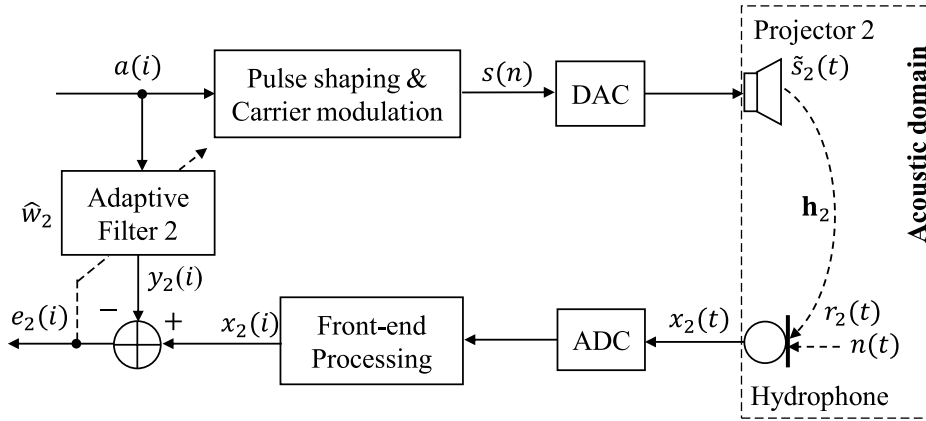


Fig. 5.3 Estimation of the secondary path  $\mathbf{h}_2$ .

the system simultaneously transmits near-end signal and receives the far-end signal with a ‘frozen’ weight vector  $\hat{\mathbf{w}}_2$  obtained at the first step after convergence.

At the first step, the adaptive filter 2 is used as shown in Fig. 5.3. The ERLS-DCD algorithm is used for the estimation of the secondary path. The secondary path is estimated when the first projector is not transmitting data. After the convergence of the adaptive filter, we obtain the weight vector  $\hat{\mathbf{w}}_2$  as a baseband estimate of  $\mathbf{h}_2$ . The adaptive filter length  $L_2$  is long enough to cover the length of the channel impulse response  $\mathbf{h}_2$  and the length of a pair of RRC filters.

The adaptation in the adaptive filter 1 in Fig. 5.1 is based on the error signal that is originally generated in the acoustic domain. Note that, in the classical form, the ERLS algorithm computes the error signal as a difference between the desired signal and the adaptive filter output in the digital domain [59]. In our case, the error signal is generated in the acoustic domain at the hydrophone. Therefore, we use another form of the ERLS algorithm as presented in Table 5.1, where  $\lambda_1$  is the forgetting factor of adaptive filter 1,  $L_1$  is the adaptive filter length,  $\epsilon$  is a regularization parameter,  $\mathbf{\Pi}$  is an  $L_1 \times L_1$  identity matrix and  $\mathbf{R}$  is an  $L_1 \times L_1$  autocorrelation matrix of the input signal. The  $i$ th sample of the regressor  $a_0(i)$  is computed by pre-filtering the vector of the transmitted data  $\mathbf{a}(i) = [a(i), \dots, a(i+L_2-1)]$  with the estimate of the secondary path  $\hat{\mathbf{w}}_2$ . Instead of the direct approach, Step 3 in Table 5.1 is implemented by solving the system of equations with a few DCD iterations.

Table 5.1 The modified RLS algorithm for acoustic SIC

| Step   | Equation  |
|--|---|
| Initialization: $\hat{\mathbf{w}}_1(0) = \mathbf{0}$ , $\mathbf{R}(0) = \epsilon \mathbf{\Pi}$ |   |
| for $n = 1, 2, \dots$  |   |
| 1  | $a_0(i) = \hat{\mathbf{w}}_2^H \mathbf{a}(i)$                                   |
| 2  | $\mathbf{R}(i) = \lambda_1 \mathbf{R}(i-1) + \mathbf{a}_0(i) \mathbf{a}_0^H(i)$ |
| 3  | $\mathbf{R}(i) \Delta \hat{\mathbf{w}}(i) = \mathbf{a}_0(i) e_1^*(i)$           |
| 4  | $\hat{\mathbf{w}}_1(i) = \hat{\mathbf{w}}_1(i-1) + \Delta \hat{\mathbf{w}}(i)$  |

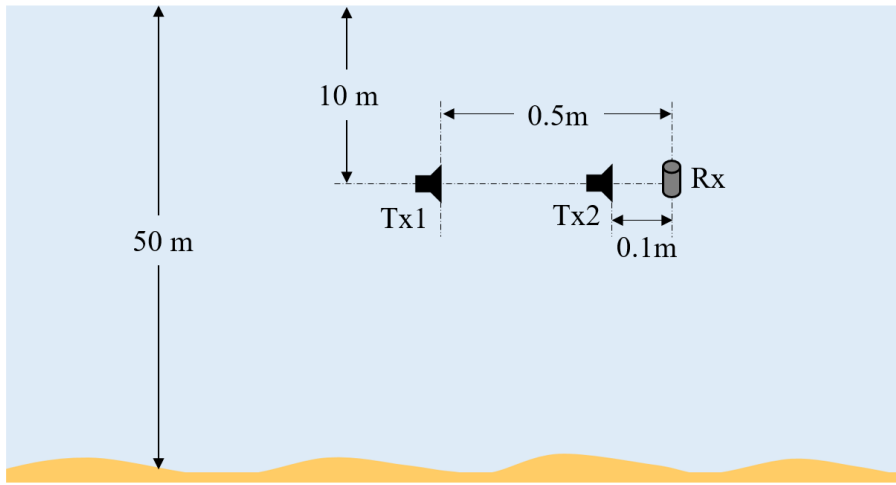


Fig. 5.4 Configuration of the simulation scenario (Tx1: primary projector; Tx2: secondary projector; Rx: hydrophone).

### 5.1.3 Simulation results

In this subsection, we investigate the acoustic SIC performance with Waymark simulation data. We consider a simulation scenario in a shallow sea of depth 50 m with a constant sound speed profile of 1500 m/s and flat sea surface. The configuration of the simulation scenario is shown in Fig. 5.4. The hydrophone and projectors are positioned at a depth of 10 m. The primary projector is 0.5 m away from the hydrophone, and the secondary projector is 0.1 m away from the hydrophone.

We use the single-carrier communication signal with quadrature phase-shift keying (QPSK) modulation. The signal length of the transmitted and received signals are 150 s.

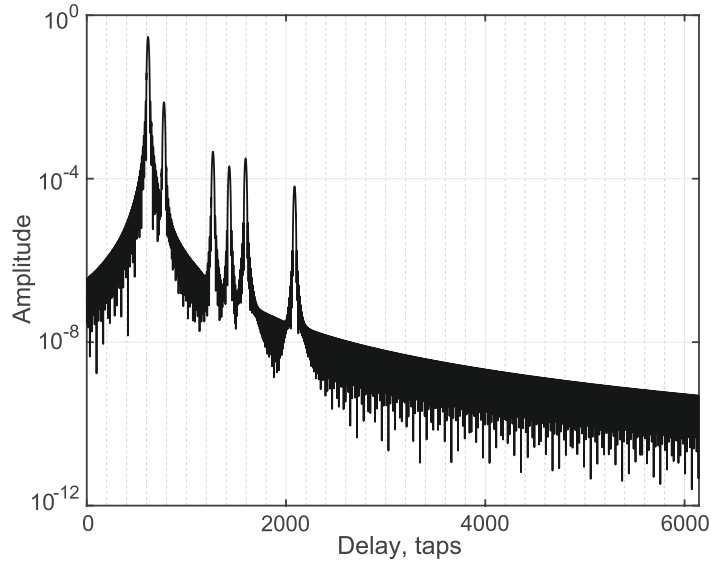


Fig. 5.5 Amplitude of the impulse response of the primary path ( $\mathbf{h}_1$ ).

The far-end channel is modelled as a single path channel. The carrier frequency is set to  $f_c = 3072$  Hz, and the frequency bandwidth is  $B = 1024$  Hz. The symbol rate is 1024 Hz, and the high sampling rate is  $f_s = 4f_c = 12288$  Hz. The roll-off factor of the RRC filter is  $\alpha = 0.2$  and the filter length is 12 symbols duration.

The passband Waymark UWA simulator [70] is used to generate the hydrophone outputs  $r_1(i)$  and  $r_2(i)$  from the primary and the secondary projectors. The impulse responses of the primary and secondary path are shown in Fig. 5.5 and Fig. 5.6, respectively. As the impulse response is generated in the passband, the delay of one tap is  $T_s = 1/f_s$  s.

The noise signal is added to the received signal to make the SI to noise ratio  $\text{SNR}_{\text{SI}}$  between the SI signal  $r_1$  and the noise equal to 100 dB; it is defined as:

$$\text{SNR}_{\text{SI}} = \frac{P_{r_1}}{\eta \cdot \sigma_n^2},$$

where  $P_{r_1}$  is the average power of the SI signal,  $\sigma_n^2$  is the noise variance. The coefficient  $\eta = 2B/f_s$  is applied to take into account the limited bandwidth of the SI signal.

For the secondary path, the SI estimation performance is assessed by the NMSE as defined in (2.1). For the primary path, the MSE is normalized with respect to the SI signal

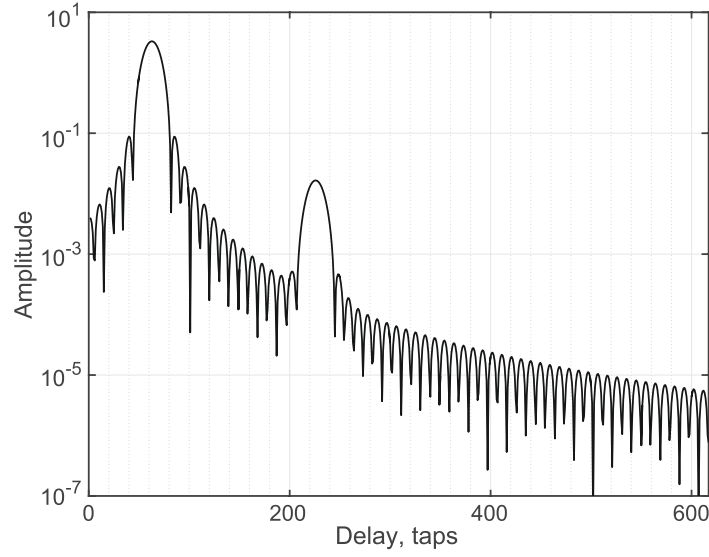


Fig. 5.6 Amplitude of the impulse response of the secondary path ( $\mathbf{h}_2$ ).

generated by the primary projector, which is computed as:

$$\text{NMSE}(i) = \frac{P_{e_1}(i)}{P_{r_1}}, \quad (5.1)$$

where  $P_{e_1}(i) = |e_1(i)|^2$  is the instantaneous power of the error signal  $e_1(n)$ , and  $P_{r_1}$  is the average power of the SI signal  $r_1$ .

Apart from the NMSE, we also compute the SIC performance as:

$$\text{SI cancellation} = \frac{P_{r_1}}{P_{\text{Residual}}}, \quad (5.2)$$

where  $P_{r_1}$  is the average power of the primary SI signal before SIC,  $P_{\text{Residual}}$  is the average power of the residual signal  $\varepsilon(i) = e_1(i) - n(i) - f(i)$  after the convergence of the first adaptive filter, where  $n(i)$  and  $f(i)$  represents the baseband equivalent noise and far-end signal, respectively. Note that (5.2) is only applicable when predictive adaptive filters are used.

The far-end SNR is defined as:

$$\text{SNR}_{\text{far}} = \frac{\sigma_f^2}{\eta \sigma_n^2}, \quad (5.3)$$

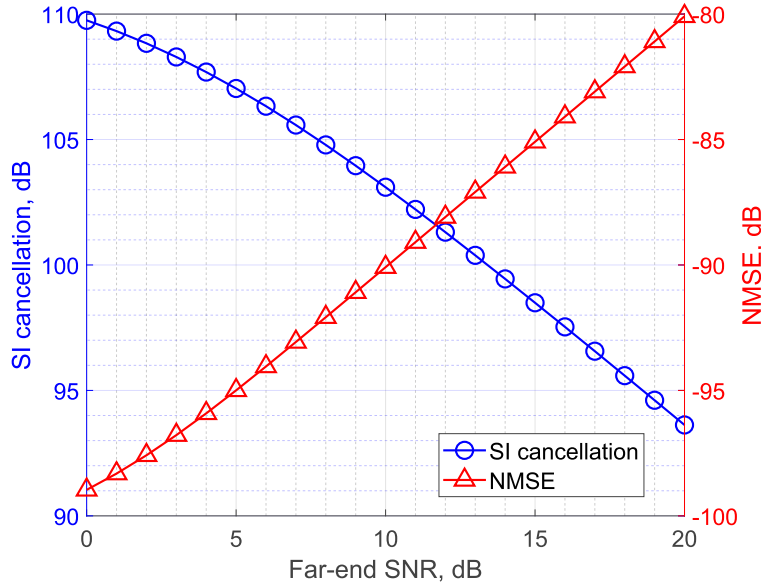


Fig. 5.7 NMSE and SIC performance of the FD UWA system against the far-end SNR. The interference level increases with the far-end SNR. This explains the degradation in SIC and the increase in MSE at high far-end SNR.

where  $\sigma_f^2$  and  $\sigma_n^2$  represent the variance of the far-end signal and the noise, respectively. The system output  $e_1(i)$  after acoustic SIC is treated as an estimate of the far-end baseband signal  $f(i)$  when computing the detection performance.

Fig. 5.7 shows the NMSE and SIC performance. The weight vectors  $\hat{w}_1$  and  $\hat{w}_2$  (of adaptive filters 1 and 2) are of lengths  $L_1 = 150$  and  $L_2 = 55$ , respectively. It can be seen that the NMSE increases with the far-end SNR. This happens because the far-end signal introduces an extra interference to the SI canceller and the interference level increases when the far-end signal level increases. However, the proposed scheme provides the SIC higher than 100 dB when the far-end SNR is smaller than 13 dB. This indicates that the residual SI is below the noise level after SIC, thus the detection performance should not degrade much compared to the case without the SI.

Fig. 5.8 shows the BER performance of the proposed scheme for two cases. In Case 1, during adjustment of  $\hat{w}_1$ , the far-end signal is present as discussed above. In Case 2, the adaptation is performed without the far-end signal. It is expected that the performance should be improved in the second case. This is verified by the results shown in Fig. 5.8. The presence of the far-end signal does degrade the detection performance; e.g., when the far-end SNR is

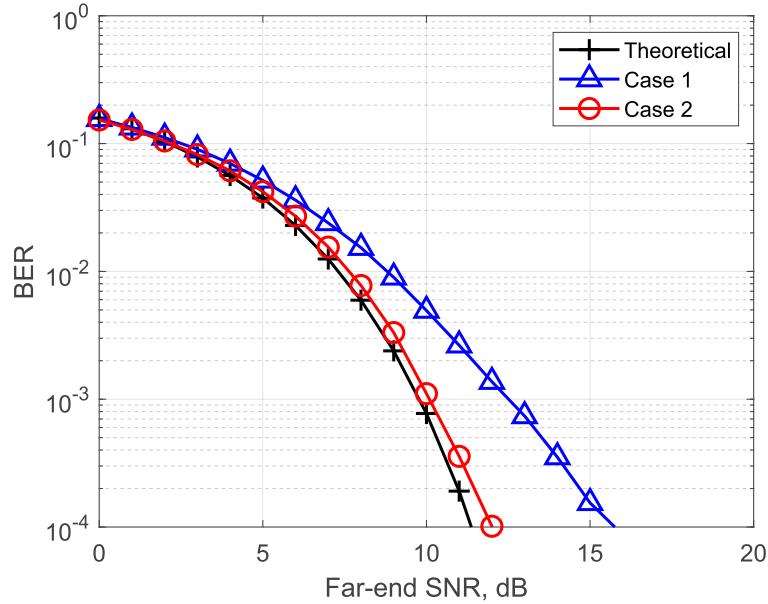


Fig. 5.8 BER performance of the FD UWA system with different levels of far-end SNR.

15 dB, the loss is about 3.5 dB. However, the QPSK transmission in our simulation does not use any coding. The detection performance can be improved by applying error-correcting codes to the transmitted data, which would allow the receiver to detect and correct a certain amount of errors [22].

As demonstrated by the simulation results, the proposed acoustic-domain SIC scheme can achieve the cancellation performance high enough for a reliable communication using the single-carrier transmission with QPSK symbols. It is believed that a joint acoustic-digital cancellation scheme has the potential to achieve a high level of SIC in FD UWA systems.

## 5.2 Digital SIC with two hydrophones

For time-invariant UWA channels, the SI can be efficiently cancelled using an adaptive filter [1]. However, apart from the direct (strong and stable) SI path between the projector and hydrophone, there are multiple SI paths, including those reflected from the moving sea surface. In Chapter 3 and 4, interpolating adaptive filters are proposed to estimate the fast time-varying channels. In this section, we propose another approach for cancelling the fast-varying reflections and propose a two-stage SIC scheme with two hydrophones.

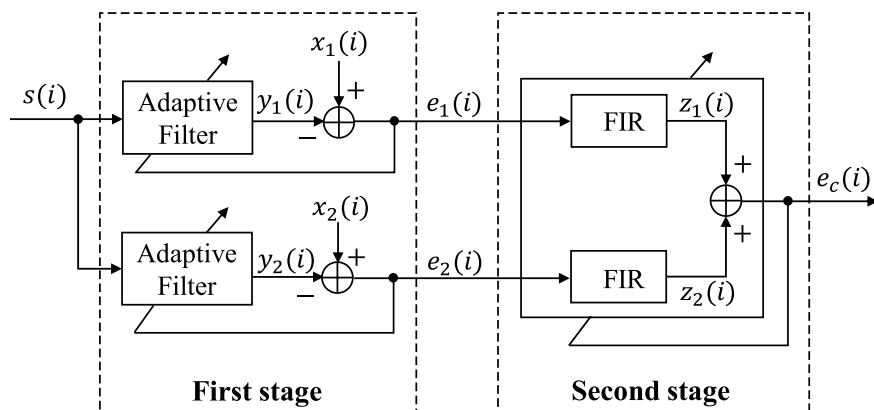


Fig. 5.9 Block diagram of the two-stage SIC scheme;  $s(i)$  is the PA output,  $x_1(i)$  and  $x_2(i)$  are the baseband received signals at the first and second hydrophones, respectively;  $e_1(i)$  and  $e_2(i)$  are the residual signals at the first and second hydrophones and  $e_c(i)$  is the combined signal after adaptive beamforming.

At the first stage, the direct path SI is cancelled at each of the hydrophone outputs. The second stage plays the role of an adaptive beamformer that tries to cancel the residual SI, particularly the SI due to reflections from the sea surface. The cancellation performance of the proposed scheme is investigated using the Waymark UWA channel simulator [68] and in the water tank and lake experiments.

### 5.2.1 Two-stage SIC scheme

The block diagram of the two-stage SIC scheme is shown in Fig. 5.9. At the first stage, the digital canceller proposed in Chapter 2 is applied to each hydrophone output. The task of the digital canceller is to subtract the SI from the received signal, which is computed based on the SI channel estimates obtained from the adaptive filter. In Chapter 2, we show that the SIC performance can be significantly improved by using the PA output as the regressor instead of the original digital data. Therefore, we use the baseband PA output as the regressor  $s(i)$ , and use the received signals ( $x_1(i)$ ,  $x_2(i)$ ) from the two hydrophones as desired signals of the adaptive filters in the digital SI cancellers. The ERLS-DCD adaptive filter is used for SI channel estimation due to its fast convergence, low-complexity and numerical stability [86, 87].

Table 5.2 The modified ERLS algorithm for the beamformer

| Step | Equation  |
|------|---|
|      | Initialization: $\mathbf{e}_1(0) = \mathbf{0}$ , $\mathbf{e}_2(0) = \mathbf{0}$ , $\mathbf{R}(0) = \epsilon \mathbf{\Pi}$ , $\hat{\mathbf{h}}(0) = \mathbf{0}$<br>for $i = 1, \dots, N$ |
| 1    | Update $\mathbf{e}_1(i)$ , $\mathbf{e}_2(i)$  |
| 2    | $\mathbf{r}(i) = [\mathbf{e}_1(i); \mathbf{e}_2(i)]^T$  |
| 3    | $\mathbf{R}(i) = \lambda \mathbf{R}(i-1) + \mathbf{r}(i) \mathbf{r}^H(i)$   |
| 4    | $e_c(i) = -\hat{\mathbf{h}}^H(i) \mathbf{r}(i)$   |
| 5    | $\mathbf{p}(i) = e_c^*(i) \mathbf{r}(i)$  |
| 6    | Solve $\mathbf{R}(i) \Delta \mathbf{h}(i) = \mathbf{p}(i) \Rightarrow \Delta \hat{\mathbf{h}}(i)$   |
| 7    | $\hat{\mathbf{h}}(i) = \hat{\mathbf{h}}(i-1) + \Delta \hat{\mathbf{h}}(i)$  |
| 8    | $\hat{\mathbf{h}}(i) = \hat{\mathbf{h}}(i) / \ \hat{\mathbf{h}}(i)\ $   |
|      | end   |

At the second stage, the main task is to further cancel the residual SI components. Here we use a modified ERLS adaptive filter for adaptive beamforming. The regressor of the beamformer consists of residual signal samples on the two branches (hydrophones)  $\mathbf{e}_1(i)$  and  $\mathbf{e}_2(i)$ . The desired signal is assumed to be equal to zero. The adaptive algorithm jointly updates weights of two FIR filters to minimize the combined error signal  $e_c(i)$  at the filter output. The weight coefficients of the adaptive filter are defined as:  $\hat{\mathbf{h}}(i) = [\hat{\mathbf{h}}_1(i); \hat{\mathbf{h}}_2(i)]^T$ , where  $\hat{\mathbf{h}}_1(i) = [\hat{h}_1(i), \dots, \hat{h}_1(i - L_2/2 + 1)]^T$  and  $\hat{\mathbf{h}}_2(i) = [\hat{h}_2(i), \dots, \hat{h}_2(i - L_2/2 + 1)]^T$  are the weight vectors of the two FIR filters,  $L_2$  is the length of the adaptive filter in the second stage. The weight coefficients  $\hat{\mathbf{h}}(i)$  are constrained to have a norm equal to one to avoid undesired situation when all filter coefficients are updated to zero. The modified ERLS algorithm is summarized in Table. 5.2, where  $\epsilon$  is the regularization parameter,  $\lambda_2$  is the forgetting factor at the second stage,  $\mathbf{e}_1(i) = [e_1(i), \dots, e_1(i - L_2/2 + 1)]^T$  and  $\mathbf{e}_2(i) = [e_2(i), \dots, e_2(i - L_2/2 + 1)]^T$  are the inputs of the FIR filters,  $\mathbf{r}(i)$  is an  $L_2 \times 1$  regressor of the beamformer and  $\|\hat{\mathbf{h}}(i)\|$  is the Euclidean norm of the weight vector  $\hat{\mathbf{h}}(i)$ . The system of equations at Step 6 is solved by using DCD iterations.

### 5.2.2 Simulation results

To investigate the cancellation performance of the proposed SIC scheme, we use the Waymark UWA channel simulator described in 1.4.2. We transmit BPSK signals at a carrier frequency of 12 kHz with 1.2 kHz bandwidth. The sampling frequency is  $f_s = 96$  kHz. The length of the transmitted signal is 10 s. The Waymark model provides passband samples of the noise-free SI channel output. The noise signal is generated by adding independent Gaussian noise to the Waymark output according to a predefined SI to noise ratio. In this scenario, the SI to noise ratio is set as 100 dB.

The cancellation performance is evaluated by residual SI level at the steady-state. For the first stage, we denote the steady-state residual SI level at the  $k$ th branch ( $k = 1, 2$ ) as  $R_{\text{SI},k}$ , which is computed as:

$$R_{\text{SI},k} = \frac{P_{e,k}}{\sigma_{n,k}^2} = \frac{\mathbf{e}_k^H \mathbf{e}_k}{N_s \sigma_{n,k}^2}, \quad (5.4)$$

where  $P_{e,k}$  is the average power of the error  $\mathbf{e}_k = [e(N - N_s + 1), \dots, e(N)]^T$  at the  $k$ th branch,  $N$  is the number of samples in the received signal,  $N_s = 1000$  is the number of samples used for computing the residual SI level,  $\sigma_{n,k}^2$  is the noise variance of the  $k$ th branch.

For the second stage, we compute the residual SI level  $R_{\text{SI},c}$  at the adaptive beamformer output as:

$$R_{\text{SI},c} = \frac{P_{e,c}}{\sigma_{n,c}^2} = \frac{\mathbf{e}_c^H \mathbf{e}_c}{N_s \sigma_{n,c}^2}, \quad (5.5)$$

where  $P_{e,c}$  is the average power of the combined error  $\mathbf{e}_c = [e_c(N - N_s + 1), \dots, e_c(N)]^T$ ,  $\sigma_{n,c}^2$  is the noise variance of the combined noise. The combined noise at each time instant is calculated as:  $n_c(i) = \hat{\mathbf{h}}(i)^H \mathbf{n}(i)$ , where  $\mathbf{n}(i) = [n_1(i), \dots, n_1(i + L_2/2 - 1), n_2(i), \dots, n_2(i + L_2/2 - 1)]^T$ ,  $n_1(i)$  and  $n_2(i)$  are the noise samples from two hydrophones, respectively.

#### Scenario 1

We first consider a static environment with fixed projector and hydrophone positions, with a constant sound speed profile of 1500 m/s and a flat sea surface. The sea depth is 150 m,

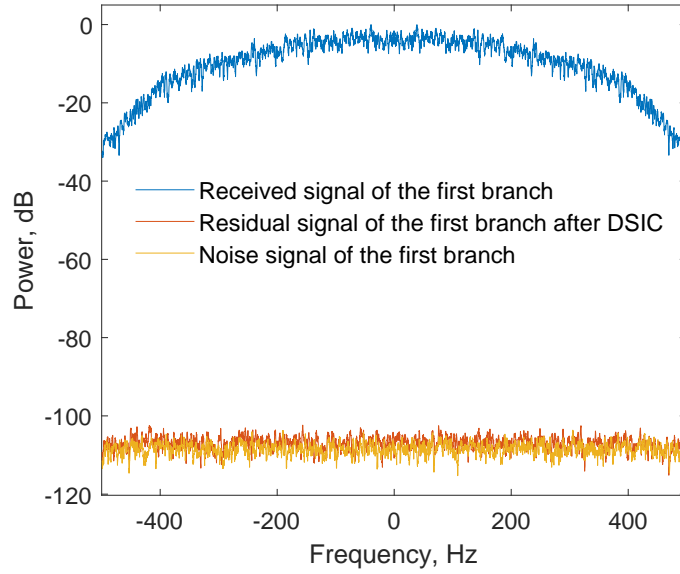


Fig. 5.10 Power spectra of the signals at a single hydrophone in the static environment produced by the Waymark simulator. The power spectral densities are normalized with respect to the maximum of the power spectral density of the received signal. Received signal of the first branch refers to  $x_1(i)$  in Fig. 5.9.

a projector and a single hydrophone are placed 0.3 m apart at a depth of 50 m. As shown in Fig. 5.10, the SI can be perfectly cancelled to the noise level using only the first stage of digital SIC. In this scenario, the second stage of cancellation is not required.

### Scenario 2

For the second scenario, we generate sea surface waves with a period of 15 s, an amplitude of 0.1 m and a space wavelength of 100 m. As shown in Fig. 5.11, the projector is placed at 50 m depth, and two hydrophones are placed at 49.85 m and 50.15 m depth, respectively. The horizontal distance between the projector and hydrophones is 0.3 m.

For digital cancellation, we use a filter length of  $L_1 = 40$ . Since the main task of the first stage is to cancel the strong SI from the direct path, a short filter length is used. For the ERLS-DCD algorithm, the forgetting factor is  $\lambda_1 = 0.999$ , the number of bits representing the impulse response  $M_b = 16$ , and the number of updates  $N_u = 16$ . For the second stage, the beamformer length is  $L_2 = 16$ . The forgetting factor is  $\lambda_2 = 0.985$ , the number of bits

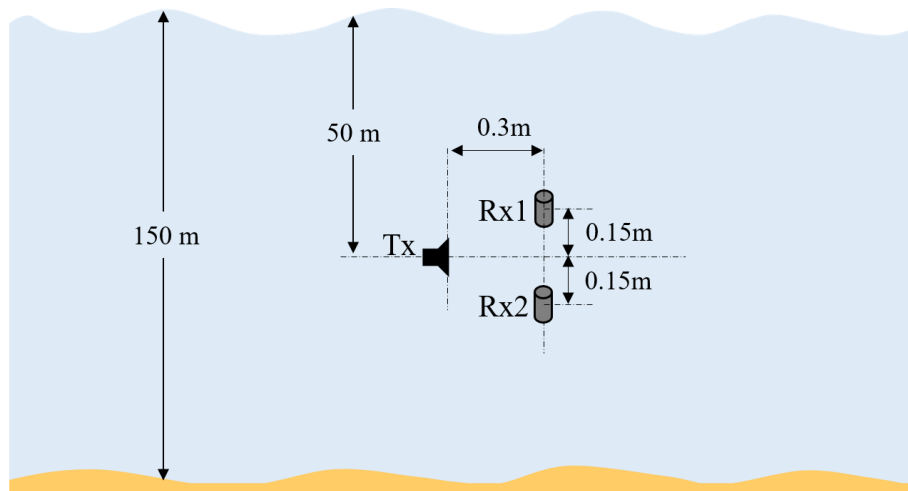


Fig. 5.11 Configuration of the simulation scenario with time-varying surface waves.

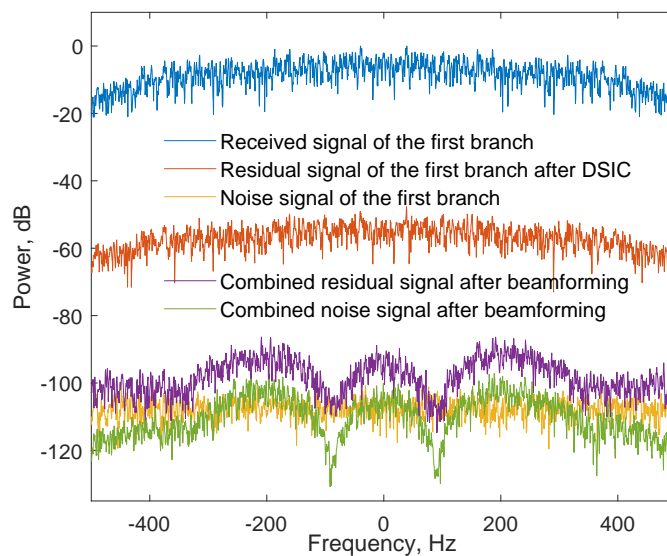


Fig. 5.12 Power spectra of signals in an environment with time-varying sea surface produced by the Waymark simulator. The power spectral densities are normalized with respect to the maximum of the power spectral density of the received signal. Received signal of the first branch and the combined residual signal after beamforming refer to  $x_1(i)$  and  $e_c(i)$  in Fig. 5.9, respectively. Residual signal of the first branch after DSIC refers to  $e_1(i)$ .

representing the beamformer coefficients  $M_b = 20$ , and the number of updates  $N_u = 36$ . At the second stage, a high number of DCD iterations is required at each time instant. This is chosen to improve the tracking ability of the ERLS-DCD algorithm in the time-varying environment.

As shown in Fig. 5.12, the residual SI is around 50 dB higher than the noise floor at the first branch ( $R_{SI,1} \approx 50$  dB) after the first stage of cancellation. Similar cancellation performance is also observed at the second branch. The power spectra of the signals on the second branch is omitted here due to the similarity. After adaptive beamforming, the combined residual signal level is around 10 dB higher than the combined noise level ( $R_{SI,c} \approx 10$  dB), which indicates that around 40 dB of extra SIC is achieved at the second stage. These results show the efficiency of the two-stage SIC scheme in an environment with reflections from time-varying sea surface.

### 5.2.3 Experimental results

In this section, we investigate the performance of the proposed SIC scheme in water tank and in lake experiments. The list of equipment used in the experiments is shown in Table 5.3.

Table 5.3 List of equipment used in the experiments

| Hardware component | Product                                    |
|--------------------|--|
| Projector          | Benthowave BII-7530 [78]                   |
| Hydrophone 1       | Benthowave BII-7011 [80]                   |
| Hydrophone 2       | Benthowave BII-7032 with pre-amplifier[80] |
| Transmitter        | Zoom F4 multitrack recorder [74]           |
| Receiver           | Zoom F4 multitrack recorder [74]           |
| Power amplifier    | PULSE PLA300 [75]                          |
| Attenuator         | Behringer DI00 [77]                        |



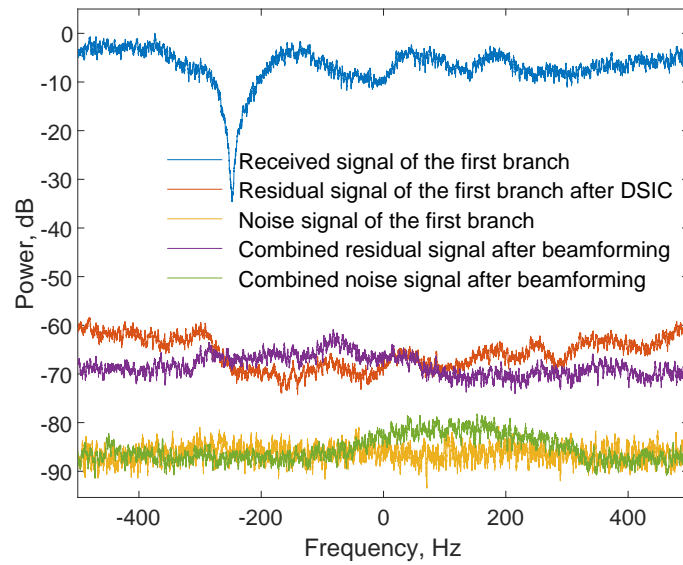
Fig. 5.13 Configuration of the water tank experiments. The plastic water tank is filled with 120 litre of water.

In all experiments, the transmitted signal length is 35 s, which includes 5 s of zero padding before data transmission. The signal recorded during the silence period is used to measure the background noise level.

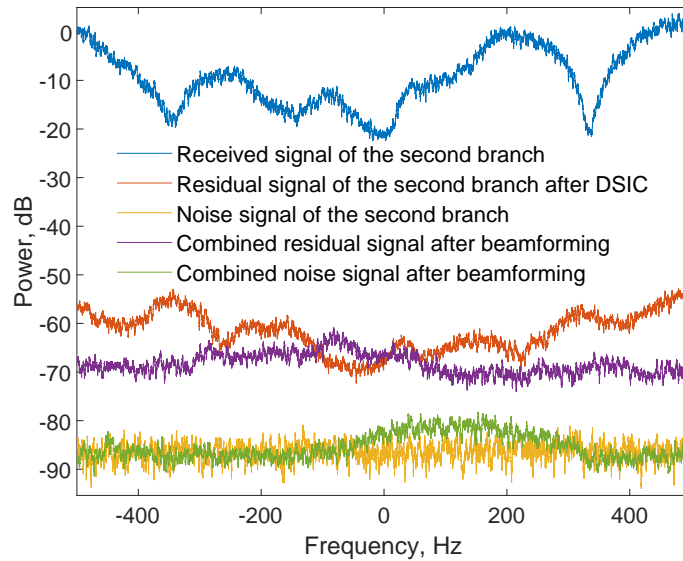
### Tank experiments

The tank experiments are conducted in an indoor plastic water tank. The configuration of the experimental setup is shown in Fig. 5.13. During the experiments, the projector and the hydrophones are clamped with two retort stands and submerged in the water. The projector is placed at one end of the tank, two hydrophones are placed vertically (4 cm apart) at the other end of the tank. The horizontal distance between the projector and hydrophones is around 70 cm. For the tank experiments, we transmit BPSK signals at carrier frequency  $f_c = 12$  kHz with 1.2 kHz bandwidth.

Note that one of the hydrophones (hydrophone 1) is equipped with an integrated pre-amplifier, which will cause a significant difference in the signal level recorded by the two hydrophones. Since the background noise is recorded simultaneously by both hydrophones in the same environment, it is reasonable to assume that the noise level should be the same. Therefore, we adjust the received signal level from hydrophone 2 to make sure that the noise recorded on both hydrophones is at the same level within the bandwidth of interest.



(a) First branch



(b) Second branch

Fig. 5.14 Power spectra of the signals in the water tank experiment. The power spectral densities are normalized with respect to the maximum of the power spectral density of the received signal on the first branch. Received signals of the first and second branches and combined residual signal after beamforming refer to  $x_1(i)$ ,  $x_2(i)$  and  $e_c(i)$  in Fig. 5.9, respectively. Residual signals of the first and second branches after DSIC refer to  $e_1(i)$  and  $e_2(i)$ , respectively.

For digital cancellation, we use a filter length  $L_1 = 100$ . The parameters of the ERLS-DCD algorithm used at the first cancellation stage are as follows: the forgetting factor  $\lambda_1 = 0.99$ , the number of bits representing the impulse response is  $M_b = 16$ , and the number of updates is  $N_u = 36$ . For the beamformer, a filter length  $L_2 = 10$  is used. The forgetting factor  $\lambda_2 = 0.9$ . For DCD iterations, we use  $M_b = 16$ , and  $N_u = 16$ .

As shown in Fig. 5.14 (a) and (b), the residual SI level are 19.8 dB and 24.5 dB higher than the noise floor at the first and second hydrophone after the first stage of SIC, respectively. After adaptive beamforming, the combined SI level is 16.8 dB higher than the combined noise level. In this experiment, the beamformer brings extra cancellation of 3 dB and 7.7 dB (for the first and second branches, respectively) on top of the first stage of cancellation. We believe that the additional cancellation achieved by the second stage is limited because of the high number of reflections received from the close boundaries of the water tank. Those arrivals from different angles introduce extra difficulties to the beamformer to adjust its beam pattern. In open water (lake or sea) trials, the reflections are received mostly from the surface and the bottom. In that case, better performance could be achieved than that in the water tank.

### Lake experiments

The lake experiments are conducted in a shallow lake on the west campus of the University of York. The experimental site is shown in Fig. 5.15. The maximum depth of the lake around the experimental site is about 1 m. The configuration of the projector and two hydrophones is shown in Fig. 5.16. The distance between the projector and each hydrophone is around 20 cm. During the experiments, the projector and the two hydrophones are clamped on a pipe and vertically submerged in the lake. For the lake experiments, we transmit BPSK signal at carrier frequency  $f_c = 14$  kHz with 1.2 kHz bandwidth.

In this experiment, the SI to noise ratio at both hydrophone outputs is around 56 dB. We use a filter length of 50 taps. The parameters used for the ERLS-DCD algorithm at the first cancellation stage are as follows: the forgetting factor is  $\lambda_1 = 0.985$ , the number of bits representing the impulse response is  $M_b = 16$ , and the number of updates  $N_u = 32$ . After



Fig. 5.15 Experimental site on the lake.

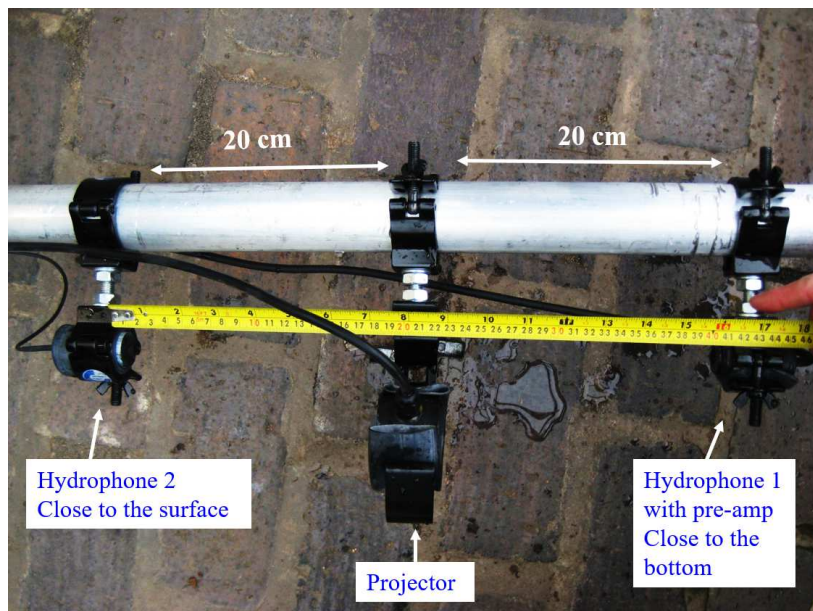
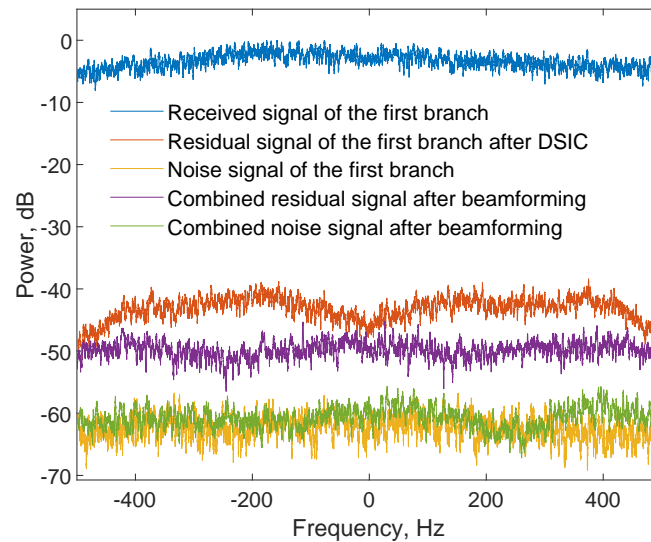
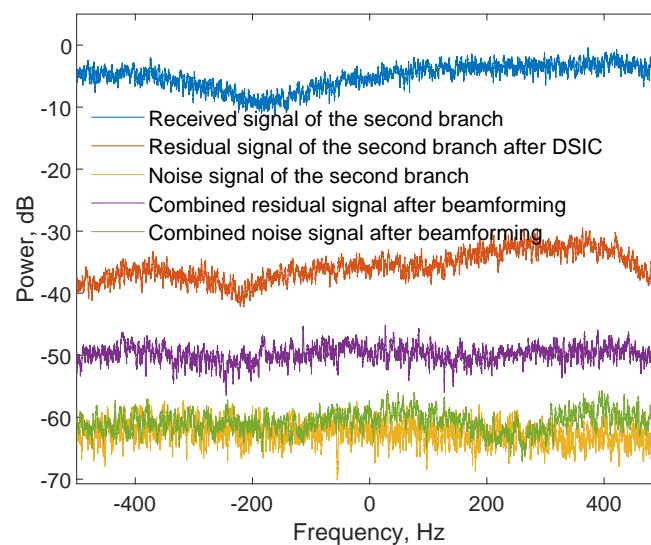


Fig. 5.16 Projector/hydrophones configuration for the lake experiment.



(a) First branch



(b) Second branch

Fig. 5.17 Power spectra of signals in the lake experiment. The power spectral densities are normalized with respect to the maximum of the power spectral density of the received signal on the first branch. Received signals of the first and second branches and combined residual signal after beamforming refer to  $x_1(i)$ ,  $x_2(i)$  and  $e_c(i)$  in Fig. 5.9, respectively. Residual signals of the first and second branches after DSIC refer to  $e_1(i)$  and  $e_2(i)$ , respectively.

the first stage of cancellation,  $R_{SI,1}$  and  $R_{SI,2}$  are 17.6 dB and 25.4 dB, respectively (See Fig. 5.17 (a) and (b)). Note that the lower residual SI level is achieved with the hydrophone closer to the bottom, which is less influenced by the moving surface.

For the second stage of cancellation, we use a beamformer with  $L_2 = 12$  taps. The forgetting factor is  $\lambda_2 = 0.9$ . For DCD iterations, we use  $M_b = 16$ , and  $N_u = 32$ . After the adaptive beamforming, the combined SI level is 11.1 dB higher than the combined noise level. This result indicates that by using adaptive beamforming, we achieve 6.5 dB and 14.3 dB of extra SIC compared to the results obtained by the first stage in the first and second branches, respectively. This can be considered as a promising improvement in the cancellation performance.

## 5.3 Conclusions and discussion

In this chapter, we have proposed two SIC schemes with multiple antennas for FD UWA systems.

The first multiple antenna cancellation scheme is operated in the acoustic domain. The SIC is performed using an extra (secondary) projector that emits an acoustic signal for cancelling the SI at the receive antenna. Since the primary and secondary paths are unknown, they are adaptively estimated using ERLS-DCD adaptive filters. Simulation results based on the Waymark simulation show that the proposed scheme can significantly reduce the SI level and achieve reliable communication in time-invariant channels. So far, this cancellation scheme has not been verified using experimental data. Unlike digital cancellation, for which we can record the experimental data and operate SIC afterwards, acoustic cancellation requires real-time processing of the experimental data. Further work will be done on real-time implementation of the acoustic SIC scheme.

Another thing which is worth to mention is that the effect of the PA nonlinearity is not taken into account in the acoustic SIC scheme. In this design, the digital data is used as the regressor of the adaptive filter. The cancellation performance will unavoidably degrade when the PA nonlinearity is incorporated in the adaptation. However, the main task of the

acoustic cancellation scheme is not to cancel the SI completely in the acoustic domain but to reduce the burden of the digital cancellation. Thus, a combination of acoustic and digital cancellation will be investigated in the future work.

The second multiple antenna cancellation scheme we have proposed is the two-stage digital SIC scheme. In the first stage, the ERLS-DCD adaptive filter is used for digital cancellation. The main purpose of the first stage is to cancel the strong and stable SI received from the direct path. At the second stage, we use an ERLS-DCD-based adaptive beamformer to cancel the time-varying reflections from the sea surface. The performance of the proposed scheme is investigated by using both simulation and experimental data. The Waymark simulation results indicate that the SIC performance can be significantly improved compared to the single-hydrophone digital SIC under the tested time-varying environment.

For the tank experimental data, close to 60 dB of SIC has been achieved at the first stage, however, the cancellation performance provided by the beamformer is somewhat limited. The second stage only provides 3 dB and 7.7 dB extra cancellation with respect to the first stage. We believe the reason behind this is that the beamformer is trying to cancel all the SI components reflected from the close boundaries of the tank. For the lake experiments, around 35 dB of SI is cancelled at the first stage by digital SIC. This level of cancellation is reasonable considering the time-varying environment of the test site. In this scenario, the beamformer provides 6.5 dB and 14.3 dB improvement in the cancellation performance, which is very promising.

# Chapter 6

## Conclusions and Further Work

### 6.1 Conclusions

FD operation allows simultaneous transmission and reception of signals in the same frequency bandwidth by closely positioned transmit and receive antennas. It can significantly increase the throughput of UWA systems. To enable FD operation, the strong SI from the near-end transmitter needs to be eliminated. The aim of this work is to achieve a high level of SIC in FD UWA systems. The main approach applied for SIC is digital cancellation. The main factors that limit the digital cancellation performance come from the imperfections of the equipments and the time-varying nature of the UWA channels. To address the distortions introduced in the transmit and receive chains, different structures of the digital SI canceller have been investigated. Regarding the fast channel variation due to the moving lake/sea surfaces, two approaches have been proposed; one is to use interpolating adaptive filtering algorithms which are capable of tracking the fast-varying channels, the other approach is to use multiple hydrophones for adaptive beamforming. An acoustic-domain SIC scheme using multiple projectors has been proposed to achieve extra amount of SI in the acoustic domain before digital cancellation. Based on the experimental results presented in this thesis, it can be concluded that a high level of SIC has been achieved with the proposed SI canceller structure and novel adaptive filtering algorithms.

The contributions from the work presented in this thesis is summarized as follows:

### **General structure of digital SIC scheme**

A general structure of the digital SI canceller has been proposed. The proposed structure uses the PA output as a reference signal for adaptive filtering, which significantly improves the cancellation performance and allows a low-complexity design using linear adaptive filters. To deal with the distortion caused by the passband to baseband conversion process, a multi-branch combining scheme has been incorporated into the SI canceller. An adaptive nonlinear equalizer has also been incorporated in the digital SI canceller to improve the cancellation performance by equalizing the nonlinearity introduced by the hydrophone pre-amplifier. With the proposed digital canceller structure, as high as 73 dB of SIC has been achieved in anechoic tank experiments.

### **ERLSd, SRLSd and SRLS-P adaptive filters**

Delayed versions of the ERLS and SRLS adaptive filters have been proposed. The dependence between the delay of the input signals and the SIC performance of the ERLS and SRLS adaptive filters has been investigated. For the SRLS adaptive filter, the optimal delay is half of the sliding window length, while the optimal delay for the ERLS adaptive filter varies in different scenarios. A new adaptive filter based on the SRLS algorithm and parabolic approximation of channel variation in time (SRLS-P) has been proposed. As indicated by the simulation and experimental results, the SIC performance can be significantly improved with the proposed algorithms compared to that of the classical SRLS algorithm in time-varying scenarios. It has been shown in a lake experiment that the SRLS-P adaptive filter outperforms the classical SRLS algorithm by 6 dB in the SIC performance.

### **SICF for measuring the SIC performance**

The MSE is not suitable for evaluating the SIC performance for interpolating adaptive filters due to the over-fitting problem. Therefore, a new evaluation metric, the SICF, has been proposed. The SICF measures the SIC performance as a factor of improvement in the SIR due to the SIC and takes into account the loss of the far-end signal after SIC. The SICF has

been validated by comparing with the MSD and BER in simulations. Results show that the SICF is well suited for evaluating the performance of FD UWA systems, especially when the true SI channel is unknown.

### **SRLS-L, SRLS-L-DCD and HSRLS-L-DCD adaptive filters**

A computationally efficient interpolating adaptive filter (SRLS-L) has been proposed for identification of time-varying SI channels. It is based on the SRLS algorithm and specified for Legendre polynomials. The SRLS-L-DCD adaptive algorithm has been proposed to further reduce the complexity by solving the system of equations recursively using the DCD iterations. A sparse adaptive filtering algorithm (HSRLS-L-DCD) based on homotopy iterations has been proposed to exploit the sparsity in the expansion coefficients. Simulation results show that the SRLS-L adaptive filter provides the same tracking performance as the state-of-the-art algorithm with significantly lower complexity. The HSRLS-L-DCD algorithm outperforms the SRLS-L-DCD algorithm with approximately the same complexity. With the third-order HSRLS-L-DCD algorithm, up to 13 dB improvement in the SIC performance has been achieved compared to the classical SRLS algorithm in the lake experiments.

### **SIC schemes with multiple antennas**

A SIC scheme with two projectors has been proposed to achieve SIC in the acoustic domain before digital cancellation. The SIC is performed using a secondary projector that emits an acoustic signal for cancelling the SI at the hydrophone. The performance of the proposed scheme is evaluated by simulation in a time-invariant scenario. The results demonstrate a good potential of achieving high level of SIC in the acoustic domain. A two-stage SIC scheme with two hydrophones has been proposed for eliminating the fast-varying surface reflections. The first stage cancels the strong and stable SI received at the two hydrophones via the direct path. An adaptive beamformer is used at the second stage to cancel the time-varying reflections from the moving surface. As indicated by the simulation and experimental results, extra amount of SIC can be achieved with adaptive beamforming.

## 6.2 Further work

In this section, a number of suggestions are given for further work based on this thesis. They are summarized as follow:

- Nonlinear distortions introduced by the equipment is one of the main limiting factors of digital SIC performance. It is proposed in Chapter 2 to use the PA output as the reference signal to incorporate the nonlinearity introduced by the PA. It is believed that the PA output is the best candidate to be used as the reference signal for digital cancellation. This is true if the projector has a linear response. However, the projector may exhibit nonlinear distortions when the input signal level is too high [50]. In such a case, the PA output cannot accurately represent the transmitted signal emitted by the projector. Apart from the nonlinearity in the projector, when high acoustic power radiated into the water, the acoustic propagation would be accompanied by a series of nonlinear acoustic effects [120], which include generation of harmonics of the original signal, creation of cavitation and parametric acoustic array. Further research can be conducted on modelling the nonlinearity of the projector and the underwater acoustics. Another way around it is to place an adjacent hydrophone close to the projector to record the transmitted signal in the acoustic domain. It would be useful to investigate the SIC performance with the recorded signal being used as the reference signal with the proposed SIC scheme.
- In Chapter 3, the SICF is proposed to evaluate the SIC performance in FD UWA systems without the need to build a whole FD system. The ultimate way of evaluating the performance of the FD UWA systems is to implement a whole FD system and to investigate the far-end detection performance. However, at that time, the proposed digital cancellation techniques are not capable of cancelling the SI to the receiver's noise floor in field experiments. In Chapter 4, new interpolating adaptive filters of excellent tracking performance have been proposed. We believe that it is worth to try to implement the whole FD UWA system with far-end signal transmission. At the early

stage, we suggest to use spread-spectrum signals as the far-end signal as described in Chapter 3 due to its high resistance to interference.

- The far-end signal is treated as extra interference when estimating the near-end SI channel. The channel estimation performance can be improved if the far-end signal is removed from the received signal. This could be done by applying turbo iterations as suggested in [42]. Firstly, the SI channel is estimated when the far-end signal is present. The output of the adaptive filter at this stage can be used as an estimate of the baseband far-end signal. The far-end transmitted symbols are then demodulated to provide an estimate of the passband far-end signal. The far-end channel can be estimated using the estimated far-end signal and the received signal. The received far-end signal is then reconstructed and subtracted from the received signal. After that, the near-end SI channel is re-estimated. More accurate channel estimates and in turn SI recovery can be obtained with such iterations.
- For investigation of digital cancellation, the SIC can be done off-line with the recorded experimental data. For the acoustic-domain SIC scheme proposed in Chapter 5, the cancellation is done in the acoustic domain, which requires real-time processing. It is desirable to implement the adaptive cancellation algorithm on a DSP board so that the acoustic cancellation performance can be evaluated in field experiments. The manually introduced delay in the cancellation scheme and the processing delay of the DSP board should be taken into account in the hardware design. If the acoustic cancellation scheme could be successfully implemented, it would be useful to investigate the performance of the joint acoustic and digital cancellation scheme.



# **Appendix A**

## **Lake surfaces during the experiments**



(a) Lake surface on the 8th of May 2019.



(b) Lake surface on the 15th of May 2019.

Fig. A.1 Lake surfaces at the Kelk Lake under different weather condition.

# Appendix B

## Derivation of the channel estimate obtained by the SRLS algorithm

We now derive the presentation (3.26) for the channel estimate  $\hat{\mathbf{h}}(i)$  obtained by the SRLS algorithm.

In the SRLS adaptive filter, without the noise, the estimate at time instant  $i$  is given by

$$\begin{aligned}\hat{\mathbf{h}}(i) &= [\mathbf{S}^H(i)\mathbf{S}(i)]^{-1}\mathbf{S}^H(i)\mathbf{x}(i), \\ &= \mathbf{R}^{-1}(i)\mathbf{S}^H(i) \text{diag}\{\mathbf{S}(i)\mathbf{H}(i)\}, \\ &= \mathbf{R}^{-1}(i)\mathbf{S}^H(i) \sum_{m=0}^{M-1} \mathbf{e}_m \mathbf{e}_m^T \mathbf{S}(i)\mathbf{H}(i)\mathbf{e}_m, \\ &= \frac{1}{M}\mathbf{R}^{-1}(i) \sum_{m=0}^{M-1} \mathbf{S}^H(i)\mathbf{e}_m \mathbf{e}_m^T \mathbf{S}(i)\mathbf{H}(i)\mathbf{e}_m,\end{aligned}\tag{B.1}$$

where  $\mathbf{e}_m$  is a column vector of zero elements, apart from the  $m$ th element which equals one,  $\mathbf{S}(i) = [\mathbf{s}(i), \dots, \mathbf{s}(i - M + 1)]^T$  is an  $M \times L$  observation matrix,  $\mathbf{H}(i) = [\mathbf{h}(i), \dots, \mathbf{h}(i - M + 1)]$  is an  $L \times M$  channel matrix, and  $\mathbf{h}(i)$  is the true channel impulse response at the  $i$ th time instant. Here, we used the fact that, in the absence of noise,  $\mathbf{x}(i) = \text{diag}\{\mathbf{S}(i)\mathbf{H}(i)\}$ .

Equation (B.1) can be further written as:

$$\begin{aligned}
\hat{\mathbf{h}}(i) &= \frac{1}{M} \mathbf{R}^{-1}(i) \sum_{m=0}^{M-1} \mathbf{s}^*(i-m) \mathbf{s}^T(i-m) \mathbf{H}(i) \mathbf{e}_m \\
&= \frac{1}{M} \mathbf{R}^{-1}(i) \sum_{m=0}^{M-1} \mathbf{s}^*(i-m) \mathbf{s}^T(i-m) \mathbf{h}(i-m) \\
&= \frac{1}{M} \mathbf{R}^{-1}(i) \sum_{m=0}^{M-1} \mathbf{R}_{i-m} \mathbf{h}(i-m) \\
&= \frac{1}{M} \mathbf{R}^{-1}(i) \sum_{m=-M+1}^0 \mathbf{R}_{i+m} \mathbf{h}(i+m),
\end{aligned} \tag{B.2}$$

where we use  $\mathbf{H}(i) \mathbf{e}_m = \mathbf{h}(i-m)$ ,  $\mathbf{S}^H(i) \mathbf{e}_m = \mathbf{s}^*(i-m)$ , and denote  $\mathbf{R}_{i-m} = \mathbf{s}^*(i-m) \mathbf{s}^T(i-m)$ . By replacing  $i$  with  $i+k$ , this can also be rewritten as:

$$\hat{\mathbf{h}}(i+k) = \frac{1}{M} \mathbf{R}^{-1}(i+k) \sum_{m=-M+k+1}^k \mathbf{R}_{i+m} \mathbf{h}(i+m). \tag{B.3}$$

# Appendix C

## Complexity analysis of the LBF estimator

Recursive computation methods are proposed in [104] to reduce the complexity of the LBF estimator (see [104] and MATLAB in [117]). The main steps of the LBF estimator are summarized as follows:

- $\mathbf{A}(i) = \boldsymbol{\xi}(i)\boldsymbol{\xi}^H(i)$ , where  $\boldsymbol{\xi}(i)$  is an  $L \times 1$  complex-valued vector. This involves  $4L^2$  real-valued MACs.
- $\mathbf{r}_m(i) \leftarrow \beta\boldsymbol{\Gamma}\mathbf{r}_m(i)$ , where  $\beta$  is a scalar,  $\mathbf{r}_m(i)$  is a  $(P+1)L \times 1$  complex-valued vector and  $\boldsymbol{\Gamma}$  is a real-valued  $(P+1)L \times (P+1)L$  matrix. This would require  $2(P+1)^2L^2$  MACs.
- $\mathbf{R}_m(i) \leftarrow \mathbf{R}_m(i) - v_1\mathbf{A}(i) \otimes \mathbf{B}$ , where  $\mathbf{R}_m(i)$  is a  $(P+1)L \times (P+1)L$  complex-valued matrix,  $\mathbf{A}(i)$  is an  $L \times L$  complex-valued matrix and  $\mathbf{B}$  is a  $(P+1) \times (P+1)$  real-valued matrix. This requires  $2(P+1)^2L^2$  MACs.
- $\mathbf{R}_m(i) \leftarrow \beta(\boldsymbol{\Gamma}\mathbf{R}_m(i)\boldsymbol{\Gamma}^T)$ , which requires  $2(P+1)^3L^3$  MACs.
- $\mathbf{R}_m(i) \leftarrow \mathbf{R}_m(i) + v_M\mathbf{A}(i) \otimes \mathbf{B}$ , which requires  $2(P+1)^2L^2$  MACs.
- Solve the system of equations:  $\mathbf{R}_m(i)\mathbf{a}(i) = \mathbf{r}_m(i)$ . This would require about  $4(P+1)^3L^3$  MACs.

The overall complexity of the main steps of the LBF estimator is about  $6(P + 1)^3 L^3 + 6(P + 1)^2 L^2 + 4L^2$  MACs.

# Appendix D

## Complexity analysis of the HSRLS-L-DCD algorithm

The HSRLS-L-DCD algorithm solves the system of equations using the  $H\ell_1$ -DCD algorithm. The complexity of the main steps of the  $H\ell_1$ -DCD algorithm is summarized as follows:

- The residual vector  $\mathbf{r}(i)$  in (4.24) can be computed with  $4(P+1)L^2$  MAC operations;
- The regularization parameter  $\tau$  (at Step 1 in  $H\ell_1$ -DCD algorithm) can be computed with  $2(P+1)L$  MAC operations;
- Removing an element from the support  $I$  and updating the residual vector involve  $4(P+1)L + 7|I|$  multiplications and  $2(P+1)L + 4|I|$  additions and  $|I|$  square-root operations, where  $|I|$  is the cardinality of the support  $I$ ;
- Adding an element into the support  $I$  takes  $4((P+1)L - |I|)$  multiplications,  $2((P+1)L - |I|)$  additions,  $(P+1)L - |I|$  divisions and  $(P+1)L - |I|$  square-root operations;
- Solving the optimization problem on the support  $I$  using the leading  $\ell_1$ -DCD algorithm:
  - Computing the threshold  $T_c$  requires  $2(P+1)L$  MACs;
  - Finding the maximum element of the residual vector requires  $2|I|$  MAC operations, this could be repeated for  $N_u + M_b$  times;

- Computing the increment of the cost function ( $\Delta J(k)$ ) and finding the direction of update which minimizes the cost function can be done with 6 multiplications and 15 additions, this is repeated for at most  $N_u + M_b$  times;
- Updating the residual vector requires  $2(P + 1)L$  MAC operations, this can be done at most  $N_u$  times;
- Obtaining the final support according to (4.27) requires  $2(P + 1)L$  MAC operations and  $(P + 1)L$  square-root operations;
- Reweighting according to (4.28) involves  $(P + 1)L$  MACs.

In total, the  $H\ell_1$ -DCD algorithm minimizes the cost function with  $4(P + 1)^2L^2 + (15 + 2N_u)(P + 1)L + 2|I|(N_u + M_b)$  MAC operations,  $(P + 1)L - |I|$  divisions and  $2(P + 1)L$  square-root operations.

Thus, the overall complexity of the HSRLS-L-DCD algorithm is  $4(P + 1)^2L^2 + (15 + 2N_u)(P + 1)L + 2|I|(N_u + M_b)$  MAC operations,  $3(P + 1)^2/2 + 3(P + 1)$  FFT operations of size  $(L + M)$ ,  $(P + 1)L - |I|$  divisions and  $2(P + 1)L$  square-root operations.

# Acronyms

**ADC** Analogue-to-Digital Converter

**BEM** Basis Expansion Model

**BPSK** Binary Phase-Shift Keying

**DAC** Digital-to-Analogue Converter

**DCD** Dichotomous Coordinate Descent

**DSIC** Digital Self-Interference Cancellation

**ERLS** Exponentially weighted Recursive Least Squares

**FD** Full-Duplex

**FFT** Fast Fourier Transform

**FIR** Finite Impulse Response

**IFFT** Inverse Fast Fourier Transform

**I/Q** In-phase and Quadrature

**LBF** Local Basis Function

**LMS** Least Mean Squares

**LS** Least Squares

**OFDM** Orthogonal Frequency-Division Multiplexing

**PA** Power Amplifier

**QPSK** Quadrature Phase-Shift Keying

**RLS** Recursive Least Squares

**RRC** Root-Raised Cosine

**SI** Self-Interference

**SIC** Self-Interference Cancellation

**SICF** Self-Interference Cancellation Factor

**SNR** Signal to Noise Ratio

**SRLS** Sliding-window Recursive Least Squares

**SSP** Sound speed profile

**UWA** Underwater Acoustic

# References

- [1] L. Shen, B. Henson, Y. Zakharov, and P. Mitchell, “Digital self-interference cancellation for full-duplex underwater acoustic systems,” *IEEE Transactions on Circuits and Systems II: Express Briefs*, vol. 67, no. 1, pp. 192–196, 2019.
- [2] L. Shen, B. Henson, Y. V. Zakharov, and P. Mitchell, “Two-stage self-interference cancellation in full-duplex underwater acoustic systems,” in *MTS/IEEE Oceans - Marseille*, 2019, pp. 1–6.
- [3] L. Shen, B. Henson, Y. Zakharov, and P. Mitchell, “Robust digital self-interference cancellation for full-duplex UWA systems: Lake experiments,” in *Underwater Acoustics Conference and Exhibition*, 2019, pp. 243–250.
- [4] L. Shen, B. Henson, Y. Zakharov, and P. D. Mitchell, “Adaptive nonlinear equalizer for full-duplex underwater acoustic systems,” *IEEE Access*, vol. 8, pp. 108 169 – 108 178, 2020.
- [5] L. Shen, Y. Zakharov, B. Henson, N. Morozs, and P. Mitchell, “Adaptive filtering for full-duplex UWA systems with time-varying self-interference channel,” *IEEE Access*, vol. 8, pp. 187 590–187 604, 2020.
- [6] L. Shen, Y. Zakharov, L. Shi, and B. Henson, “BEM adaptive filtering for SI cancellation in FD underwater acoustic systems,” *submitted to Signal Processing*, Under review.
- [7] Y. Wang, Y. Li, L. Shen, and Y. Zakharov, “Acoustic-domain self-interference cancellation for full-duplex underwater acoustic communication systems,” in *IEEE Asia-Pacific Signal and Information Processing Association Annual Summit and Conference*, 2019, pp. 1112–1116.
- [8] Y. Zakharov, Y. Fei, P. Mitchell, N. Morozs, B. Henson, L. Shen, and T. Tozer, “Low-complexity UAC modem and data packet structure,” in *IEEE Underwater Communications and Networking Conference*, 2018, pp. 1–5.
- [9] Y. Zakharov, B. Henson, R. Diamant, Y. Fei, P. D. Mitchell, N. Morozs, L. Shen, and T. C. Tozer, “Data packet structure and modem design for dynamic underwater acoustic channels,” *IEEE Journal of Oceanic Engineering*, vol. 44, no. 4, pp. 837–849, 2019.

- [10] N. Morozs, W. Gorma, B. T. Henson, L. Shen, P. D. Mitchell, and Y. Zakharov, "Channel modeling for underwater acoustic network simulation," *IEEE Access*, 2020.
- [11] M. Stojanovic, "Underwater acoustic communications," in *Proceedings of Electro/International 1995*, 1995, pp. 435–440.
- [12] M. Chitre, S. Shahabudeen, and M. Stojanovic, "Underwater acoustic communications and networking: Recent advances and future challenges," *Marine Technology Society Journal*, vol. 42, no. 1, pp. 103–116, 2008.
- [13] C. C. Eriksen, T. J. Osse, R. D. Light, T. Wen, T. W. Lehman, P. L. Sabin, J. W. Ballard, and A. M. Chiodi, "Seaglider: A long-range autonomous underwater vehicle for oceanographic research," *IEEE Journal of Oceanic Engineering*, vol. 26, no. 4, pp. 424–436, 2001.
- [14] P. Felisberto, S. M. Jesus, F. Zabel, R. Santos, J. Silva, S. Gobert, S. Beer, M. Björk, S. Mazzuca, G. Procaccini *et al.*, "Acoustic monitoring of O<sub>2</sub> production of a seagrass meadow," *Journal of Experimental Marine Biology and Ecology*, vol. 464, pp. 75–87, 2015.
- [15] K. Wang, H. Gao, X. Xu, J. Jiang, and D. Yue, "An energy-efficient reliable data transmission scheme for complex environmental monitoring in underwater acoustic sensor networks," *IEEE Sensors Journal*, vol. 16, no. 11, pp. 4051–4062, 2015.
- [16] I. F. Akyildiz, D. Pompili, and T. Melodia, "Challenges for efficient communication in underwater acoustic sensor networks," *ACM Sigbed Review*, vol. 1, no. 2, pp. 3–8, 2004.
- [17] I. F. Akyildiz, D. Pompili, and T. Melodia, "Underwater acoustic sensor networks: Research challenges," *Ad Hoc Networks*, vol. 3, no. 3, pp. 257–279, 2005.
- [18] T. H. Eggen, A. B. Baggeroer, and J. C. Preisig, "Communication over Doppler spread channels. Part I: Channel and receiver presentation," *IEEE Journal of Oceanic Engineering*, vol. 25, no. 1, pp. 62–71, 2000.
- [19] R. Urick, *Principles of Underwater Sound*. Peninsula Publishing, 2013.
- [20] A. Sabharwal, P. Schniter, D. Guo, D. W. Bliss, S. Rangarajan, and R. Wichman, "In-band full-duplex wireless: Challenges and opportunities," *IEEE Journal on Selected Areas in Communications*, vol. 32, no. 9, pp. 1637–1652, 2014.
- [21] D. Bharadia, E. McMillin, and S. Katti, "Full duplex radios," in *ACM SIGCOMM Computer Communication Review*, vol. 43, no. 4, 2013, pp. 375–386.
- [22] A. Goldsmith, *Wireless Communications*. Cambridge university press, 2005.
- [23] J. I. Choi, M. Jain, K. Srinivasan, P. Levis, and S. Katti, "Achieving single channel, full duplex wireless communication," in *Annual International Conference on Mobile Computing and Networking*, 2010, pp. 1–12.

- [24] D. Bliss, P. Parker, and A. Margetts, "Simultaneous transmission and reception for improved wireless network performance," in *IEEE Workshop on Statistical Signal Processing*, 2007, pp. 478–482.
- [25] B. Radunovic, D. Gunawardena, P. Key, A. Proutiere, N. Singh, V. Balan, and G. De-jean, "Rethinking indoor wireless mesh design: Low power, low frequency, full-duplex," in *IEEE 5th Workshop on Wireless Mesh Networks*, 2010, pp. 1–6.
- [26] M. Duarte and A. Sabharwal, "Full-duplex wireless communications using off-the-shelf radios: Feasibility and first results," in *44th Asilomar Conference on Signals, Systems and Computers*, 2010, pp. 1558–1562.
- [27] E. Everett, M. Duarte, C. Dick, and A. Sabharwal, "Empowering full-duplex wireless communication by exploiting directional diversity," in *Asilomar Conference on Signals, Systems and Computers*, 2011, pp. 2002–2006.
- [28] D. Bharadia and S. Katti, "Full duplex MIMO radios," in *Symposium on Networked Systems Design and Implementation*, 2014, pp. 359–372.
- [29] V. R. Cadambe and S. A. Jafar, "Degrees of freedom of wireless networks with relays, feedback, cooperation, and full duplex operation," *IEEE Transactions on Information Theory*, vol. 55, no. 5, pp. 2334–2344, 2009.
- [30] H. Ju and R. Zhang, "Optimal resource allocation in full-duplex wireless-powered communication network," *IEEE Transactions on Communications*, vol. 62, no. 10, pp. 3528–3540, 2014.
- [31] S. Lourey, "Adaptive filtering for enhanced detection of continuous active sonar signals," in *Proceedings of the Underwater Acoustics Conference and Exhibition*, 2017, pp. 145–152.
- [32] D. Havelock, S. Kuwano, and M. Vorländer, *Handbook of Signal Processing in Acoustics*. Springer New York, 2008.
- [33] D. Korpi, T. Riihonen, V. Syrjälä, L. Anttila, M. Valkama, and R. Wichman, "Full-duplex transceiver system calculations: Analysis of ADC and linearity challenges," *IEEE Transactions on Wireless Communications*, vol. 13, no. 7, pp. 3821–3836, 2014.
- [34] L. Anttila, D. Korpi, V. Syrjala, and M. Valkama, "Cancellation of power amplifier induced nonlinear self-interference in full-duplex transceivers," in *Asilomar Conference on Signals, Systems and Computers*, 2013, pp. 1193–1198.
- [35] T. Riihonen and R. Wichman, "Analog and digital self-interference cancellation in full-duplex MIMO-OFDM transceivers with limited resolution in A/D conversion," in *46th Asilomar Conference on Signals, Systems and Computers*, 2012, pp. 45–49.

- [36] Y. S. Choi and H. Shirani Mehr, "Simultaneous transmission and reception: Algorithm, design and system level performance," *IEEE Transactions on Wireless Communications*, vol. 12, no. 12, pp. 5992–6010, 2013.
- [37] D. Korpi, S. Venkatasubramanian, T. Riihonen, L. Anttila, S. Otewa, C. Icheln, K. Haneda, S. Tretyakov, M. Valkama, and R. Wichman, "Advanced self-interference cancellation and multiantenna techniques for full-duplex radios," in *Asilomar Conference on Signals, Systems and Computers*, 2013, pp. 3–8.
- [38] D. Korpi, J. Tamminen, M. Turunen, T. Huusari, Y.-S. Choi, L. Anttila, S. Talwar, and M. Valkama, "Full-duplex mobile device: Pushing the limits," *IEEE Communications Magazine*, vol. 54, no. 9, pp. 80–87, 2016.
- [39] D. Korpi, Y. S. Choi, T. Huusari, L. Anttila, S. Talwar, and M. Valkama, "Adaptive nonlinear digital self-interference cancellation for mobile inband full-duplex radio: Algorithms and RF measurements," in *IEEE Global Communications Conference*, 2015, pp. 1–7.
- [40] M. S. Sim, M. Chung, D. Kim, J. Chung, D. K. Kim, and C.-B. Chae, "Nonlinear self-interference cancellation for full-duplex radios: From link-level and system-level performance perspectives," *IEEE Communications Magazine*, vol. 55, no. 9, pp. 158–167, 2017.
- [41] M. Emara, P. Rosson, K. Roth, and D. Dassonville, "A full duplex transceiver with reduced hardware complexity," in *IEEE Global Communications Conference*, 2017, pp. 1–6.
- [42] S. Li and R. D. Murch, "An investigation into baseband techniques for single-channel full-duplex wireless communication systems," *IEEE Transactions on Wireless Communications*, vol. 13, no. 9, pp. 4794–4806, 2014.
- [43] J. G. McMichael and K. E. Kolodziej, "Optimal tuning of analog self-interference cancellers for full-duplex wireless communication," in *Annual Allerton Conference on Communication, Control, and Computing*, 2012, pp. 246–251.
- [44] J. H. Lee, "Self-interference cancelation using phase rotation in full-duplex wireless," *IEEE Transactions on Vehicular Technology*, vol. 62, no. 9, pp. 4421–4429, 2013.
- [45] M. Duarte, A. Sabharwal, V. Aggarwal, R. Jana, K. Ramakrishnan, C. W. Rice, and N. Shankaranarayanan, "Design and characterization of a full-duplex multiantenna system for WiFi networks," *IEEE Transactions on Vehicular Technology*, vol. 63, no. 3, pp. 1160–1177, 2014.
- [46] N. Li, W. Zhu, and H. Han, "Digital interference cancellation in single channel, full duplex wireless communication," in *IEEE International Conference on Wireless Communications, Networking and Mobile Computing*, 2012, pp. 1–4.

- [47] R. Askar, N. Zarifeh, B. Schubert, W. Keusgen, and T. Kaiser, "I/Q imbalance calibration for higher self-interference cancellation levels in full-duplex wireless transceivers," in *IEEE International Conference on 5G for Ubiquitous Connectivity*, 2014, pp. 92–97.
- [48] G. Qiao, S. Gan, S. Liu, and Q. Song, "Self-interference channel estimation algorithm based on maximum-likelihood estimator in in-band full-duplex underwater acoustic communication system," *IEEE Access*, vol. 6, pp. 62 324–62 334, 2018.
- [49] "Hydrophone handbook," <http://www.ondacorp.com>, [Accessed: 06- Feb- 2020].
- [50] J. Butler and C. Sherman, *Transducers and Arrays for Underwater Sound*, ser. Modern Acoustics and Signal Processing. Springer International Publishing, 2016.
- [51] M. Duarte, C. Dick, and A. Sabharwal, "Experiment-driven characterization of full-duplex wireless systems," *IEEE Transactions on Wireless Communications*, vol. 11, no. 12, pp. 4296–4307, 2012.
- [52] A. Sahai, G. Patel, and A. Sabharwal, "Pushing the limits of full-duplex: Design and real-time implementation," *arXiv preprint arXiv:1107.0607*, 2011.
- [53] G. Qiao, Y. Zhao, S. Liu, and N. Ahmed, "The effect of acoustic-shell coupling on near-end self-interference signal of in-band full-duplex underwater acoustic communication modem," in *International Bhurban Conference on Applied Sciences and Technology*, 2020, pp. 606–610.
- [54] G. Qiao, S. Liu, Z. Sun, and F. Zhou, "Full-duplex, multi-user and parameter reconfigurable underwater acoustic communication modem," in *MTS/IEEE Oceans - San Diego*, 2013, pp. 1–8.
- [55] S. Nikolaou, R. Bairavasubramanian, C. Lugo, I. Carrasquillo, D. C. Thompson, G. E. Ponchak, J. Papapolymerou, and M. M. Tentzeris, "Pattern and frequency reconfigurable annular slot antenna using PIN diodes," *IEEE Transactions on Antennas and Propagation*, vol. 54, no. 2, pp. 439–448, 2006.
- [56] M. Jain, J. I. Choi, T. Kim, D. Bharadia, S. Seth, K. Srinivasan, P. Levis, S. Katti, and P. Sinha, "Practical, real-time, full duplex wireless," in *Annual International Conference on Mobile Computing and Networking*, 2011, pp. 301–312.
- [57] L. Li, A. Song, L. J. Cimini, X. G. Xia, and C. C. Shen, "Interference cancellation in in-band full-duplex underwater acoustic systems," in *MTS/IEEE Oceans - Washington*, 2015, pp. 1–6.
- [58] N. Judell, "Cancellation systems, methods, apparatuses, and software for acoustic or electromagnetic measurement or communications," Jan 2020, US Patent 10,536,320.
- [59] S. Haykin, *Adaptive Filter Theory*. Prentice Hall, 2002.

- [60] G. Qiao, S. Gan, S. Liu, L. Ma, and Z. Sun, "Digital self-interference cancellation for asynchronous in-band full-duplex underwater acoustic communication," *Sensors*, vol. 18, no. 6, pp. 1700–1716, 2018.
- [61] M. Stojanovic and J. Preisig, "Underwater acoustic communication channels: Propagation models and statistical characterization," *IEEE communications magazine*, vol. 47, no. 1, pp. 84–89, 2009.
- [62] C. Healy, B. Jeburb, C. Tsimenidisa, J. Neashama, and J. Chambersc, "Full-duplex channel analysis for underwater acoustic communications," in *Underwater Acoustics Conference and Exhibition, Crete, Greece*, July 2019, pp. 251–258.
- [63] T. Yang, "Properties of underwater acoustic communication channels in shallow water," *The Journal of the Acoustical Society of America*, vol. 131, no. 1, pp. 129–145, 2012.
- [64] M. Towliat, Z. Guo, L. J. Cimini, X.-G. Xia, and A. Song, "Self-interference channel characterization in underwater acoustic in-band full-duplex communications using ofdm," *arXiv preprint arXiv:2005.10933*, 2020.
- [65] M. Johnson, L. Freitag, and M. Stojanovic, "Improved Doppler tracking and correction for underwater acoustic communications," in *1997 IEEE International Conference on Acoustics, Speech, and Signal Processing*, vol. 1. IEEE, 1997, pp. 575–578.
- [66] B. S. Sharif, J. Neasham, O. R. Hinton, and A. E. Adams, "A computationally efficient Doppler compensation system for underwater acoustic communications," *IEEE Journal of Oceanic Engineering*, vol. 25, no. 1, pp. 52–61, 2000.
- [67] J. Li, Y. V. Zakharov, and B. Henson, "Multibranch autocorrelation method for Doppler estimation in underwater acoustic channels," *IEEE Journal of oceanic engineering*, vol. 43, no. 4, pp. 1099–1113, 2017.
- [68] C. Liu, Y. V. Zakharov, and T. Chen, "Doubly selective underwater acoustic channel model for a moving transmitter/receiver," *IEEE Transactions on Vehicular Technology*, vol. 61, no. 3, pp. 938–950, 2012.
- [69] M. Siderius and M. B. Porter, "Modeling broadband ocean acoustic transmissions with time-varying sea surfaces," *The Journal of the Acoustical Society of America*, vol. 124, no. 1, pp. 137–150, 2008.
- [70] B. Henson, J. Li, Y. V. Zakharov, and C. Liu, "Waymark baseband underwater acoustic propagation model," in *IEEE Underwater Communications and Networking, Sestri Levante, Italy, September*, 2014, pp. 1–5.
- [71] L. Liao, B. Henson, and Y. Zakharov, "Grid waymark baseband underwater acoustic transmission model," in *Underwater Acoustics Conference and Exhibition*, 2017, pp. 343–350.

- [72] M. B. Porter, “The Bellhop manual and user’s guide: Preliminary draft,” *Heat, Light, and Sound Research, Inc., La Jolla, CA, USA, Tech. Rep*, 2011.
- [73] D. B. Percival, “Simulating gaussian random processes with specified spectra,” *Computing Science and Statistics*, pp. 534–534, 1993.
- [74] “Zoom F4 multitrack recorder,” <https://www.zoom-na.com/products/field-video-recording/field-recording/zoom-f4-multitrack-field-recorder>, [Accessed: 08- Oct- 2018].
- [75] “Pulse PLA series Power Amplifier,” <http://www.pulse-audio.co.uk/product/pla300/>, [Accessed: 17- Aug- 2020].
- [76] “Behringer A800 reference amplifier,” <https://www.behringer.com/product.html?modelCode=POCE8>, [Accessed: 17- Aug- 2020].
- [77] “ULTRA-DI DI100 Professional Battery/Phantom Powered DI-Box,” [https://static.bhphotovideo.com/lit\\_files/84886.pdf](https://static.bhphotovideo.com/lit_files/84886.pdf), [Accessed: 26- Nov- 2018].
- [78] “Low frequency underwater transducer,” <https://www.benthowave.com/products/BII-7530lowfrequencytransducer.html>, [Accessed: 08- Oct- 2018].
- [79] “Acoustic calibration service,” <http://www.neptune-sonar.co.uk/services/acoustic-calibration-service/>, [Accessed: 13- June- 2020].
- [80] “Low noise broadband hydrophone,” <https://www.benthowave.com/products/BII-7010Hydrophone.html>, [Accessed: 19- Nov- 2018].
- [81] “Neptune sonar - hydrophones with pre-amplifiers,” <http://www.neptune-sonar.co.uk/product-category/standard-transducer-products/hydrophones/hydrophone-with-pre-amplifier/>, [Accessed: 26- Feb- 2020].
- [82] F. H. Gregorio, G. J. González, J. Cousseau, T. Riihonen, and R. Wichman, “Distortion for power amplifier linearization in full-duplex transceivers without extra RF chain,” in *IEEE International Conference on Acoustics, Speech and Signal Processing*, 2017, pp. 6563–6567.
- [83] G. L. Stüber, *Principles of mobile communication*. Springer Science & Business Media, 2011.
- [84] J. Proakis and M. Salehi, *Digital Communications*, ser. McGraw-Hill International Edition. McGraw-Hill, 2008.
- [85] “ANALOG DEVICES Datasheet of the SHARC+ Dual-Core DSP with Arm Cortex-A5,” [https://www.analog.com/media/en/technical-documentation/data-sheets/ADSP-SC582\\_583\\_584\\_587\\_589\\_ADSP-21583\\_584\\_587.pdf](https://www.analog.com/media/en/technical-documentation/data-sheets/ADSP-SC582_583_584_587_589_ADSP-21583_584_587.pdf), [Accessed: 30- Jan- 2019].

- [86] Y. V. Zakharov, G. P. White, and J. Liu, "Low-complexity RLS algorithms using dichotomous coordinate descent iterations," *IEEE Transactions on Signal Processing*, vol. 56, no. 7, pp. 3150–3161, 2008.
- [87] J. Liu, Y. V. Zakharov, and B. Weaver, "Architecture and FPGA design of dichotomous coordinate descent algorithms," *IEEE Transactions on Circuits and Systems I: Regular Papers*, vol. 56, no. 11, pp. 2425–2438, 2009.
- [88] C. Rapp, "Effects of HPA-nonlinearity on a 4-DPSK/OFDM-signal for a digital sound broadcasting signal," in *European Conference on Satellite Communications*, 1991, pp. 179–184.
- [89] C. T. Tindle, G. B. Deane, and J. C. Preisig, "Reflection of underwater sound from surface waves," *The Journal of the Acoustical Society of America*, vol. 125, no. 1, pp. 66–72, 2009.
- [90] P. Diniz, *Adaptive Filtering: Algorithms and Practical Implementation*, ser. Kluwer international series in engineering and computer science. Springer US, 2008.
- [91] Y. V. Zakharov and J. Li, "Sliding-window homotopy adaptive filter for estimation of sparse UWA channels," in *IEEE Sensor Array and Multichannel Signal Processing Workshop*, 2016, pp. 1–4.
- [92] Y. V. Zakharov, T. C. Tozer, and J. F. Adlard, "Polynomial spline-approximation of Clarke's model," *IEEE Transactions on Signal Processing*, vol. 52, no. 5, pp. 1198–1208, 2004.
- [93] M. Niedzwiecki, "Functional series modeling approach to identification of nonstationary stochastic systems," *IEEE Transactions on Automatic Control*, vol. 33, no. 10, pp. 955–961, 1988.
- [94] G. W. Wornell, "A Karhunen-Loeve-like expansion for 1/f processes via wavelets," *IEEE Transactions on Information Theory*, vol. 36, no. 4, pp. 859–861, 1990.
- [95] M. K. Tsatsanis and G. B. Giannakis, "Time-varying system identification and model validation using wavelets," *IEEE Transactions on Signal Processing*, vol. 41, no. 12, pp. 3512–3523, 1993.
- [96] M. Visintin, "Karhunen-Loeve expansion of a fast Rayleigh fading process," *Electronics Letters*, vol. 32, no. 18, pp. 1712–1713, 1996.
- [97] M. K. Tsatsanis and G. B. Giannakis, "Modelling and equalization of rapidly fading channels," *Int. J. Adaptive Contr. Signal Processing*, vol. 10, no. 2-3, pp. 159–176, 1996.
- [98] Z. Tang and G. Leus, "Time-multiplexed training for time-selective channels," *IEEE Signal Processing Letters*, vol. 14, no. 9, pp. 585–588, 2007.

- [99] G. Leus, "On the estimation of rapidly time-varying channels," *Proc. EUSIPCO'04, Vienna, Austria*, pp. 2227–2230, Sep. 2004.
- [100] H. Mai, Y. V. Zakharov, and A. G. Burr, "Iterative channel estimation based on B-splines for fast flat fading channels," *IEEE Transactions on Wireless Communications*, vol. 6, no. 4, pp. 1224–1229, Apr. 2007.
- [101] T. Zemen and C. F. Mecklenbrauker, "Time-variant channel estimation using discrete prolate spheroidal sequences," *IEEE Transactions on Signal Processing*, vol. 53, no. 9, pp. 3597–3607, 2005.
- [102] D. Slepian, "Prolate spheroidal wave functions, Fourier analysis and uncertainty, V: The discrete case," *Bell System Technical Journal*, vol. 43, no. 6, pp. 3009–3058, 1964.
- [103] P. S. Rossi and R. R. Muller, "Slepian-based two-dimensional estimation of time-frequency variant MIMO-OFDM channels," *IEEE Signal Processing Letters*, vol. 15, pp. 21–24, 2008.
- [104] M. Niedźwiecki and M. Ciołek, "Generalized Savitzky–Golay filters for identification of nonstationary systems," *Automatica*, vol. 108, p. 108477, 2019.
- [105] M. J. Niedźwiecki, M. Ciołek, and A. Gańcza, "A new look at the statistical identification of nonstationary systems," *Automatica*, vol. 118, p. 109037, 2020.
- [106] Y. V. Zakharov and T. C. Tozer, "Local spline approximation of time-varying channel model," *Electronics Letters*, vol. 37, no. 23, pp. 1408–1409, 2001.
- [107] D. K. Borah and B. D. Hart, "Frequency-selective fading channel estimation with a polynomial time-varying channel model," *IEEE Transactions on Communications*, vol. 47, no. 6, pp. 862–873, 1999.
- [108] C. Shin, J. G. Andrews, and E. J. Powers, "An efficient design of doubly selective channel estimation for OFDM systems," *IEEE Transactions on Wireless Communications*, vol. 6, no. 10, pp. 3790–3802, 2007.
- [109] T. Hrycak, S. Das, and G. Matz, "Inverse methods for reconstruction of channel taps in OFDM systems," *IEEE Transactions on Signal Processing*, vol. 60, no. 5, pp. 2666–2671, 2012.
- [110] M. Niedzwiecki and T. Klaput, "Fast recursive basis function estimators for identification of time-varying processes," *IEEE Transactions on Signal Processing*, vol. 50, no. 8, pp. 1925–1934, 2002.
- [111] I. Gradshteyn and I. Ryzhik, *Table of Integrals, Series, and Products*. Elsevier Science, 2014.
- [112] S. Soliman and M. Srinath, *Continuous and Discrete Signals and Systems*. Prentice Hall, 1998.

- 
- [113] Y. V. Zakharov, V. H. Nascimento, R. C. De Lamare, and F. G. D. A. Neto, “Low-complexity DCD-based sparse recovery algorithms,” *IEEE Access*, vol. 5, pp. 12 737–12 750, 2017.
- [114] Y. Wang and W. Yin, “Sparse signal reconstruction via iterative support detection,” *SIAM Journal on Imaging Sciences*, vol. 3, no. 3, pp. 462–491, 2010.
- [115] Y. Zakharov and V. H. Nascimento, “Homotopy algorithm using dichotomous coordinate descent iterations for sparse recovery,” in *IEEE Asilomar Conference on Signals, Systems and Computers*, 2012, pp. 820–824.
- [116] Y. V. Zakharov and V. H. Nascimento, “Homotopy RLS-DCD adaptive filter,” in *International Symposium on Wireless Communication Systems*, 2013, pp. 1–5.
- [117] “Supplement: supplementary material (including MATLAB codes),” <https://eti.pg.edu.pl/katedra-systemow-automatyki/Automatica>, [Accessed: 2- Dec- 2020].
- [118] M. B. Elmashade and A. Aboshosha, “Active and passive self-interference cancellation techniques for full-duplex systems in the next generation (5G) of mobile communication networks,” *Advances in Networks*, vol. 5, no. 51, pp. 14–21, 2017.
- [119] E. Aryafar and M. A. Khojastepour, “MIDU: enabling MIMO full duplex,” in *International Conference on Mobile Computing Networking (MobiCom), Istanbul, Turkey, August*, 2012, pp. 257–268.
- [120] L. Bjørnø, *Applied Underwater Acoustics*. Elsevier Science, 2017.

